THE EFFECT OF STRUCTURAL LAYOUT ON THE SUPERSONIC FLUTTER CHARACTERISTICS OF A FIGHTER WING

A THESIS SUBMITTED TO
THE GRADUATE SCHOOL OF NATURAL AND APPLIED SCIENCES
OF
THE MIDDLE EAST TECHNICAL UNIVERSITY

BY

BAŞAK OKUMUŞ

IN PARTIAL FULFILLMENT OF THE REQUIREMENTS
FOR
THE DEGREE OF MASTER OF SCIENCE
IN
AEROSPACE ENGINEERING

AUGUST 2018

Approval of the thesis:

THE EFFECT OF STRUCTURAL LAYOUT ON THE SUPERSONIC FLUTTER CHARACTERISTICS OF A FIGHTER WING

submitted by **BAŞAK OKUMUŞ** in partial fulfillment of the requirements for the degree of **Master of Science in the Department of Aerospace Engineering, Middle East Technical University** by,

Prof. Dr. Halil Kalıpçılar
Dean, Graduate School of **Natural and Applied Sciences** _____

Prof. Dr. Ozan Tekinalp
Head of Department, **Aerospace Engineering** _____

Prof. Dr. Altan Kayran
Supervisor, **Aerospace Engineering Dept., METU** _____

Examining Committee Members:

Assoc. Prof. Dr. Demirkan Çöker
Aerospace Engineering Dept., METU _____

Prof. Dr. Altan Kayran
Aerospace Engineering Dept., METU _____

Prof. Dr. Dilek Funda Kurtuluş
Aerospace Engineering Dept., METU _____

Assoc. Prof. Dr. Ercan Gürses
Aerospace Engineering Dept., METU _____

Prof. Dr. Nafiz Alemdaroğlu
School of Civil Aviation, Atılım University _____

Date: _____

I hereby declare that all information in this document has been obtained and presented in accordance with academic rules and ethical conduct. I also declare that, as required by these rules and conduct, I have fully cited and referenced all material and results that are not original to this work.

Name, Last name : BAŞAK OKUMUŞ

Signature : _____

ABSTRACT

THE EFFECT OF STRUCTURAL LAYOUT ON THE SUPERSONIC FLUTTER CHARACTERISTICS OF A FIGHTER WING

Okumuş, Başak
M.S., Department of Aerospace Engineering
Supervisor: Prof. Dr. Altan Kayran

August 2018, 134 pages

The increase in flexibility of modern aircraft structures requires the aeroelastic effects be taken into consideration from the very beginning of the design phase in order to escape expensive iterations during the subsequent design phases and lower the required weight penalties resulting from compliance to certain aeroelastic requirements. Therefore, to be able to predict the supersonic flutter velocity is important in the preliminary design phase of fighter aircraft to increase design efficiency. In the first phase of the thesis study, the supersonic aerodynamics required for the flutter calculations are derived for a typical section wing section model using the application of Possio's theory proposed by Garrick and Rubinow and the supersonic Piston theory. A code is developed applying these theories and it is used to estimate the supersonic flutter speed of a finite plate wing model. In the second phase of the study, the commercial aeroelastic solver ZAERO is utilized to calculate the flutter speed of the weakened AGARD 445.6 Wing. Finally, a fighter wing model is created and its various layout options are analyzed in terms of their effect on supersonic flutter speed with ZAERO. The spar number and orientation, the skin ply orientation and the effect of an external mass is analyzed to observe their effects on the supersonic flutter speed.

Keywords: Typical Section Wing Model, Fighter Wings, Supersonic Aerodynamics, Wing Flutter, Aeroelasticity, Structural Layout

ÖZ

SAVAS UÇAGI İÇ YAPISINDAKİ ALTERNATİF TASARIM ÇÖZÜMLERİNİN SES ÜSTÜ HIZLARDAKİ ÇIRPINMA KARAKTERİSTİĞİNE ETKİSİ

Okumuş, Başak
Yüksek Lisans, Havacılık ve Uzay Mühendisliği Bölümü
Tez Yöneticisi: Prof. Dr. Altan Kayran

Ağustos 2018, 134 sayfa

Modern hava araçlarında esnekliğin artışıyla, aeroelastik etkilerin tasarım fazının en başından dikkate alınması önem kazanmıştır. Aeroelastik isterlere uygunluğun, tasarımın erken aşamalarında doğru olarak belirlenmesi, tasarımın ileriki seviyelerinde olası iterasyonları ve düzeltmeleri engelleyerek maliyet ve zaman açısından verimliliği arttıracaktır. Bu sebeplerden ötürü, konsept tasarım fazında ses üstü çırpınma hızının tespit edilebilmesi önem kazanmaktadır. Tez çalışmasının ilk aşamasında, çırpınma hesaplarında kullanılan ses üstü aerodinamiği, Garrick ve Rubinow'un öne sürdüğü Possio teorisi ve ses üstü Piston teorisi ile basit iki boyutlu kanat modeli için türetilmiştir. Bu teoriler temel alınarak üretilen kod, sonlu basit plaka kanat modelinin ses üstü çırpınma hızının tahmini için kullanılmıştır. Tez çalışmasının ikinci aşamasında, paket aeroelastik çözücü olan ZAERO kullanımıyla zayıflatılmış AGARD 445.6 kanadının ses üstü çırpınma hızı hesaplanmıştır. Çalışmanın sonunda, bir savaş uçağı kanat modeli oluşturulmuş ve çeşitli iç dizilimlerinin ses üstü çırpınma hızını etkisi araştırılmıştır. Spar sayısı ve oryantasyonu, kabuk tabaka oryantasyonu ve harici yük eklentisinin ses üstü çırpınma etkileri incelenmiştir.

Anahtar Sözcükler: Basit İki Boyutlu Kanat Modeli, Savaş Uçağı Kanatları, Ses üstü Aerodinamiği, Kanat Çırpınması, Kanat İç Dizilimi

To My Beloved Family,

ACKNOWLEDGMENTS

I would like to express my gratitude to my supervisor Prof. Dr. Altan Kayran, for giving me an opportunity to work with him, allowing me to benefit from his invaluable comments and experiences and his endless patience throughout my study.

I would like to thank my team at Turkish Aerospace for their encouragement, knowledge and empathy especially my chief Umut Susuz who introduced me to the field of aeroelasticity and my colleagues Evren Sakarya, Ezgi Üstün and Tuğçe Kiper Elibol. I would like thank the rest of my fellow colleagues at structural dynamics, load and weight team for their support throughout this study.

Special thanks to my close friends Dilan Özdil, Eren Kozan, Gülce Öztürk and Kevser Yüceer for the years that we spent together, for all the precious memories we created and for the support throughout this work.

I also would like to express my thanks to my oldest friends İrem Erkal, Elif Güler and Zeynep Artunç who kept me sane over the course of this work and for always being there for me with their continuous motivation.

Finally, my deepest appreciation goes to my family, my mother Sabriye Okumuş, my father Aydın Okumuş and my brother Kaan Okumuş. Without their encouragement, I would not have been able to finish this work.

TABLE OF CONTENTS

LIST OF TABLES

LIST OF FIGURES

LIST OF ABBREVIATIONS

DoF	Degree-of-freedom
FEM	Finite element model
CG	Center of gravity
EA	Elastic axis
NACA	National advisory committee for aeronautics
UAIC	Unified aerodynamic influence coefficient
IPS	Infinite plate spline
Im	Imaginary
Re	Real
FSI	Flutter speed index
QI	Quasi-isotropic
UD	Uni-directional
LE	Leading edge

LIST OF SYMBOLS

m	Mass of two-dimensional wing per unit distance perpendicular to the flow
I_a	Mass moment of inertia about axis of rotation per unit span
b	One-half chord
h	Bending displacement of axis of rotation
α	Torsional displacement of axis of rotation
x_α	Location of center of gravity measured from the elastic axis (non-dimensionalized with respect to chord length $(2b)$
x_0	Abscissa of axis of rotation of wing axis (elastic axis)
K_h	Bending stiffness of the wing
K_α	Torsion stiffness of the wing
L	Lift per unit span
M_α	Aerodynamic Moment per unit span
ω	Circular frequency of simple harmonic motion
c	Speed of sound
M	Mach number
ϕ	Disturbance velocity potential
t	Time at which disturbance is felt
T	Time at which disturbance is created
v	Velocity of main stream (supersonic)
$w(x,t)$	Vertical velocity at position x on chord and at time t
(x,y)	Coordinate measured in direction of main stream ordinate
(ξ,η)	Abscissa and ordinate of point of disturbance
k	Reduced frequency
p	Pressure
ρ	Free stream density
p'	Pressure difference
J_n	Bessel function of order n

$\bar{w}$	Frequency parameter
γ	Specific heat ratio of air
p_∞	Pressure of undisturbed stream
A_w	Cross-sectional area of the two-dimensional wing
M_w	Static moment of area of the two-dimensional wing about its leading edge
μ	Wing density parameter
r_a^2	Radius of gyration parameter
w_a	Pitching natural frequency
w_h	Plunging natural frequency
σ	Ratio of the wing bending frequency to the wing torsion frequency
U_F	Flutter speed
w_f	Flutter frequency

CHAPTER 1

INTRODUCTION

1.1 Motivation of the Thesis

Preliminary design is a good starting point for a more detailed analysis when designing an air vehicle. The structural layout is usually shaped during this phase of the aircraft design. Finding the appropriate structural layout and sizes early on in the design process will help avoid expensive redesign and corrections and increase design efficiency. Additionally, with the increase in flexibility of modern aircraft structures, aeroelastic effects must be taken into consideration from the beginning of a design phase in order to escape expensive iterations during the following phases and lower the needed weight penalties resulting from compliance to certain aeroelastic requirements. In the scope of aeroelastic requirements, an air vehicle being free from flutter in its operational region may be considered to be the most critical issue as this is the aeroelastic phenomena which can have the most dangerous consequences. Moreover, although for conventional aircraft the subsonic or near sonic speed ranges may be the main concern, for a high-speed combat aircraft, the problem of aeroelastic instabilities in the supersonic region can become the primary issue. Therefore, understanding the effect of wing structural layout on supersonic flutter as a guide for preliminary design is crucial in terms design efficiency.

1.2 Literature Survey

Aeroelasticity deals with the interactions between inertial, elastic and aerodynamic forces that act on a body exposed to a fluid flow [1]. The first systematic description of the aeroelasticity was given in 1946 by Collar, who defined a triangle of forces in which the inertial, elastic and aerodynamic forces each occupies a corner [2]. Each aeroelastic phenomenon can be located in the triangle according to the forces involved in its occurrence. The aeroelasticity triangle is illustrated in Figure 1.1.

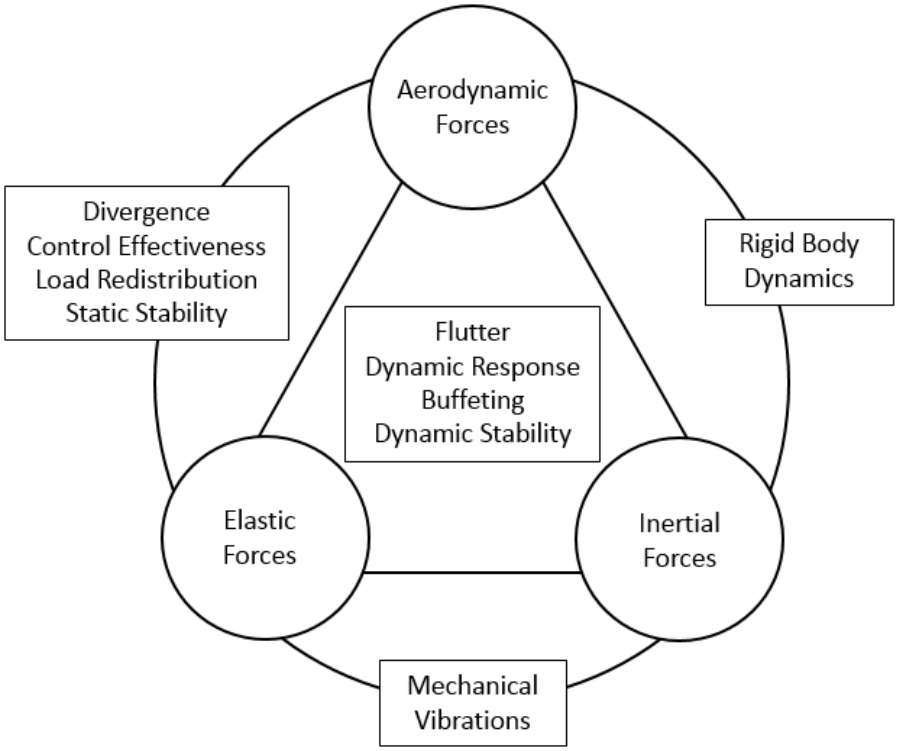

Figure 1.1 Collar's Triangle of Aeroelasticity

Flutter is a type of dynamic aeroelastic instability, which results from the interaction of the elastic, inertia and aerodynamic forces. It may be considered as the most dangerous problem of aeroelasticity since this phenomenon can have violent consequences. Flutter occurs when the structure extracts energy from the air stream and self-excited unstable oscillations start to grow in the structure. The amplitude of these oscillations increases violently in the current flight condition in a short amount of time and therefore an external excitation may not be applied to the system before catastrophic failure occurs. The classical type of flutter is associated with potential flow and usually involves coupling of two or more degrees-of-freedom. The non-

classical type of flutter is associated with separated flow, periodic breakaways, turbulence and stalling conditions [1].

The problem of supersonic flutter began to be studied more seriously when the aircraft started to be designed to fly at these flight conditions. In 1947 Charles Yeager became the first person to carry on a supersonic level flight with the X-l research airplane [3]. However the analytical flutter calculations had started to be considered a few years previous to that date. Von Borbely in 1942 [4], Temple and Jahn in 1945 [5] and Garrick and Rubinow [6] in 1946 expanding on Possio's work [7] in 1937 are the earliest contributors to the development of the analytical calculations of supersonic flutter problem. These theories were based on thin airfoil theory and linearization of the equation of motions. However, in 1953 Lighthill [8] showed that the nonlinear thickness effects are more dominant on the supersonic regions compared to the subsonic speeds with the simple piston theory. Furthermore, this approach was proved to be a less complicated one since the problem of determining the forces on an oscillatory airfoil is reduced to a one-dimensional flow problem of finding the pressure of a piston moving in a tube with this method.

The location of the aerodynamic center relative to the center of gravity is an important component of the aeroelastic instability. If the aerodynamic center is located behind the center of gravity, the aerodynamic forces and inertial forces will act in the same direction with respect to the shear center and therefore will oppose any deviation from equilibrium of the wing. However, if the aerodynamic center is located forward of the center of gravity, an opposite behavior will occur. The aerodynamic forces will reinforce an initial disturbance and will further remove the wing from equilibrium. The latter condition will result in a tendency towards instability compared to the former [9]. According to Raymer [10], for most airfoils, at subsonic speeds, the quarter-chord point is the aerodynamic center whereas at supersonic speeds, the aerodynamic center moves aft typically to about 45% of the mean aerodynamic chord. This shift of the aerodynamic center towards the rear may point to an unlikely occurrence of classical coupled flutter, however this is not the case as the effects of thickness, the changes in the flight altitudes and the different aircraft configurations that come to play due to the compliances in the supersonic regions, prevents flutter from being eliminated [3].

From the earliest contributions explained to the current timeline, the problem of supersonic flutter has been widely investigated in various areas. Sabri and Lakis [11] applied the supersonic piston theory aerodynamics to determine the flutter speed of a cylindrical shell. They compared the flutter results with and without the curvature effects and concluded that the correction term to account for shell curvature provides a better approximation for the pressure loading acting on a curved shell exposed to supersonic flow.

Niblett [12] examined the effects of engines mounted to the wing up to a Mach number of 2, on the flutter characteristics of the wing and the idea of engines acting as mass balancing components are investigated. He remarked that the torsional stiffness necessary to avoid flutter is greater than the bending stiffness stating that increasing the bending stiffness brings the natural frequencies closer together and increases the effect of any couplings that may occur. He concluded that the engines have a powerful mass balancing effect when placed at the forward locations of the wing. Furthermore, he stated that at supersonic speeds, the wing stiffness required to eliminate flutter shows a tendency to increase as the Mach number is reduced, highlighting the importance of the transonic region.

Zhang et al. [13] developed a local classical piston theory by separating the total loads induced by air into two parts which are the steady mean part caused by the mean location of the wing and the unsteady fluctuations resulting from the motion of the wing around its mean location. Then, this theory is compared with the unsteady Euler method to predict the flutter boundary of an airfoil with pitching and plunging degrees of freedom. They concluded that the local piston theory offers a better accuracy and wider applicability range compared to classical piston theory, with better cost and time efficiency compared to the Euler method.

Woolston and Huckel [14] presented the subsonic and supersonic flutter results for a wing having bending and torsional degrees-of-freedom as well as aileron rotation degree-of-freedom. They investigated the influence of the parameters that are the mass balance, control surface frequency relative to the wing frequency and the structural damping. In terms of mass balance, they concluded that the results indicate a reverse effect at the transonic speeds. In most of the calculations they conducted, at higher and

lower Mach numbers, overbalance aileron eliminates flutter however near a Mach number of 1, flutter occurs for an overbalanced aileron. With regard to the aileron frequency, a high value of the ratio of aileron frequency to wing bending or torsional frequency shows good results in eliminating wing-aileron flutter. Finally, they concluded that the influence of structural damping of the wing and aileron reduces the amount of mass balance or the value of the ratio of aileron frequency to the wing frequency required to avoid flutter.

Broadbent [15] presented the effect and importance of the rigid body modes involved in the supersonic flutter analysis of delta and swept wings. He remarks that for conventional wings flutter instability occurs due to the coupling of the bending and torsion modes leading to the importance of torsional stiffness in these types of systems. He further adds that with the implementation of swept back wings for high speed aircraft, flutter can arise due to the coupling of a single elastic mode and a rigid body mode. If the first elastic mode is the bending mode for these types of systems then the bending mode becomes primary importance. He concluded that the body freedoms have a higher impact on the supersonic flutter speeds for a swept-back wing rather than an unswept design. He stated that this results because of the greater bodily motion in the fundamental normal mode in addition to the higher contribution to the pitching inertia that result from the wings. Moreover, he found that for a fighter wing, the critical flutter frequency can be almost as half the frequency of the fundamental normal mode.

Mason [16] presented the theoretical and experimental results of a fighter wing concept adapted to increase the efficiency of supersonic maneuvering. He utilized the concept of Supercritic Conical Camber (SC^3) which is based on providing efficient attached flow high lift during supersonic speed. This is done by controlling the expansion and recompression of the crossflow, the lift on the upper surface is obtained without the use of adverse pressure gradient or crossflow shock wave sufficiently strong to separate the boundary layer. He shows with experiment results that by modifying the upper surface such that the supercritical crossflow can be controlled, associated drag due to lift can be reduced by about 20% for fighter-type wing planforms.

Sasher [17] listed the most important design constraints for a combat aircraft as the lift to drag ratio and specific fuel consumption. He remarked that the delta wing is a good solution for the transonic and supersonic speed requirements stating that at supersonic speed these type of wings induce low wave drag with the thin profiles leading to 30% improvement to existing aircraft. He further stated that other key concerns for a combat aircraft regarding the wing design are issues that arise from the high angle of attack which are the vortex flow control, post stall capability, high maneuverability and lateral and directional stability.

Striz and Venkayya [18] investigated the influence of structural complexity in the chordwise direction, in other words, the spar number variation of a fighter wing on its flutter characteristics. They analyzed a low aspect ratio wing with 5 and 10 spar configurations while keeping the total weight constant at a Mach number of 0.85. The model they analyzed had bending normal mode as well as coupled bending and torsion normal mode and in-plane bending mode. They showed that the natural frequencies as well as the flutter speed decreased when the spar number was increased. They concluded that while keeping the weight constant a coarser model in the chordwise direction is a non-conservative approach in terms of flutter constraints.

Liu, Wan and Yang [19] investigated the effects of the front and rear spar locations on the flutter speed for a large wing. They showed that as the front spar moves to the rear, the wing-box size, structural weight and stiffness decrease leading to an increase in the vertical displacements in the wingtip and a decrease in the flutter speed. Moreover, they showed that as the rear spar moves to the rear, the increase observed at the wing-box size, structural weight and stiffness are very little which results in the vertical displacements in the wingtip and a decrease in the flutter speed to be negligible. They concluded that the position of the leading edge spar had a far greater impact on the aeroelastic optimization process than the trailing edge spar.

Abdullah and Sulaeman [20] conducted the supersonic flutter analysis of a wing equipped with external missiles located at the inner two rib and at the wingtip. They located the flutter mode to be the bending of the tip of the wing, which points to the importance of the missile attached at this location in flutter analysis. They calculated the flutter speed for various altitudes at supersonic speeds and reached the conclusion

that at lower altitudes flutter speed becomes more critical while no significant variation is observed at the flutter frequency.

In terms of composite modelling of the wing structure, Turner and Grande [21] explored the effect of composite modelling on a wing with a cruise speed of Mach 2.7. A titanium wing configuration developed for a prior study was modified such that the upper and lower surface panels of the wing were given high strength graphite/polyimide sandwich panels, while the spar and ribs were kept as titanium. This resulted in a 17.8 % reduction in the weight compared to an all titanium wing. However, due to the large twist deflections at the tip region with this configuration, the flutter speed was quite low. The thickness of wing panel laminates was increased to improve the flutter speed and it was concluded that the final mass of the wing structure was significantly less than that of the titanium wing with an equal flutter speed.

Kennedy and Martins [22] evaluated the design of metallic and composite aircraft wings in terms of a trade-off between structural weight and drag. They showed that the composite wing designs are lighter between 34% and 40% than the equivalent metallic wings for the same lift to drag performance. Due to this large structural weight savings, the composite aircraft are able to achieve a fuel burn savings of between 5% and 8% and a take-off gross-weight savings of between 6% and 11%.

Ali and Hamed [23] analyzed the effect of the ply orientations on the flutter characteristics of a wing idealized as load carrying beam structure. They concluded that the bending and torsion are decoupled when the ply orientation is one of the four orientations of 0°,-45°,45°,90° for woven fiber and 0° or 90° for unidirectional fiber. Furthermore, they showed that maximum bending stiffness is achieved when the orientations are 0° or 90° and maximum torsional stiffness is achieved when the orientations are -45° or 45°. They showed that torsional rigidity has a more significant effect on the flutter speed.

Guo, Bannerjee and Cheung [24] carried on an analytical study on optimization of a laminated composite wing structure for achieving a maximum flutter speed and a minimum weight without strength penalty. They observed that the asymmetric layup

is more preferable in terms of aeroelastic effects due the contribution of the bending torsion coupling stiffness. They showed that torsional rigidity is more significant in reducing the flutter speed. Furthermore, they remarked that the front and the rear spar of the structure layups increased the wing stiffness however had little impact on the flutter speed.

In terms of the structural layout of combat wings, Sensmeier and Samareh [25] carried on an extensive study on post-WWII aircraft. They researched a total of sixty-five different combat jet aircraft for the study and observed that high maneuver loads acting on the combat aircraft resulted in designs which have at least three spars and up to ten or more spars. In addition, one main deriving points of the wing structure design is integration with the fuselage structure. In terms of rib and spar spacing, they were able to reduce these fighter wings into two categories, which are multi-spar and multi-rib. Figure 1.2 shows that multi-rib configurations are more often observed in Russian and old U.S. fighter aircraft whereas multi-spar configurations are more dominant in modern U.S. fighters.

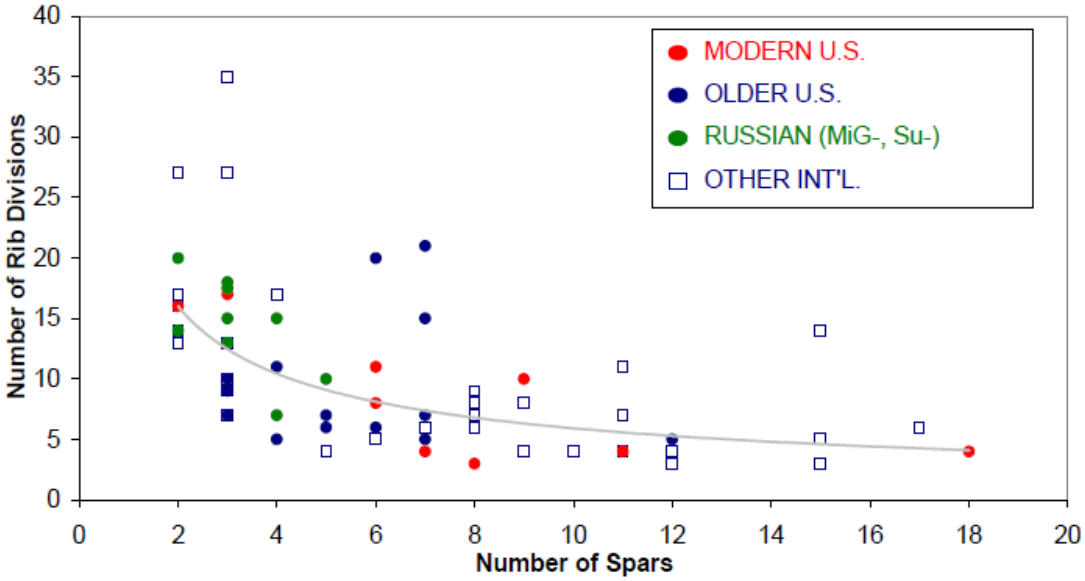

Figure 1.2 Number of Spar and Rib Variations for Various Combat Aircraft [25]

Figure 1.3 - Figure 1.7 give structural layouts of some of the popular fighter wings. The aircrafts F-16, F-35 JSF and Eurofighter Typhoon are examples of the multi-spar wing layout configuration whereas the MiG-31 and F-22A aircrafts are examples of the multi-rib wing layout configuration.

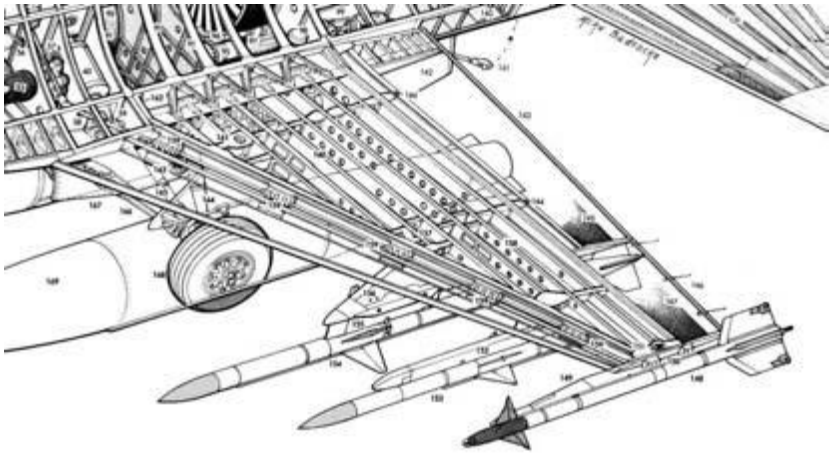

Figure 1.3 Lockheed Martin F-16 Wing Structural Layout [25]

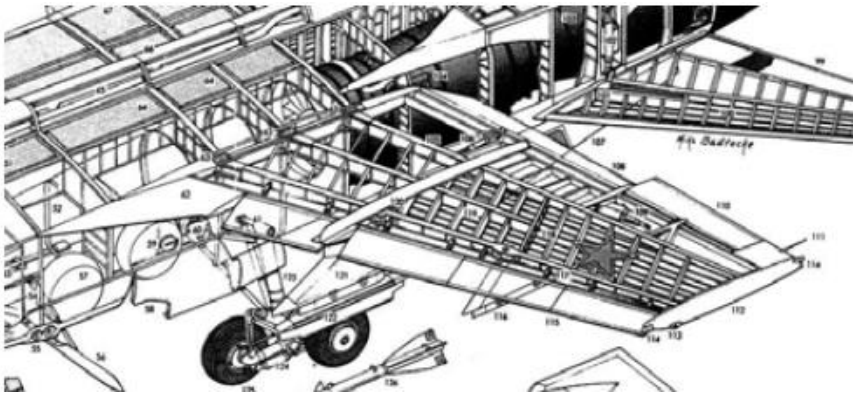

Figure 1.4 Mikoyan-Gurevich MiG-31 Foxhound Wing Structural Layout [25]

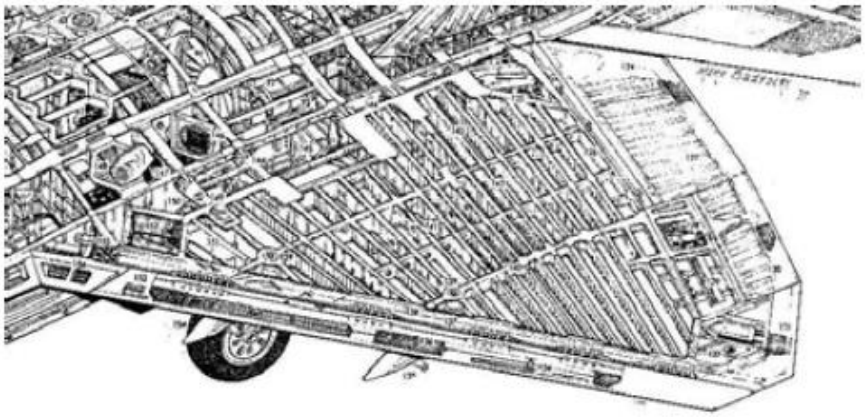

Figure 1.5 Lockheed Martin F-22A Raptor Wing Structural Layout [25]

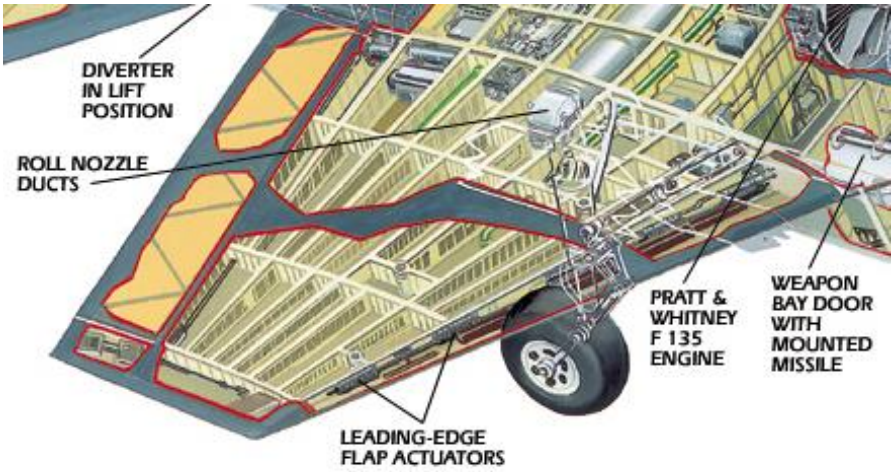

Figure 1.6 Lockheed Martin F 35 JSF Wing Structural Layout [25]

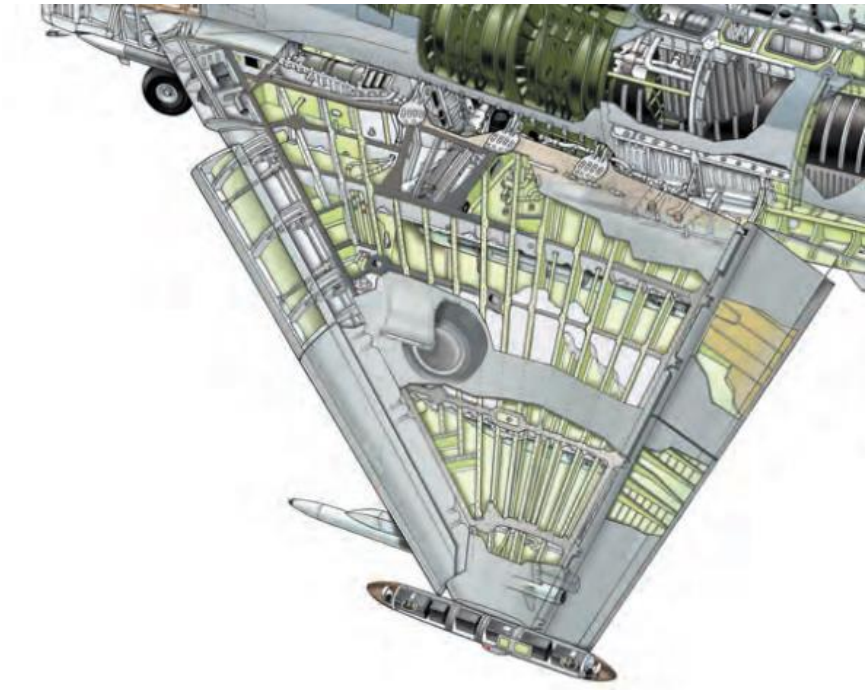

Figure 1.7 Eurofighter Typhoon Structural Layout [26]

It can be concluded that in modern combat aircraft, multi-spar layouts are more widespread. Furthermore, Weissberg, Green and Mey-Paz [27] have compared structural concepts for aircraft wings. They state that wing should be designed with respect to the constraints of aerodynamic forces acting on the wing and the torsional stiffness in order to avoid flutter. They further explain that the main limiting criterion for multi-spar and multi-rib configurations is the skin buckling. They show that in terms of skin buckling, reducing the distance between the spars have a larger impact

compared to the distance between the ribs. In the light of this information, for this study, the structural layout is varied such that the ribs are kept the same between the configurations and the effect of spar numbers and spar orientations on the supersonic aeroelastic instability speeds are investigated.

1.3 Scope of the Thesis

The research in the scope of the thesis can be divided into two main parts. The first part of the thesis is the theory of supersonic aerodynamics used for the flutter calculations. Two methods are investigated and applied for the calculations. These methods are derived for typical section wing models having bending and torsion degrees-of-freedom. The first method used is the application of Possio theory of non-stationary flow for small disturbances in a two-dimensional supersonic flow proposed by Garrick and Rubinow [6] and the second method is the supersonic Piston theory [28]. With the use of these theories, a code is written in MATLAB and validated with the results in literature [29]. Then; the estimation of the supersonic flutter speed of a finite wing using the typical section wing aerodynamics is investigated. For this, a simple plate model with stiffeners along the leading and the trailing edge is created and the effect of the variation of parameters such as the span, beam cross-section and the material on the flutter speed are observed. The second part of the thesis is the investigation of the supersonic flutter speed of a fighter wing. Initially, the commercial aeroelastic solver ZAERO is applied to solve the flutter speed of a Weakened AGARD 445.6 wing to validate its applicability with experimental results. Then, a fighter wing model is created to investigate the effect of structural layout on its supersonic flutter characteristics. The aspects of structural layout investigated are the spar number and orientation, the skin composite ply orientation and the effect of an external mass attached to the ribs of the wing. Various configurations are created to come to the conclusion of how the supersonic flutter speed is affected with the different configuration wings.

1.4 Content of the Thesis

- In Chapter 2, the typical section model is introduced as a simplification of a finite wing. This reduction is done by giving the geometric and inertial properties of an appropriate section of a finite wing to the two-dimensional typical section model. Then, the aerodynamic lift and moment equations for a typical section wing model are derived by two supersonic theories, the first one being Possio theory proposed by Garrick and Rubinow and the second one being the supersonic Piston theory. Then, with the construction of the flutter problem with these methods, two codes are developed in MATLAB that solve the supersonic flutter speed. Finally, the validation of the codes with literature is presented as well as their comparison to each other.

- In Chapter 3, the supersonic flutter speed of a finite wing is estimated with the two-dimensional supersonic Piston theory with thickness effects. A simple plate wing model is created with stiffeners on the leading and trailing edges. The variation of the span, beam cross-section and the material properties is analyzed and its effect on the supersonic flutter speed calculated by the typical section aerodynamics is observed to show that this simplification can provide the change of flutter speed in terms of certain parameters correctly. Finally, the code results are compared to results obtained from ZAERO.

- In Chapter 4, a general review of the commercial aeroelastic solver ZAERO is provided. The supersonic aerodynamics, the spline approach and the flutter calculation method implemented in ZAERO is summarized as basis information for the upcoming analysis. Then, ZAERO is utilized to solve the flutter problem of the Weakened AGARD 445.6 Wing and the results are compared with the experimental solutions to prove the applicability of the ZAERO commercial tool.

- In Chapter 5, a finite element model of a fighter wing is created. Mesh refinement analyses of the structural and aerodynamic models are presented and the reasoning behind the mesh sizes chosen are explained. Then the effect of the various aspects of the layout of a fighter wing on its supersonic flutter speed is analyzed. Initially, the spar number is varied to observe the effects. Then, different spar configurations

are implemented to investigate the effect on flutter speed. In addition, the skin material is varied from aluminum to carbon fiber reinforced plastic as well as various composite ply orientations and the supersonic flutter speed is calculated. And finally, an external mass representing a missile or a pod is attached to the various locations of the middle rib of the baseline configuration and its effect is investigated.

- In Chapter 6, the thesis is summarized and the results are discussed. In addition, the future work that can be carried on based on the work applied in this thesis is given.

CHAPTER 2

SUPERSONIC FLUTTER ANALYSIS OF A TYPICAL WING SECTION

2.1 Mathematical Modelling of a 2 DoF Typical Section

In literature, when the sophisticated analysis tools that are used today were not available, aeroelasticity analyses were carried out by using a typical section model. The typical section model is a simplified aeroelastic system, which consists of a rigid, elastically restrained airfoil in two-dimensional flow. Figure 2.1 shows the representation of this system. $Z = 0$ is the centerline where b is the half-chord length, a is the ratio of the distance between the centerline and the elastic axis to the half-chord length, b and x_a, which is the static unbalance, is the ratio of distance between the elastic axis and the center of gravity of the airfoil to the half-chord length, b. The airfoil is given plunging and pitching degrees of freedom represented by the linear springs located in the elastic axis whose restraining spring stiffness values are K_h and K_α, respectively. The airfoil deflection in the plunging direction is represented with h and the airfoil deflection angle in the pitching direction is represented with α. L is the aerodynamic lift force and M_y is the aerodynamic moment.

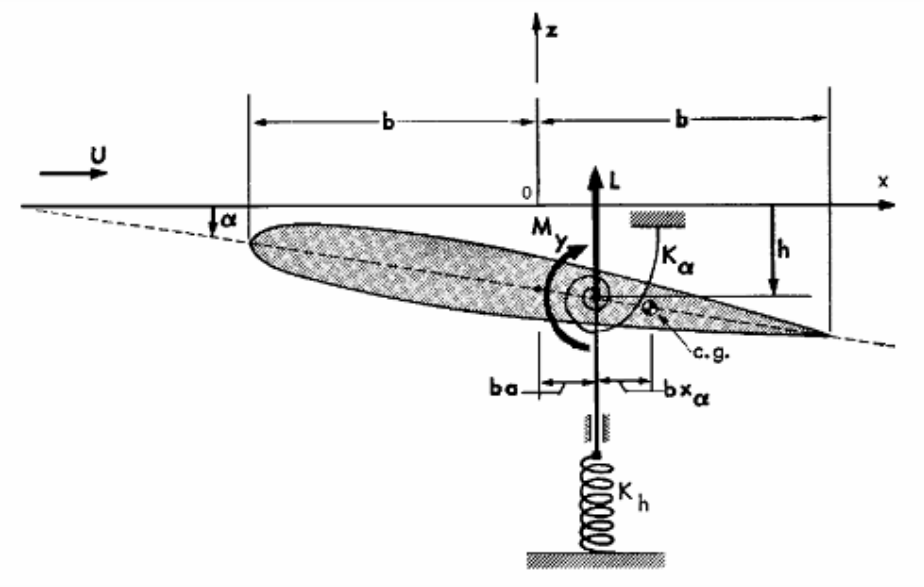

Figure 2.1 The 2 DoF Typical Section [1]

The equations of motions for the typical section are given as;

$$m\ddot{h} + mbx_\alpha\ddot{\alpha} + K_h h = L \tag{2.1}$$

$$I_\alpha\ddot{\alpha} + mbx_\alpha\ddot{h} + K_\alpha\alpha = M_\alpha \tag{2.2}$$

where m is the airfoil mass per unit span length and I_a is the airfoil mass moment of inertia per unit span length.

The motion is assumed to be simple harmonic and represented by;

$$h = \bar{h}e^{i\omega t} \tag{2.3}$$

$$\alpha = \bar{\alpha}e^{i\omega t} \tag{2.4}$$

Substituting the equations for simple harmonic motion gives a pair of algebraic equations for the amplitudes $\bar{h}$ and $\bar{\alpha}$ as;

$$-mw^2\bar{h}e^{i\omega t} - mbx_\alpha w^2\bar{\alpha}e^{i\omega t} + K_h\bar{h}e^{i\omega t} = L \tag{2.5}$$

$$-I_\alpha w^2\bar{\alpha}e^{i\omega t} - mbx_\alpha w^2\bar{h}e^{i\omega t} + K_\alpha\bar{\alpha}e^{i\omega t} = M_\alpha \tag{2.6}$$

In order for the Equations (2.5) and (2.6) to be solved, the lift and moment variables have to be defined. In the scope of this study, two different methods will be used to determine the supersonic aerodynamics which are the Possio's Theory in Section 2.2 and Piston's Theory in Section 2.3.

2.2. Solution of the 2 DoF Model Equations using the Supersonic Aerodynamics based on Possio's Theory

The supersonic characteristics of an oscillating airfoil with an infinite aspect ratio is studied by Possio [7]. The theory assumes the airfoil to be very thin, with small angle of attack with the non-stationary flow being nonviscous, unseparated and free of strong shocks. As a result, the theory of small perturbations on the flow is used with the linearization of the velocity potential equation.

Garrick and Rubinow [6] utilized the Possio theory of non-stationary flow for small disturbance in a two-dimensional supersonic flow to determine the aerodynamic forces acting on an airfoil. This chapter outlines the derivation of aerodynamic forces acting on the thin airfoil.

In reference [6], the wave equation is defined as the differential equation satisfied by the velocity potential in fixed coordinates for infinitesimal disturbances as given in Equation (2.7).

$$\frac{1}{c^2}\frac{\partial^2\phi}{\partial t^2} = \nabla\phi^2 \tag{2.7}$$

where c is the speed of sound.

The wave equation satisfied by the velocity potential in two-dimensional flow with the supersonic speed v in the negative x direction becomes;

$$\frac{1}{c^2}\frac{\partial^2\phi}{\partial t^2}+\frac{2v}{c}\frac{\partial^2\phi}{\partial x\partial t}+\left[\left(\frac{v}{c}\right)^2-1\right]\frac{\partial^2\phi}{\partial x^2}-\frac{\partial^2\phi}{\partial y^2}=0 \tag{2.8}$$

The source creates a disturbance of magnitude A originating at a point (ξ,η) at a time T which creates an effect at a point (x,y) at a later time t. As a result, the potential is a delayed potential and the elapsed time at (x,y) since the formation of the disturbance becomes $\tau=t-T$.

The source pulse in Equation (2.8) can be defined as;

$$\phi_0=\frac{A(\xi,\eta,T)}{\sqrt{c^2(t-T)^2-[x-\xi-v(t-T)]^2-(y-\eta)^2}} \tag{2.9}$$

In supersonic flow, the point influenced (x,y) is always behind the point of disturbance (ξ,η). The disturbance point, which moves forward with supersonic velocity, creates an angular region having half vertex angle of $\mu=\pm\sin^{-1}\frac{c}{v}=\pm\sin^{-1}M$ as shown in Figure 2.2. This creates the so-called Mach wedge, which simplifies the calculation of the fluid motion at any particular point due to an arbitrary supersonic wing since conditions at a certain point are influenced only by the portion of the plane restricted by the fore cone [1]. Upstream of the Mach wedge, the value of the source impulse becomes zero.

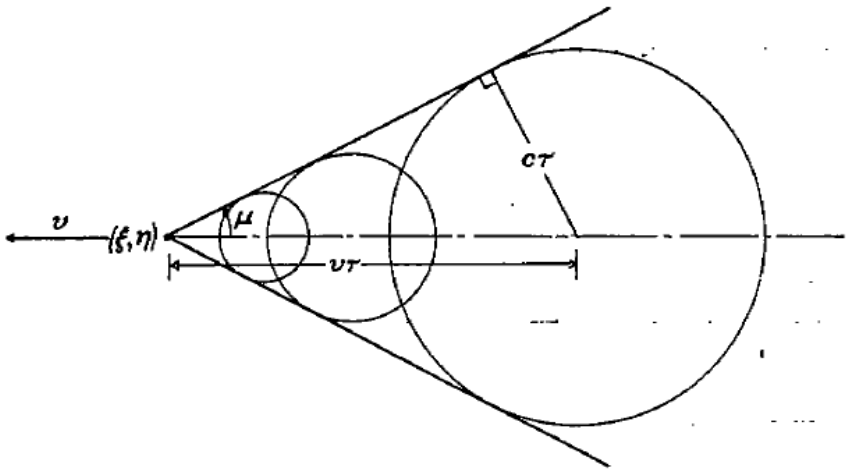

Figure 2.2 Mach Angle μ [6]

A disturbance at (ξ, η) created at a time T creates an influence at a point (x, y) after a certain time τ_1 has passed. The point moves at a speed greater than that of the wave which results in it entering the wave front of the disturbed region at a later time τ_2. Therefore, the duration of the disturbance becomes $\tau_2 - \tau_1$. The journey of a point travelling through a region of disturbance is described by the denominator of Equation (2.9) becoming zero. As a result, the values of τ_1 and τ_2 on the axis where $\eta = 0$ can be given as;

$$\tau_1 = \frac{M(x-\xi) - \sqrt{(x-\xi)^2 - y^2(M^2-1)}}{c(M^2-1)} \tag{2.10}$$

$$\tau_2 = \frac{M(x-\xi) + \sqrt{(x-\xi)^2 - y^2(M^2-1)}}{c(M^2-1)} \tag{2.11}$$

As previously stated, only the disturbances within the Mach wedge can create a disturbance. Figure 2.3 illustrates that a disturbance can affect (x, y) only forward of the Mach angle region.

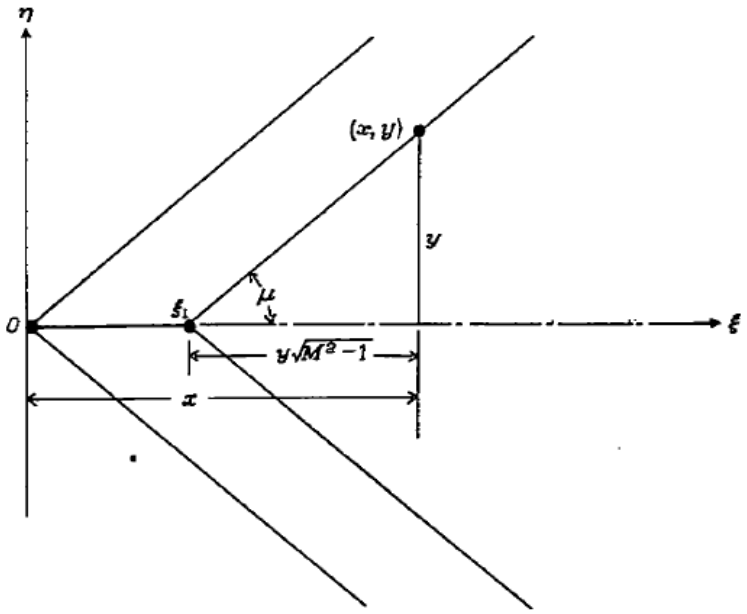

Figure 2.3 Disturbances Created with Vertex at ξ_1 [6]

Therefore, the total effect of the disturbances is obtained by the sum of any disturbance created in this region. From Figure 2.3, the following equation can be derived;

$$\frac{y}{x-\xi_1} = \tan\mu = \frac{1}{\sqrt{M^2-1}} \tag{2.12}$$

which leads to;

$$\xi_1 = x - y\sqrt{M^2-1} \tag{2.13}$$

The total potential at (x, y) at any time t can be expressed as;

$$\phi(x,y,t) = \int_0^{\xi_1} \int_{\tau_1}^{\tau_2} \frac{A(\xi,0,t-\tau)}{\sqrt{c^2\tau^2 - [x-\xi-v\tau]^2 - (y)^2}} d\tau\, d\xi \tag{2.14}$$

Rearranging the denominator of Equation (2.14) gives;

$$\phi(x,y,t) = \frac{1}{\sqrt{v^2 - c^2}} \int_0^{\xi_1} \int_{\tau_1}^{\tau_2} \frac{A(\xi, 0, t-\tau)}{\sqrt{(\tau - \tau_1)(\tau_2 - \tau)}} d\tau \, d\xi \tag{2.15}$$

If a tangential flow along the boundary of the airfoil is to be formed, then a vertical velocity of $w(x,t)$ has to be induced by the source. Accordingly, magnitude of the source, $A(\xi, 0, t-\tau)$ can be obtained by the boundary condition of this tangential flow on the airfoil given in Equation (2.16).

$$\left(\frac{\partial \phi}{\partial y}\right)_{y=0} = w(x,t) = \frac{\partial y(x,t)}{\partial t} + v\frac{\partial y(x,t)}{\partial x} \tag{2.16}$$

A new parameter θ is introduced in place of τ where;

$$2\tau = (\tau_2 - \tau_1)\cos\theta + \tau_2 + \tau_1 \tag{2.17}$$

Substituting Equation (2.17) into Equation (2.15) gives;

$$\phi(x,y,t) = \frac{1}{\sqrt{v^2 - c^2}} \int_0^{\xi_1} \int_0^{\pi} A\left(\xi, 0, t - \frac{\tau_2 + \tau_1}{2} - \frac{\tau_2 - \tau_1}{2}\cos\theta\right) d\theta \, d\xi \tag{2.18}$$

Differentiation of the disturbance velocity potential with respect to y gives [6];

$$\begin{aligned} \frac{\partial \phi}{\partial y} &= \frac{1}{\sqrt{v^2 - c^2}} \frac{\partial \xi_1}{\partial y} \pi A\left(\xi_1, 0, t - \frac{My}{c\sqrt{M^2 - 1}}\right) \\ &+ \frac{1}{\sqrt{v^2 - c^2}} \int_0^{\xi_1} \int_0^{\pi} \frac{\partial^2 A}{\partial t^2} \sin^2\theta \; d\theta \, d\xi \end{aligned} \tag{2.19}$$

In order to obtain the term ${}^{\partial \xi_1}/_{\partial y}$, Equation (2.13) is differentiated with respect to y;

$${}^{\partial \xi_1}/_{\partial y} = -\sqrt{M^2 - 1} \tag{2.20}$$

Substituting Equation (2.20) into Equation (2.19) and taking the limit as y approaches zero on the positive side gives,

$$\left(\frac{\partial \phi}{\partial y}\right)_{y=+0} = -\frac{\pi}{c} A(x, 0, t) \tag{2.21}$$

When y approaches zero from the negative side, the equal but opposite sign result is obtained. The magnitude of the source can be obtained by rearranging Equation (2.21) and inserting Equation (2.16).

$$A(x, t) = -\frac{c}{\pi} w(x, t) \tag{2.22}$$

The total potential equation can then be expressed as follows:

$$\phi(x, t) = -\frac{1}{\pi} \frac{1}{\sqrt{M^2 - 1}} \int_0^x \int_{\tau_1}^{\tau_2} \frac{w(\xi, t - \tau)}{\sqrt{(\tau - \tau_1)(\tau_2 - \tau)}} d\tau \, d\xi \tag{2.23}$$

where from Equations (2.10) and (2.11);

$$\tau_1 = \frac{x - \xi}{c(M + 1)} \tag{2.24}$$

$$\tau_2 = \frac{x - \xi}{c(M - 1)} \tag{2.25}$$

The total potential equation can be applied to an airfoil with leading edge at $x = 0$ and chord of $2b$, moving in small oscillations. If the wing has a degree of freedom in the displacement h and twist in α about its elastic axis, the vertical velocity of any point on the airfoil can be expressed as;

$$w(x, t) = -\left[\dot{h} + v\alpha + (x - x_0)\dot{\alpha}\right] \tag{2.26}$$

where x_0 is the position of the elastic axis measured from the leading edge.

As previously stated, simple harmonic motion is assumed. Therefore, the velocity function can be expressed as follows for convenience;

$$w(\xi, t-\tau) = w(\xi, t)e^{-i\omega\tau} \tag{2.27}$$

Substituting Equation (2.27) into Equation (2.23) gives;

$$\phi(x,t) = -\frac{1}{\sqrt{M^2-1}}\int_0^x w(\xi,t)\, I(\xi,x)\, d\xi \tag{2.28}$$

where

$$I(\xi,x) = \frac{1}{\pi}\int_{\tau_1}^{\tau_2} \frac{e^{-i\omega\tau}}{\sqrt{(\tau-\tau_1)(\tau_2-\tau)}}\, d\tau \tag{2.29}$$

Reintroducing the parameter θ as in Equation (2.17), using the values of τ_1 and τ_2 from Equations (2.24) and (2.25) and the related Bessel function gives;

$$I(\xi,x) = e^{-i\omega\frac{x-\xi}{c}\frac{M}{M^2-1}} J_0\left(\frac{x-\xi}{c}\frac{w}{M^2-1}\right) \tag{2.30}$$

In the following sections, the variables x and ξ are used as non-dimensional quantities by dividing the original values by the chord $2b$.

Introducing the frequency parameters as follows;

$$k = \frac{\omega b}{v} \tag{2.31}$$

$$\overline{w} = \frac{2kM^2}{M^2-1} \tag{2.32}$$

Then, Equation (2.28) becomes;

$$\phi(x,t) = \frac{2b}{\sqrt{M^2-1}} \int_0^x \left[\dot{h} + v\alpha + 2b(\xi - x_0)\dot{\alpha}\right] I(\xi, x)\, d\xi \tag{2.33}$$

where the function $I(\xi, x)$ is;

$$I(\xi, x) = e^{-i\omega(x-\xi)} J_0\left(\frac{\overline{w}}{M}(x-\xi)\right) \tag{2.34}$$

In order to form the aerodynamic lift force and moment, the theory of small disturbances is utilized to obtain the basic pressure formula for p as follows [6];

$$p = -\rho \frac{d\phi}{dt} = -\rho\left(\frac{\partial \phi}{\partial t} + v\frac{\partial \phi}{\partial x}\right) \tag{2.35}$$

where ρ is the density of the atmosphere.

The local pressure difference between the upper and lower surfaces of the airfoil at any non-dimensional point x can be expressed as;

$$p' = -2\rho\left(\frac{\partial \phi}{\partial t} + \frac{v}{2b}\frac{\partial \phi}{\partial x}\right) \tag{2.36}$$

The total force, in other words lift acting on the airfoil can be expressed as;

$$L = 2b\int_0^1 p' dx = -2\rho v \int_0^1 \frac{\partial \phi}{\partial x}\, dx - 4\rho b \int_0^1 \phi\, dx \tag{2.37}$$

The moment acting on the airfoil about the elastic axis can be expressed as;

$$M_\alpha = 4b^2 \int_0^1 (x - x_0) p' dx$$
$$= -2\rho v \int_0^1 \frac{\partial \phi}{\partial x} (x - x_0) dx - 8\rho b^2 \int_0^1 \phi\, (x - x_0) dx \tag{2.38}$$

The sign convention of the lift and moment equations can be seen in Figure 2.1. In Reference [6] further reductions are carried out and the final aerodynamic expressions are obtained as follows;

$$L = -4\rho b v^2 k^2 e^{i\omega t} \left[\left(\frac{\overline{h}}{b} \right) (L_1 + iL_2) + \bar{a}(L_3 + iL_4) \right] \tag{2.39}$$

$$M_\alpha = -4\rho b^2 v^2 k^2 e^{i\omega t} \left[\left(\frac{\overline{h}}{b} \right) (M_1 + iM_2) + \bar{a}(M_3 + iM_4) \right] \tag{2.40}$$

where explicit expressions in the lift (L) and the pitching moment (M) expressions are given by Garrick and Rubinow [6] as follows:

$$L_1 = \frac{1}{\sqrt{M^2 - 1}} \left\{ -2(f_0)_R + \frac{1}{k} \left[J_0 \left(\frac{\overline{w}}{M} \right) \sin \overline{w} - \frac{1}{M} J_1 \left(\frac{\overline{w}}{M} \right) \cos \overline{w} \right] \right\} \tag{2.41}$$

$$L_2 = \frac{1}{\sqrt{M^2 - 1}} \left\{ -2(f_0)_I + \frac{1}{k} \left[J_0 \left(\frac{\overline{w}}{M} \right) \cos \overline{w} + \frac{1}{M} J_1 \left(\frac{\overline{w}}{M} \right) \sin \overline{w} \right] \right\} \tag{2.42}$$

$$L_3 = L_3' - 2x_0 L_1 \tag{2.43}$$

$$L_4 = L_4' - 2x_0 L_2 \tag{2.44}$$

$$L_3' = L_1 + \frac{1}{k} L_2 + A_1 \tag{2.45}$$

$$L_4' = L_2 - \frac{1}{k}L_1 + A_2 \tag{2.46}$$

$$M_1 = M_1' - 2x_0L_1 \tag{2.47}$$

$$M_2 = M_2' - 2x_0L_2 \tag{2.48}$$

$$M_3 = M_3' - 2x_0[(M_1' + L_3') - 2x_0L_1] \tag{2.49}$$

$$M_4 = M_4' - 2x_0[(M_2' + L_4') - 2x_0L_2] \tag{2.50}$$

$$M_1' = L_1 - A_1 \tag{2.51}$$

$$M_2' = L_2 - A_2 \tag{2.52}$$

$$M_3' = \frac{4}{3}(L_1 - B_1) + \frac{1}{k}(L_2 + A_2) \tag{2.53}$$

$$M_4' = \frac{4}{3}(L_2 - B_2) - \frac{1}{k}(L_1 + A_1) \tag{2.54}$$

The terms in the equations are given as follows [6];

$$A_1 = \frac{1}{\sqrt{M^2 - 1}}\frac{1}{M}\frac{1}{2k^2}\left[\frac{1}{M}(f_0)_R - \frac{1}{M}J_0\left(\frac{\overline{w}}{M}\right)\cos\overline{w} - J_1\left(\frac{\overline{w}}{M}\right)\sin\overline{w}\right] \tag{2.55}$$

$$A_2 = \frac{1}{\sqrt{M^2 - 1}}\frac{1}{M}\frac{1}{2k^2}\left[\frac{1}{M}(f_0)_I - \frac{1}{M}J_0\left(\frac{\overline{w}}{M}\right)\sin\overline{w} - J_1\left(\frac{\overline{w}}{M}\right)\cos\overline{w}\right] \tag{2.56}$$

$$B_1 = \frac{1}{\sqrt{M^2 - 1}}\frac{1}{M}\frac{1}{2k^2}\left[-\frac{2}{\overline{w}}J_1\left(\frac{\overline{w}}{M}\right)\cos\overline{w} + \frac{1}{M}J_0\left(\frac{\overline{w}}{M}\right)\cos\overline{w} + J_1\left(\frac{\overline{w}}{M}\right)\sin\overline{w}\right] \tag{2.57}$$

$$B_2 = \frac{1}{\sqrt{M^2-1}}\frac{1}{M}\frac{1}{2k^2}\left[\frac{2}{\bar{w}}J_1\left(\frac{\bar{w}}{M}\right)\sin\bar{w} - \frac{1}{M}J_0\left(\frac{\bar{w}}{M}\right)\sin\bar{w} + J_1\left(\frac{\bar{w}}{M}\right)\cos\bar{w}\right] \quad (2.58)$$

where the values of $f_0(M,\bar{w}) = (f_0)_R + i(f_0)_I$ are defines as;

$$(f_0)_R = \frac{1}{\bar{w}}\int_0^{\bar{w}} J_0\left(\frac{u}{M}\right)\cos u\, du \quad (2.59)$$

$$(f_0)_I = -\frac{1}{\bar{w}}\int_0^{\bar{w}} J_0\left(\frac{u}{M}\right)\sin u\, du \quad (2.60)$$

2.3. Solution of the 2 DoF Model Equations using Supersonic Aerodynamics based on Piston's Theory

Piston theory calculates the aerodynamic force and moments on an aircraft by relating the body's motion and the local normal component of fluid velocity to each other. Piston theory has been extensively studied in literature and the basis relies on the quasi-steady point-function relationship with the surface downwash and aerodynamic pressure point on an airfoil [28]. In this theory, an airfoil moving in a stream can be reduced to a piston moving in a one-dimensional channel with the reference frame (x,y) given in Figure 2.4.

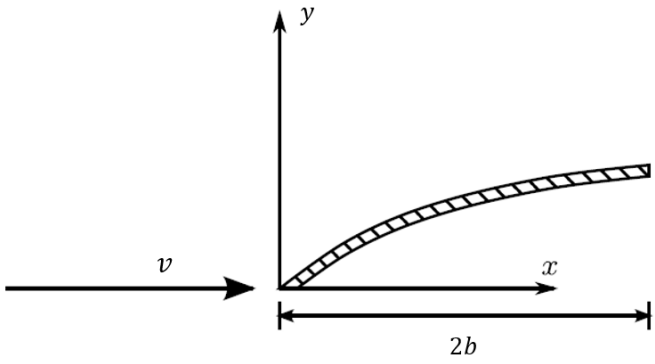

Figure 2.4 Piston Theory Reference Frame [28]

An airfoil moving with a velocity v in a channel containing a gas with a density of ρ and undisturbed pressure of p_∞ will generate a pressure on the upper and lower surfaces of the lifting surface as follows [28].

$$p(x,t) = p_\infty \left[1 + \frac{(\gamma - 1)}{2}\frac{w}{c}\right]^{\frac{2\gamma}{\gamma - 1}} \tag{2.61}$$

where the term γ is the specific heat ratio of gas which can be taken as 1.4 for air and the vertical velocity that is generated is;

$$w(x,t) = -\left(\frac{\partial y}{\partial t} + v\frac{\partial y}{\partial x}\right) = -\left[\dot{h} + v\alpha + (x - x_0)\dot{\alpha}\right] \tag{2.62}$$

which shows consistency to the equations in Possio's Theory explained in Section 2.2.

Furthermore, expanding Equation (2.61), the following third order equation holds true,

$$\frac{p}{p_\infty} = 1 + \gamma\left(\frac{w}{c}\lambda\right) + \frac{\gamma(\gamma+1)}{4}\left(\frac{w}{c}\lambda\right)^2 + \frac{\gamma(\gamma+1)}{12}\left(\frac{w}{c}\lambda\right)^3 \tag{2.63}$$

where the aerodynamic correction factor is defined as;

$$\lambda = \frac{M}{\sqrt{M^2 - 1}} \tag{2.64}$$

The local pressure difference between the upper and lower surfaces of the airfoil can be expressed as [30]:

$$p' = \frac{4q}{M}\lambda\left[\left(\frac{\partial w}{\partial t}\frac{1}{v} + \frac{\partial w}{\partial x}\right) + \frac{1+\gamma}{12}\lambda^2 M^2\left(\frac{\partial w}{\partial t}\frac{1}{v} + \frac{\partial w}{\partial x}\right)^3\right] \tag{2.65}$$

where $q = \frac{1}{2}\rho v^2$ is the dynamic pressure.

Ashley [29] remark that the third order terms have been discovered to have negligible effects, therefore these terms are not included in the scope of this study.

The lift and moment equations are obtained as in Possio Theory from Equations (2.37) and (2.38). And the final lift and moment equations [29] are as follows:

$$L = -4\rho b v^2 k^2 e^{i\omega t}\left[\left(\frac{\bar{h}}{b}\right)(L_1 + iL_2) + \bar{a}(L_3 + iL_4)\right] \tag{2.66}$$

$$M_\alpha = -4\rho b^2 v^2 k^2 e^{i\omega t}\left[\left(\frac{\bar{h}}{b}\right)(M_1 + iM_2) + \bar{a}(M_3 + iM_4)\right] \tag{2.67}$$

where explicit expressions in the lift (L) and the pitching moment (M) expressions are given as follow [29];

$$L_1 = 0 \tag{2.68}$$

$$L_2 = 1/kM \tag{2.69}$$

$$L_3 = L_3' - 2x_0 L_1 \tag{2.70}$$

$$L_4 = L_4' - 2x_0 L_2 \tag{2.71}$$

$$L_3' = 1/k^2 M \tag{2.72}$$

$$L_4' = (1/kM) - [(\gamma + 1)/k](A_w/8b^2) \tag{2.73}$$

$$M_1 = M_1' - 2x_0 L_1 \tag{2.74}$$

$$M_2 = M_2' - 2x_0 L_2 \tag{2.75}$$

$$M_3 = M_3' - 2x_0[(M_1' + L_3') - 2x_0 L_1] \tag{2.76}$$

$$M_4 = M_4' - 2x_0[(M_2' + L_4') - 2x_0 L_2] \tag{2.77}$$

$$M_1' = 0 \tag{2.78}$$

$$M_2' = (1/kM) - [(\gamma + 1)/k](A_w/8b^2) \tag{2.79}$$

$$M_3' = (1/k^2 M) - [(\gamma + 1)/k^2](A_w/8b^2) \tag{2.80}$$

$$M_4' = (4/3kM) - [(\gamma + 1)/k](M_w/4b^3) \tag{2.81}$$

where A_w is the cross sectional area of the airfoil and M_w is the static moment of inertia of the airfoil about its' leading edge. It is important to note that these terms vanish for the Zero Thickness Piston Theory.

2.4. Solution of the Flutter Determinant using the Classical Flutter Method

Sections 2.2 and 2.3 explain the supersonic aerodynamics of both theories and give the aerodynamic lift force and moment equations. The final forms of these expressions are the same however; the explicit equations of the lift (*P*) and the pitching moment (*M*) differ between the theories. These terms will be specified in the following sections.

The flutter solution is carried on by finalizing the equation of motions. Merging Equations (2.5), (2.6) and (2.39), (2.40) gives;

$$-\frac{m}{4\rho b^2}\left(\frac{\bar{h}}{b}\right) + \frac{m}{4\rho b^2} x_\alpha \bar{\alpha} + \frac{m}{4\rho b^2}\left(\frac{w_h}{w}\right)^2 \left(\frac{\bar{h}}{b}\right) = -\left[\left(\frac{\bar{h}}{b}\right)(L_1 + iL_2) + \bar{\alpha}(L_3 + iL_4)\right] \tag{2.82}$$

$$-\frac{m}{4\rho b^2}\frac{I_a}{mb^2}\bar{\alpha}-\frac{m}{4\rho b^2}x_\alpha\left(\frac{\bar{h}}{b}\right)+\frac{I_a}{mb^2}\frac{m}{4\rho b^2}\left(\frac{w_a}{w}\right)^2\bar{\alpha}$$
$$=-\left[\left(\frac{\bar{h}}{b}\right)(M_1+iM_2)+\bar{a}(M_3+iM_4)\right] \tag{2.83}$$

Equations (2.82) and (2.83) are applicable for both methods however the terms L_1, L_2, L_3, L_4 and M_1, M_2, M_3, M_4 differ accordingly.

In order to simplify the coefficients, the following dimensionless parameters are introduced.

$$\mu=\frac{m}{4\rho b^2} \quad \text{(wing density parameter)}$$

$$r_a^2=\frac{I_a}{mb^2} \quad \text{(radius of gyration parameter)} \tag{2.84}$$

$$w_a=\sqrt{\frac{K_\alpha}{I_a}} \quad \text{(pitching natural frequency)}$$

$$w_h=\sqrt{\frac{K_h}{m}} \quad \text{(plunging natural frequency)}$$

With the use of these parameters, Equations (2.82) and (2.83) become as follows;

$$-\mu\left(\frac{\bar{h}}{b}\right)+\mu x_\alpha\bar{\alpha}+\mu\left(\frac{w_h}{w}\right)^2\left(\frac{\bar{h}}{b}\right)=-\left[\left(\frac{\bar{h}}{b}\right)(L_1+iL_2)+\bar{a}(L_3+iL_4)\right] \tag{2.85}$$

$$-\mu r_a^2\bar{\alpha}-\mu x_\alpha\left(\frac{\bar{h}}{b}\right)+r_a^2\mu\left(\frac{w_a}{w}\right)^2\bar{\alpha}=-\left[\left(\frac{\bar{h}}{b}\right)(M_1+iM_2)+\bar{a}(M_3+iM_4)\right] \tag{2.86}$$

For the flutter analysis, these algebraic equations are solved for the related flight conditions. Because the equations are linear and homogenous for $(\bar{h}/b)$ and $\bar{\alpha}$, it is

necessary for Equations (2.85) and (2.86) to have a nontrivial solution. Therefore, Equation (2.87) must be satisfied.

$$\begin{vmatrix} \mu\left(\frac{w_h}{w}\right)^2 - \mu + L_1 + iL_2 & -\mu x_a + L_3 + iL_4 \\ -\mu x_a + M_1 + iM_2 & \mu r_a^2\left(\frac{w_a}{w}\right)^2 - \mu r_a^2 + M_3 + iM_4 \end{vmatrix} = 0 \qquad (2.87)$$

The determinant given by Equation (2.87) is called the flutter determinant. A new parameter can be defined as $\sigma = (w_h/w_a)$. So a common term explicitly available shows up which is w_a/w. Therefore, the expansion of the determinant will give a quadratic polynomial in the unknown $(w_a/w)^2$.

$$\begin{vmatrix} \mu\sigma^2\left(\frac{w_a}{w}\right)^2 - \mu + L_1 + iL_2 & -\mu x_a + L_3 + iL_4 \\ -\mu x_a + M_1 + iM_2 & \mu r_a^2\left(\frac{w_a}{w}\right)^2 - \mu r_a^2 + M_3 + iM_4 \end{vmatrix} = 0 \qquad (2.88)$$

To summarize and compare the dimensionless coefficients defining the lift and moment on the oscillating airfoil for the Piston and Possio theory, Table 2.1 is given.

Table 2.1 Comparison for the Dimensionless Aerodynamic Coefficients

Parameter	Possio Theory	Piston Theory
L_1	$\frac{1}{\sqrt{M^2-1}}\left\{-2(f_0)_R + \frac{1}{k}\left[J_0\left(\frac{\overline{w}}{M}\right)\sin\overline{w} - \frac{1}{M}J_1\left(\frac{\overline{w}}{M}\right)\cos\overline{w}\right]\right\}$	0

L_2	$\frac{1}{\sqrt{M^2-1}}\left\{-2(f_0)_I + \frac{1}{k}\left[J_0\left(\frac{\overline{w}}{M}\right)\cos\overline{w} + \frac{1}{M}J_1\left(\frac{\overline{w}}{M}\right)\sin\overline{w}\right]\right\}$	$1/kM$
L_3	$L_3' - 2x_0L_1$	$L_3' - 2x_0L_1$
L_4	$L_4' - 2x_0L_2$	$L_4' - 2x_0L_2$
L_3'	$L_1 + \frac{1}{k}L_2 + A_1$	$1/k^2M$
L_4'	$L_4' = L_2 - \frac{1}{k}L_1 + A_2$	$(1/kM) - [(\gamma + 1)/k](A_w/8b^2)$
M_1	$M_1' - 2x_0L_1$	$M_1' - 2x_0L_1$
M_2	$M_2' - 2x_0L_2$	$M_2' - 2x_0L_2$
M_3	$M_3' - 2x_0[(M_1' + L_3') - 2x_0L_1]$	$M_3' - 2x_0[(M_1' + L_3') - 2x_0L_1]$
M_4	$M_4' - 2x_0[(M_2' + L_4') - 2x_0L_2]$	$M_4' - 2x_0[(M_2' + L_4') - 2x_0L_2]$
M_1'	$L_1 - A_1$	0
M_2'	$L_2 - A_2$	$(1/kM) - [(\gamma + 1)/k](A_w/8b^2)$

M_3'	$\frac{4}{3}(L_1 - B_1) + \frac{1}{k}(L_2 + A_2)$	$(1/k^2M) - [(\gamma + 1)/k^2](A_w/8b^2)$
M_4'	$\frac{4}{3}(L_2 - B_2) - \frac{1}{k}(L_1 + A_1)$	$(4/3kM) - [(\gamma + 1)/k](M_w/4b^3)$

In the flutter determinant the unknowns regarding the motion and flight conditions, there are four unknowns; μ, w_a/w, M and k. In order for these values to be found, the second-degree polynomial equation from the determinant is solved. However, the complex quantities in the aerodynamic coefficients result in the complex equation representing two real equations, where both the real and imaginary parts have to be zero in order for the equations to be solved. In other words, since there are two equations to be solved, two of the four unknowns have to be defined. A procedure that can be used to solve the flutter problem is the Classical Flutter Method. The following steps outline this method:

1. Specify the parameter μ which represents the altitude.
2. Specify the Mach number, M.
3. Specify a set of trial values for the reduced frequency, k.
4. Calculate the aerodynamic functions L_1, L_2, L_3, L_4 and M_1, M_2, M_3, M_4 for each value of k and construct the flutter determinant.
5. Solve the flutter determinant for the corresponding values of $(w_a/w)^2$ for each values of k. Since this is a quadratic equation with complex coefficients, the roots will have a real and imaginary part. The real part of the root is an estimation of $(w_a/w)^2$ and the imaginary part is related to the damping of the mode.

6. Iterate until the k at which imaginary part of one of the roots zero is detected. This can be done by interpolating between the reduced frequency values where the imaginary part crosses the zero axis.

7. With the reduced frequency, k obtained by interpolation, repeat steps 4 and 5 until a reduced frequency value is found that gives an imaginary part closest to zero with a prescribed tolerance. This k value is then used to find the corresponding real value of $(w_a/w)^2$ from which the value of w can be obtained.

8. Determine the flutter speed using the values of w and k as follows;

$$U_F = {}^{bw}/_{k} \;\&\; M_F = U_F/c \tag{2.89}$$

9. Repeat steps from 3 to 7 until the output M obtained in step 8 converges to the initial M value given in step 2.

10. In order to sweep the whole flutter boundary in terms of altitude, repeat the process for different values of μ.

Figure 2.5 explains the classical flutter method in terms of a flowchart.

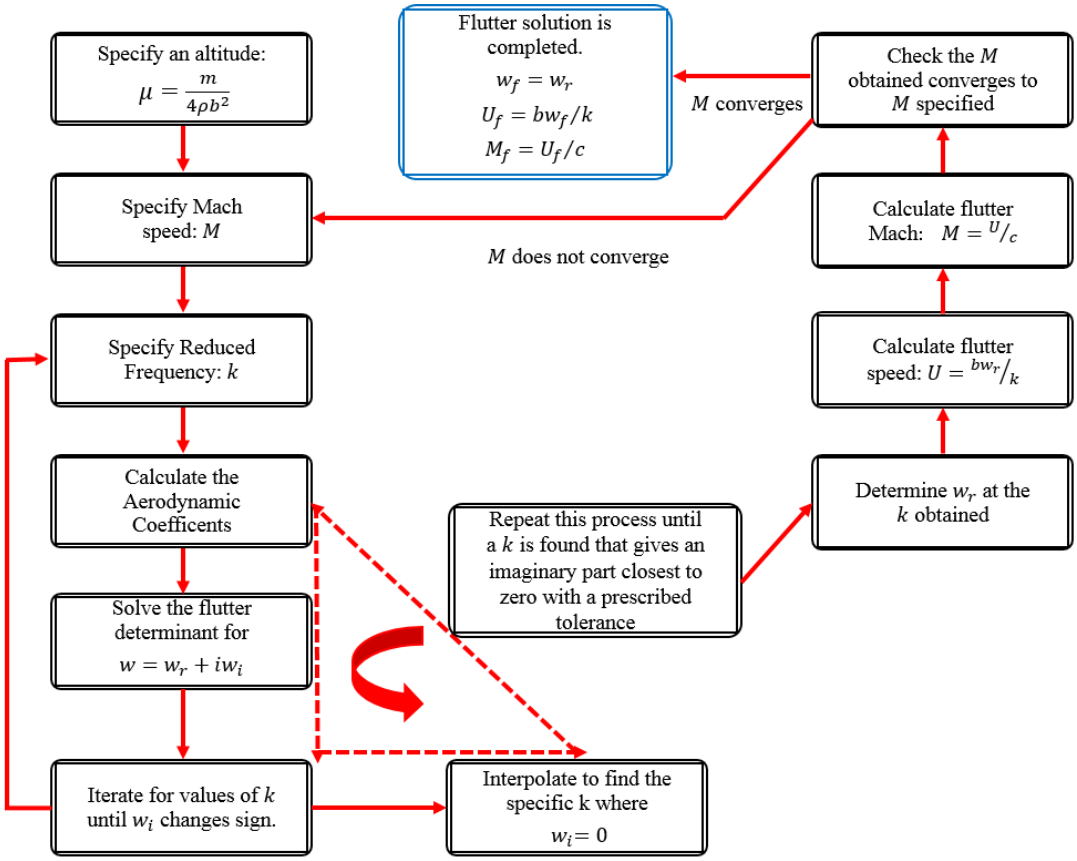

Figure 2.5 Flowchart for Classical Flutter Method Solution

2.5. Setting up a Solver to Estimate the Flutter Speed of a Typical Wing Model

The classical flutter method is an iterative process. Therefore, MATLAB [31] is utilized to significantly reduce the computation time. The eigenvalues of the flutter determinant are solved with the implementation of the "*eig*" command in MATLAB. In order for this command to be used, Equation (2.88) is rearranged in the form of $[X] - \lambda\,[Y] = 0$ as,

$$\begin{bmatrix} \mu - (L_1 + iL_2) & \mu x_a - (L_3 + iL_4) \\ \mu x_a - (M_1 + iM_2) & \mu r_a^2 - (M_3 + iM_4) \end{bmatrix} - \lambda \begin{bmatrix} \mu\sigma^2 & 0 \\ 0 & \mu r_a^2 \end{bmatrix} = 0 \qquad (2.90)$$

where $\lambda = (w_a/w)^2$.

Hence, the flutter frequency and speed are determined from;

$$Re(\lambda) = \left(\frac{w_a}{w_r}\right)^2 \rightarrow w_f = w_r = \frac{w_a}{\sqrt{Re(\lambda)}} \tag{2.91}$$

$$U_f = \frac{w_f b}{k} = \frac{w_a}{\sqrt{Re(\lambda)}}\frac{b}{k} \rightarrow \frac{U_f}{b w_a} = \frac{1}{k\sqrt{Re(\lambda)}} \tag{2.92}$$

Two separate codes for Possio and Zero Thickness Piston Theory are generated using the supersonic aerodynamics described previously. The flutter speed and frequency are obtained with the iteration process explained in Figure 2.5.

The inputs for the codes are given in Table 2.2.

Table 2.2 Input Parameters of the Typical Section Flutter Analysis Codes

Parameter	**Definition**
b	Half-chord
x_0	Distance of elastic axis from the leading edge (non-dimensionalized with respect to $2b$ chord length)
x_a	Distance of the center of gravity from the elastic axis (non-dimensionalized with respect to $2b$ chord length)
μ	Wing density parameter
M	Mach number
r_a^2	Radius of gyration parameter of the wing
σ	Ratio of the wing bending frequency to the wing torsion frequency

The codes written for Possio and Zero Thickness Piston Thery are validated with the results given in Reference [29]. Figure 2.6 and Figure 2.7 show the dimensionless flutter velocity U_f/bw_a vs. M of a typical section wing at three different altitudes. The wing analyzed has a low frequency ratio of $\sigma \approx 0$ and a radius of gyration of $r_a^2 = 0.25$ with elastic axis at its' midchord and center of gravity at its 60 per cent chord. The results show that, even though at higher altitudes the code results begin to differ ever so slightly from literature, in general, the code results can accurately determine the flutter speed of a typical wing section for both theories.

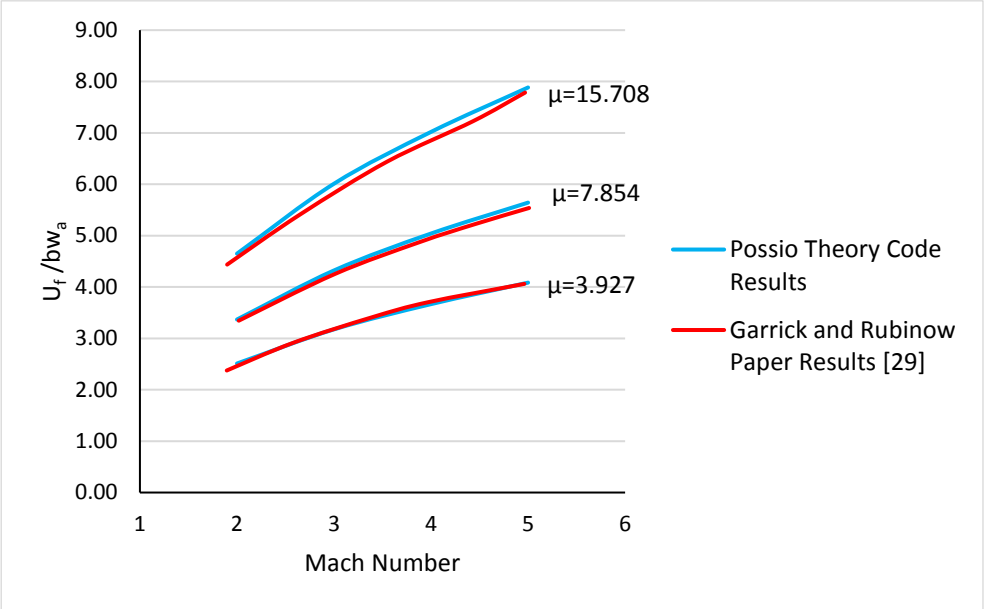

Figure 2.6 Comparison of the Code and Paper Results for the Possio Theory for $\sigma \approx 0$, $r_a^2 = 0.25$, $x_0 = 0.5$, $x_a = 0.2$

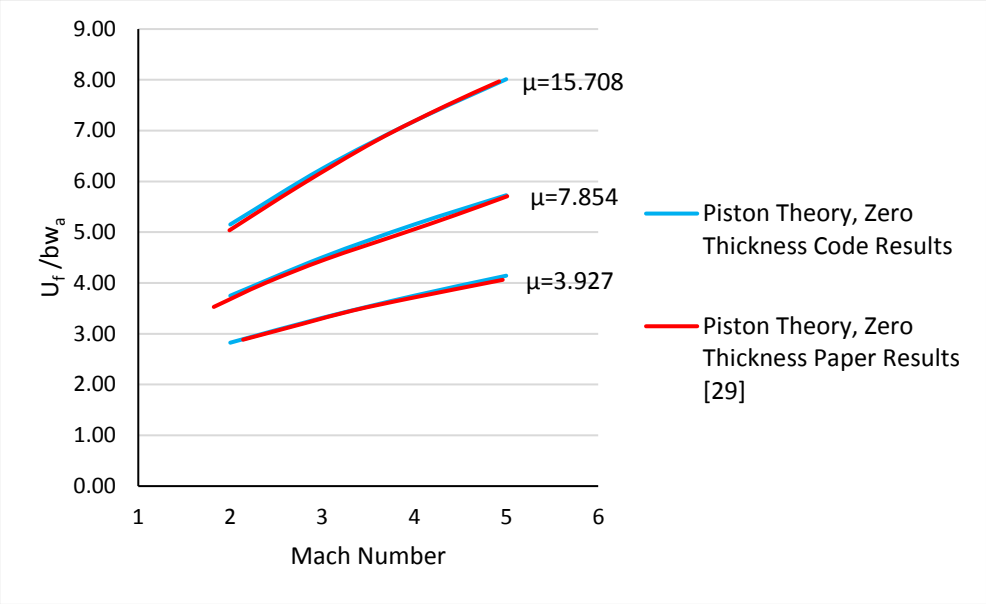

Figure 2.7 Comparison of the Code and Paper Results for the Piston Theory, Zero Thickness for $\sigma \approx 0$, $r_a^2 = 0.25$, $x_0 = 0.5$, $x_a = 0.2$

Numerical comparison of the theories is given in Table 2.3. It can be observed that there is a good correlation between the two theories especially at the higher Mach numbers for all altitudes. In deciding on which theory to continue with in the subsequent chapters, literature is taken as reference. Ashley [29] has reached the conclusion that for values of $M \geq 2.5$, the piston theory approach yields flutter speed values of 10% to their exact counterparts for a two-dimensional bending-torsion flutter. Moreover, Ashley [29] have calculated the flutter speed of a two-dimensional bending-torsion flutter with a zero thickness 20 per cent chord flap with the use of Piston theory at a Mach number of 2, and come to the conclusion that the piston theory results are consistent when compared to the exact flutter speed. In the light of these results, the theory for the flutter estimations given in Chapter 3 are performed with the use of the Piston Theory.

Table 2.3 Comparison of the Possio and the Zero Thickness Piston Theories

M	**Wing Density** μ	**Possio Theory Flutter Speed** U_f/bw_a	**Piston (0t) Theory Flutter Speed** U_f/bw_a	**Difference %**
2	3.927	2.51	2.82	11.1
3		3.18	3.31	4.2
4		3.67	3.75	2.2
5		4.09	4.14	1.4
2	7.854	3.37	3.75	10.2
3		4.32	4.50	4.0
4		5.04	5.15	2.2
5		5.64	5.73	1.5
2	15.708	4.65	5.15	9.8
3		6.01	6.25	3.8
4		7.02	7.19	2.3
5		7.88	8.01	1.6

CHAPTER 3

ESTIMATING THE SUPERSONIC FLUTTER SPEED OF A FINITE WING WITH THE TYPICAL WING MODEL AERODYNAMICS

The analysis of a multi degree-of-freedom system can be reduced to a simple two-dimensional typical section model for purposes of flutter prediction as demonstrated in Figure 3.1. This simplification can be done by giving the geometric and inertial properties of an appropriate section of a finite wing to the two-dimensional typical section model. For typical wing flutter, the modes involved are bending and torsion, therefore giving the airfoil the pitching and plunging degrees-of-freedom can be sufficient to simulate the motion of the oscillating wing.

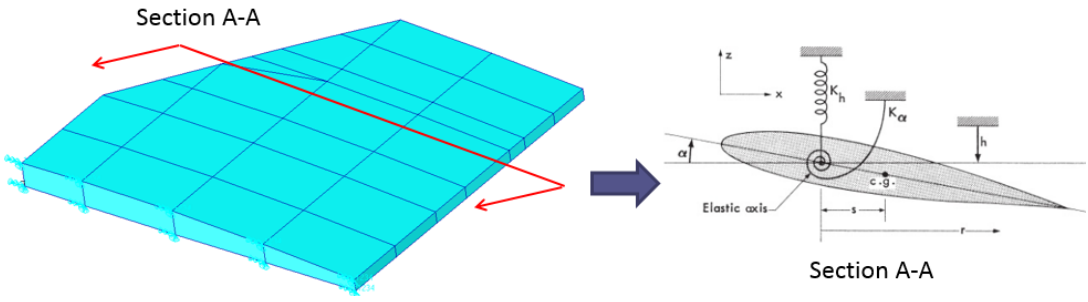

Figure 3.1 Simplification of a Wing to a Typical Section Model

In this section of the study, the aim is to estimate the supersonic flutter characteristics of a finite wing applying the typical section supersonic aerodynamics of the Piston Theory outlined in Section 2.3. For this purpose, a parametric study is carried out changing various wing parameters and observing their effect on the supersonic flutter speed. The code generated in Section 2.5 is used to calculate the flutter speed with a slight addition. In Section 2.5, zero thickness piston theory was utilized in terms of

comparison with the Possio Theory however; for this part, the thickness effects are also included to the theory.

3.1 Description of the Finite Element Model for the Supersonic Flutter Speed Estimation

The finite wing is a plate model which is stiffened with two rectangular stiffeners at its' leading and trailing edges as shown in Figure 3.2. The attachment of the wing-fuselage is simulated by fixing the related grids in all degrees-of-freedom.

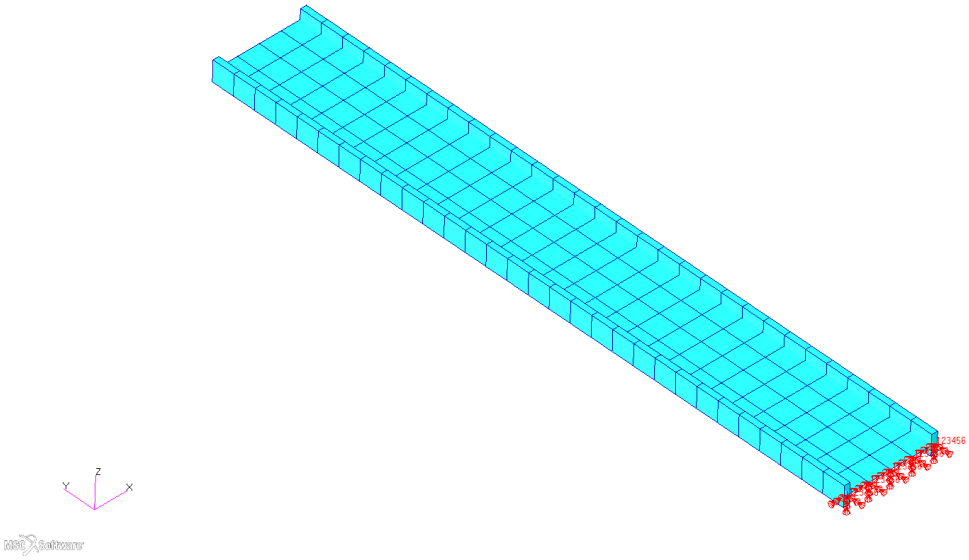

Figure 3.2 Finite Element Model of the Wing Structure

The cross-section of the finite element model is given in Figure 3.3. The flutter equations require the input of mass and moment of inertia per unit span, therefore, the wing is chosen with a constant cross-section to simplify the process of determining these parameters. Moreover, the symmetric nature of the model lets the center of gravity (CG) and the elastic axis (EA) to be located on the same plane which is the midchord.

The wing has a chord length of $c = 2b$ and a half-span of L with a plate thickness of t_s and a beam area of $t_a * t_b$. The material of both the stiffener and plate is kept the same and density of the wing is defined with the symbol ρ.

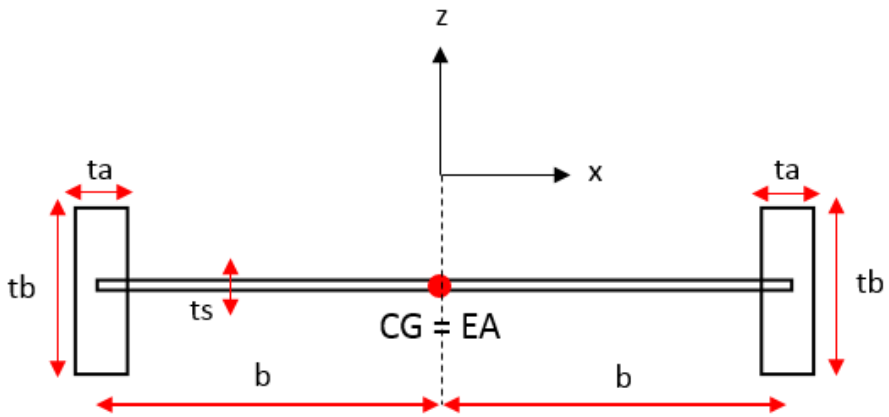

Figure 3.3 Cross-Section of the Wing Model given in Figure 3.2

The mass per unit length of the wing cross-section can be found as;

$$m'_{plate} = \frac{m_{plate}}{L} = \frac{2\rho(t_s b L)}{L} \tag{3.1}$$

$$m'_{stiffener} = \frac{m_{stiffener}}{L} = \frac{2\rho(t_a t_b L)}{L} \tag{3.2}$$

$$m'_{total} = m'_{plate} + m'_{stiffener} \tag{3.3}$$

The mass moment of inertia per unit length of the wing cross-section can be found from the following equations:

$$I'_a = I'_{plate} + I'_{stiffener} = \int r^2 dm' \tag{3.4}$$

$$I'_{plate} = 2\int_0^b r^2 \frac{m'_{plate}}{2b} dr \tag{3.5}$$

$$I'_{stiffener} = m'_{stiffener} * b^2 \tag{3.6}$$

The effect of the wing thickness is included with the terms A_w and M_w which are the airfoil cross-sectional area and the airfoil static moment of inertia about its leading edge. These terms can be found as;

$$A_W = A_{plate} + A_{stiffener} = t_s(2b) + 2(t_a t_b) \tag{3.7}$$

$$M_W = M_{plate} + M_{stiffener} = t_s(2b)\left(b + \frac{t_a}{2}\right) + (t_a t_b)\left(2b + \frac{t_a}{2}\right) + (t_a t_b)\left(\frac{t_a}{2}\right) \tag{3.8}$$

The baseline wing model has the parameters given in Table 3.1.

Table 3.1 Baseline Wing Parameters

Parameter	**Definition**	**Value**	**Unit**
L	Half-span	1.125	[m]
b	Half-chord	0.075	[m]
$t_a * t_b$	Stiffener Geometry	$0.01 * 0.035$	[m^2]
t_S	Plate Thickness	0.005	[m]
ρ	Wing Density	2700	[kg/m^3]
E	Modulus of Elasticity	70 000	[Pa]

3.2 Parametric Study

The purpose of this section is to show that the results obtained with the typical section code gives applicable results for a finite wing as well. The following sections present how the supersonic flutter characteristics of the finite wing calculated using the Piston theory typical section aerodynamics is affected by the change of the half-span, beam area and modulus of elasticity of the wing material.

One of the inputs of the code is the ratio of wing bending frequency to wing torsion frequency. Therefore, a modal analysis is conducted to determine the mode shapes of each configuration. The finite wing model with all the variations considered have first natural frequency as the first bending mode followed by the first torsion mode as the second natural frequency. As explained previously, the modes included for flutter prediction purposes are these two modes. Figure 3.4 shows the mode shapes for the baseline model calculated by MSC. Nastran [32].

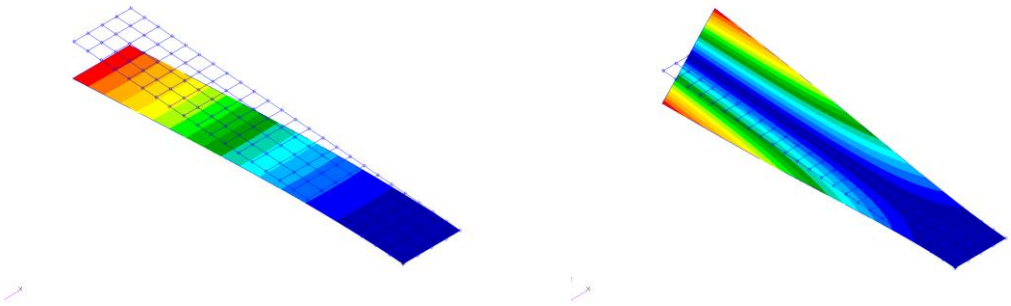

Mode 1 (1st Bending) Mode 2 (1st Torsion)

Figure 3.4 Mode shapes of the Finite Wing

After obtaining the natural frequencies from the normal modes analysis from MSC. Nastran, the code generated using supersonic Piston theory is utilized to obtain the flutter speeds. The flutter determinant in Equation (2.88)(2.81) is solved using the explicit lift and moment equations given in Equations (2.68) - (2.81).

3.2.1 Effect of the Span of the Wing on the Supersonic Flutter Speed

The first parameter, whose effect studied, is the span of the wing structure. If the wing is structurally reduced to a cantilever beam/bar fixed at one end and free at the other, the bending and torsional natural frequency is related to the length as follows [33];

$$w_{bending} \sim \sqrt{\frac{EI}{\rho A L^4}} \tag{3.9}$$

$$w_{torsion} \sim \sqrt{\frac{GJ}{\rho k_\theta L^2}} \tag{3.10}$$

where k_θ is the torsional stiffness coefficient for the cross-section an A is the cross-sectional area.

As explained in Section 3.2, the initial step to conducting the supersonic flutter speed of a finite wing using the typical section code is obtaining its modal frequencies. MSC Nastran is utilized to obtain the corresponding bending and torsion frequency for each span length configuration analyzed. Table 3.2 shows how the natural frequencies vary with the changing span lengths. Both the torsional and bending frequencies decrease with increasing span consistent with the simplified assumptions stated above. Moreover, the relations show that the bending frequency is more strongly affected by the length compared to the torsion frequency, which is also reflected in the results.

Table 3.2 Comparison of Modal Frequencies w.r.t. Half-Span

Half-Span [m]	**1st Bending [Hz]**	**1st Torsion [Hz]**
0.900	24.9	75.1
0.975	21.2	68.2
1.050	18.3	62.4
1.125	15.9	57.5

The supersonic aerodynamic force and moments, which are based on a two-dimensional theory, are the same for all the span lengths considered since all the terms which appear are per unit span length. Therefore, the effect will be included with the stiffness terms when solving the flutter determinant. It was observed in Table 3.2 that increasing span leads to decreasing natural frequencies, which means decreasing bending and torsional stiffness. Figure 3.5 reflects this remark, showing that the code was successful in predicting the decrease in the flutter speed as the span increases. It should be noted that, this rate of decrease should be less for a rigid wing as the modes will not be as affected with the changing span as it does for a flexible lifting surface.

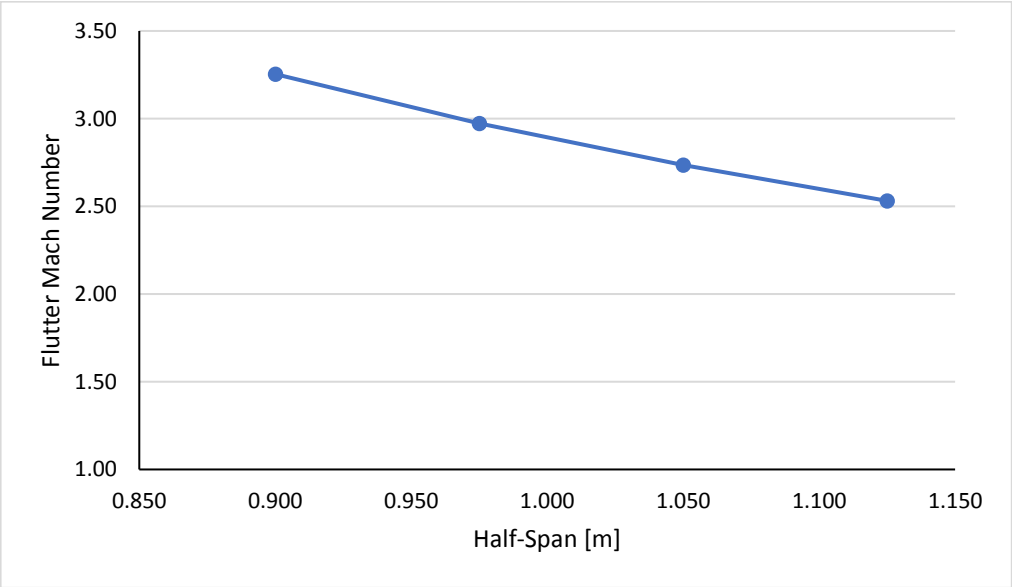

Figure 3.5 Flutter Speed versus Half Span

3.2.2 Effect of Beam Cross Section of the Wing on the Supersonic Flutter Speed

As explained in Section 3.1, the finite wing model consists of a plate with stiffeners at each side. The stiffeners are modeled as beams and their cross-sectional area is modified to see how this parameter influences the supersonic flutter speed. Initially, a modal analysis is conducted for the finite wing using MSC. Nastran for each variation and the modal frequency results are given in Table 3.3.

Table 3.3 Comparison of Modal Frequencies w.r.t. Beam Area of the Side Stiffeners

$t_a * t_b$ [m^2]	1st Bending [Hz]	1st Torsion [Hz]
$0.01 * 0.025$	10.6	52.4
$0.01 * 0.030$	13.2	55.1
$0.01 * 0.035$	15.9	57.5
$0.01 * 0.040$	18.8	59.7

The results show that the increase in the beam area results in an increase in both the bending and torsion frequencies. Stiffeners when modeled as beams are capable of taking axial, bending, and shear loads, in addition to moments and torsional or twisting or torque loads. This results in them being able to account for large deflections and increasing the stiffness of the structure. Therefore, the increase in the natural frequencies observed in Table 3.3 is an expected result, since the increase in the stiffener area results in a more stiff structure.

The effect of the beam cross-sectional area of the side stiffeners is included in the calculation of the supersonic aerodynamic force and moments. The mass per unit length (A_w) and the mass moment of inertia (M_w) of the wing which are directly affected by the stiffener area are included in the aerodynamic load expressions as seen in Equations (2.68) - (2.81). The effect of this combined with the increase in the stiffness of the wing with increasing beam area results in a variation of flutter speed as seen in Figure 3.6. The results show that the code was successful in correctly predicting the increase of the flutter speed with the increase in the cross-sectional area.

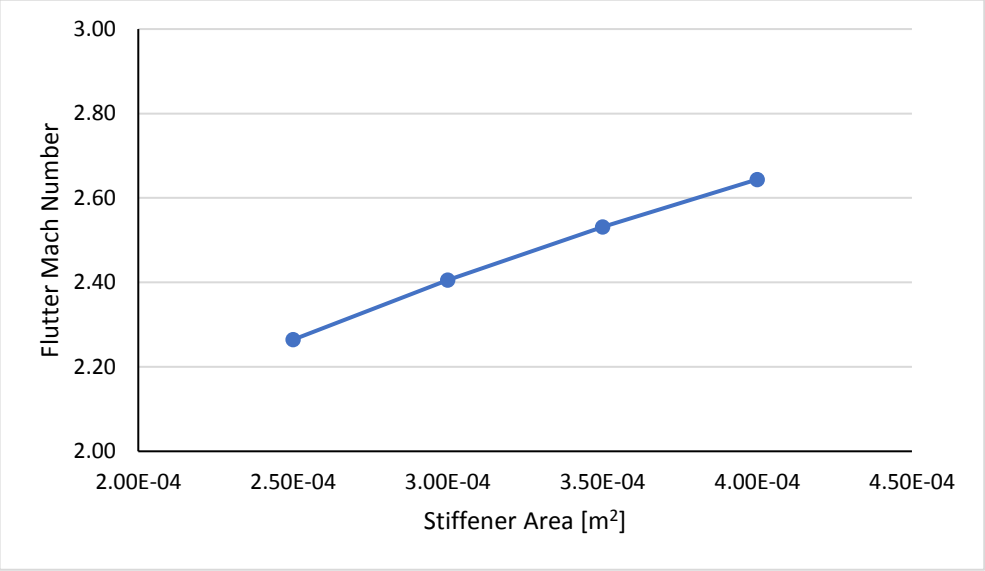

Figure 3.6 Flutter Speed versus Beam Area of the Side Stiffeners

3.2.3 Effect of Material of the Wing on the Supersonic Flutter Speed

Finally, the modulus of elasticity is changed and its effect on the flutter speed is observed. The modal frequencies of the various finite wing configurations of modulus of elasticity which are calculated in MSC. Nastran can be observed in Table 3.4. Equation (3.9) shows that the bending frequency is proportional to the square root of the elastic modulus. Moreover, in Equation (3.10), the frequency is related to the shear modulus which is $G = E/2(1 + \nu)$, relating the torsional frequency to the elastic modulus. Therefore, the results in Table 3.4, which show the increase of the bending and torsional stiffness with the increasing modulus of elasticity, is an expected outcome.

Table 3.4 Comparison of Modal Frequencies w.r.t. Modulus of Elasticity

***E* [Pa]**	**1st Bending [Hz]**	**1st Torsion [Hz]**
60 000	14.8	55.7
65 000	15.4	56.6
70 000	15.9	57.5
75 000	16.5	58.4

Same as in Section 3.2.1, the elastic modulus parameter does not show itself on the aerodynamic force and moment equations. Therefore, the flutter speed is affected from the modulus of elasticity parameter in the way that the stiffness is varied. The modulus of elasticity is about the tendency of a structure to deform when opposing forces are applied and is associated with the stiffness of a structure. As a result, as the modulus of elasticity is increased, the bending and torsional stiffness characteristically also show an increasing trend. Figure 3.7 shows the results consistent with this remark, leading to an increase of flutter speed with the increasing modulus of elasticity.

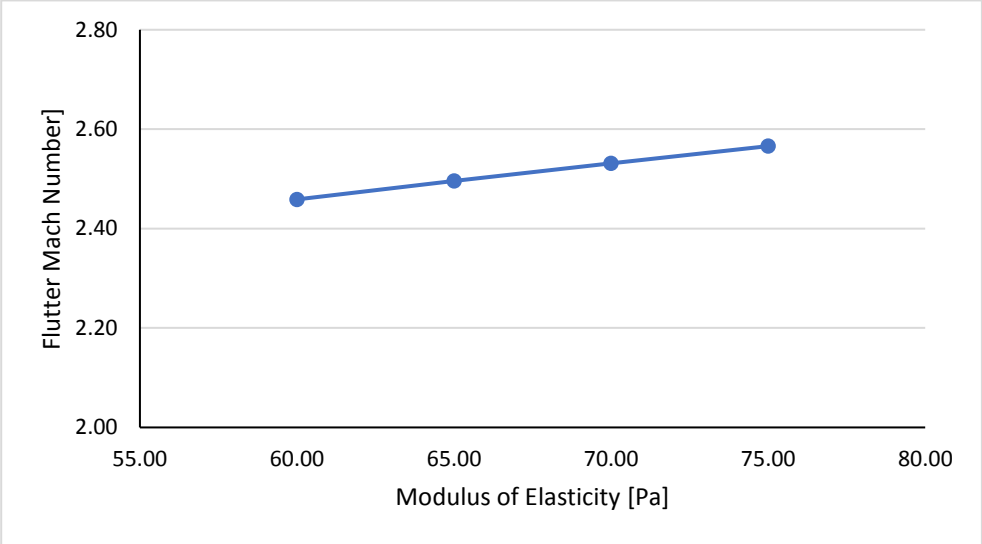

Figure 3.7 Flutter Speed versus Modulus of Elasticity

3.3 Comparison of the Code Results with ZAERO

The flutter estimation of a finite wing using the typical section supersonic aerodynamics are given in Section 3.2 as a parametric study. In this section, the results of the parametric study are compared to supersonic flutter analysis results obtained by ZAERO [34]. ZAERO is a commercial aeroelastic tool whose capabilities include solution of supersonic flutter analysis. The ZAERO analysis procedure is explained in further detail in Chapter 4.

The comparison for the supersonic flutter analysis are presented in Figure 3.8 - 3.10. The flutter speeds are normalized with respect to the lowest flutter speed obtained for each configuration such that the minimum flutter speed for each case becomes 1. It

can be observed from the plots that the increasing or decreasing trends are reflected in the ZAERO results as well as in the code results.

The results show that, although, an exact flutter speed may not be calculated with the use of the two dimensional supersonic flutter analysis code created in this study, the effects of various parameters on the flutter speed can be observed. As a result, this code can be used for the evaluation of different design cases in a iterative design phase during which frequent design changes are made and the effect of design changes on the trend of the flutter speed is needed. Percent changes of the flutter speed corresponding to the design changes can be predicted with the 2D code and costly aeroelastic analysis can be avoided. Moreover, when a reliable flutter speed for a single case is known, flutter speed corresponding to a wing configuration with modified design parameter can also be estimated with the use of the two dimensional supersonic flutter analysis code developed without the need of various costly aeroelastic analyses to be carried out.

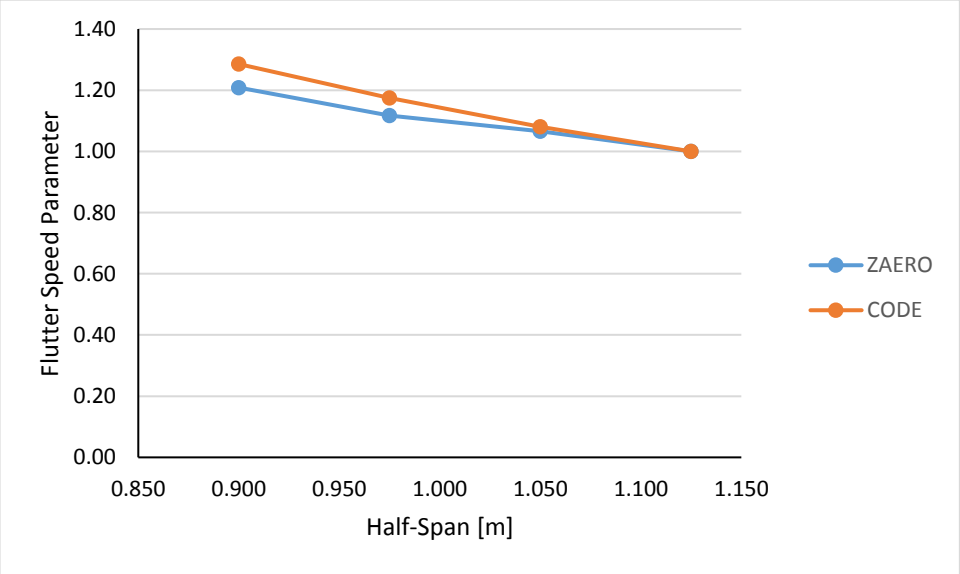

Figure 3.8 ZAERO and Code Comparison for Half-Span Variation

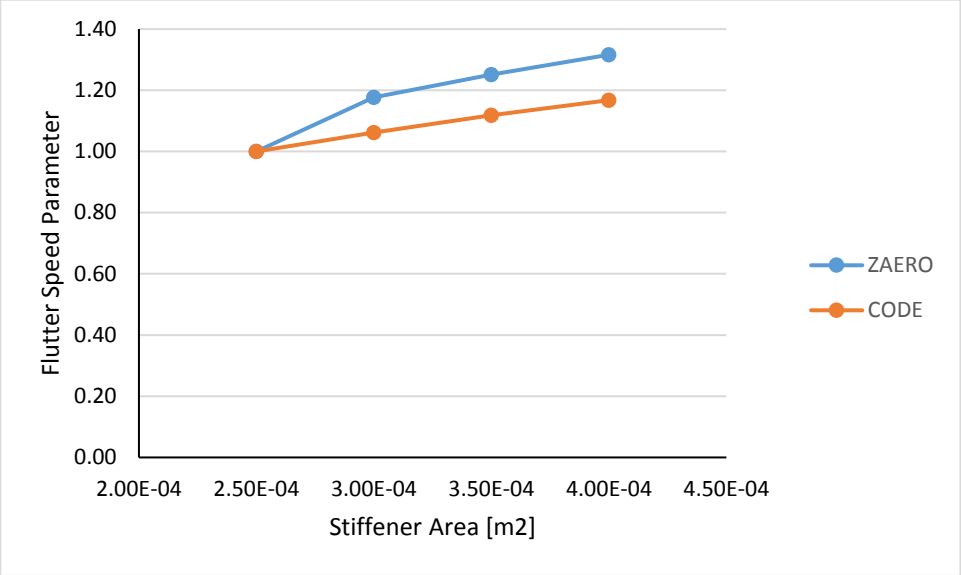

Figure 3.9 ZAERO and Code Comparison for Stiffener Area Variation

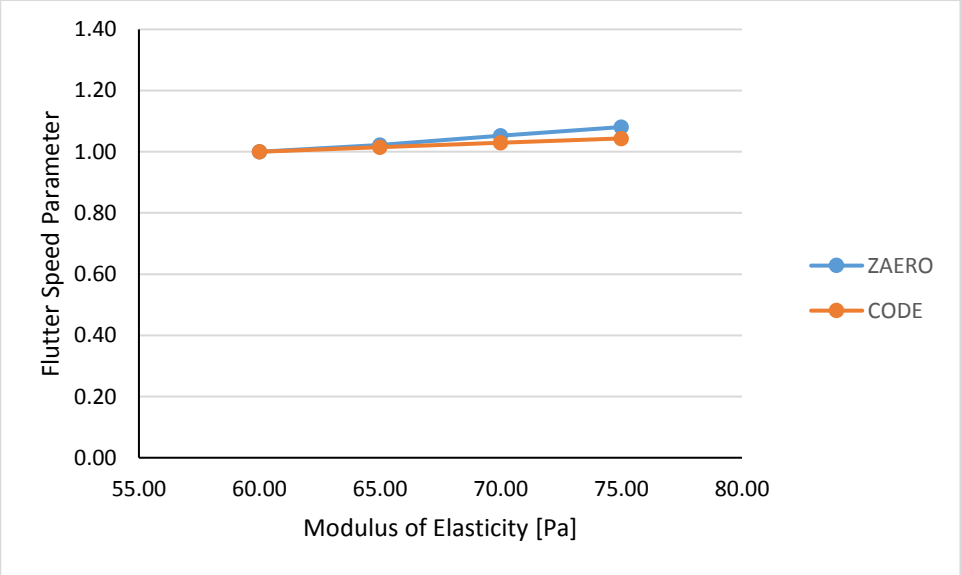

Figure 3.10 ZAERO and Code Comparison for Half-Span Variation

CHAPTER 4

SUPERSONIC FLUTTER ANALYSIS USING ZAERO

4.1 General Review of the Flutter Calculation Process of ZAERO

ZAERO is a commercial software developed by ZONA Technology INC for the purposes of solving all kinds of aeroelastic problems that range from static aeroelastic/trim analysis to aeroservoelasticity [34]. An important feature of the ZAERO software is that it can generate Unified Aerodynamic Influence Coefficient (UAIC) matrices for full aircraft configurations. This solution can be done for all Mach numbers that is covered by the five aerodynamic methods that are detailed in Figure 4.1. In the scope of this study, ZONA7 ($M > 1$) is used to formulate the supersonic aerodynamics for the lifting surfaces.

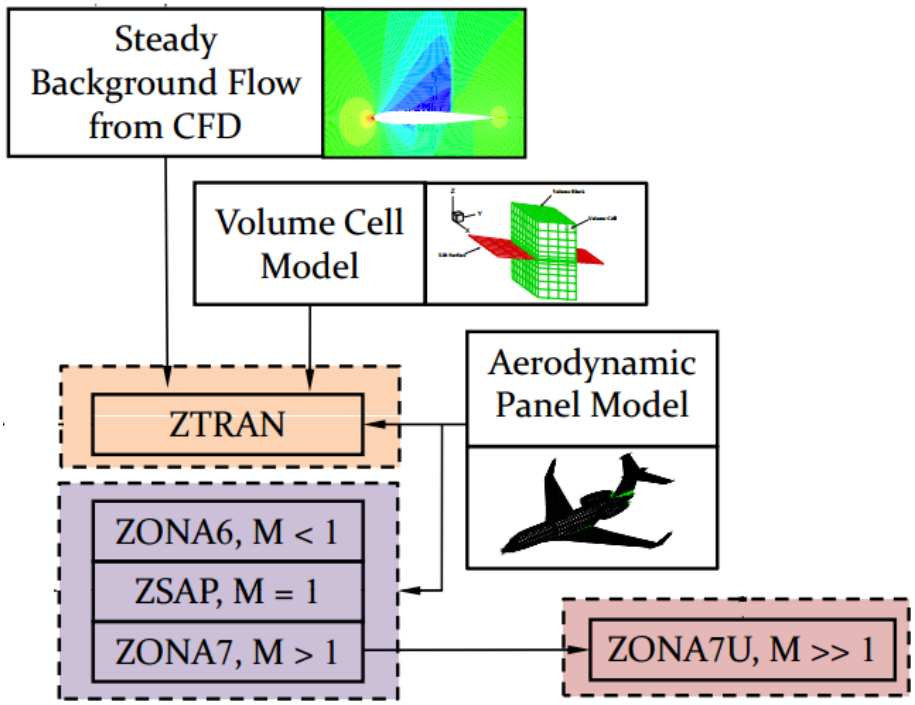

Figure 4.1 Capability of the ZAERO UAIC Module [34]

ZAERO does not provide the structural finite element solution, therefore the computed normal modes solution is externally imported to the program. The Model Data Importer is a module that can process the output files of the commercial programs which have the computed structural free vibration data. In this study, the structural stiffness, mass, and damping matrices required by the aeroelastic analyses are generated by MSC. Nastran and saved in the Nastran output file (.f06). The Modal Data Importer reads these output files to get the information of the structural grid point locations for the spline calculation, the mode shapes, the natural frequencies, the generalized mass and the stiffness matrices of the structural finite element model.

The unified aerodynamic influence matrix is constructed from the geometry of the aerodynamic finite elements whose aerodynamic grids are independent from the structural grids of the FEM. In this thesis study, the panel formulation for the lifting surfaces is generated by the supersonic unsteady aerodynamic module ZONA7.

With the data obtained from the Nastran output (.f06) file, a structural spline is created to link the aerodynamic and the structural models by generating a transformation matrix relating the deflections of the aerodynamic and the structural grids.

The generalized aerodynamic loads are calculated for different reduced frequencies with the multiplication of the UAIC with downwash resulting from harmonic oscillation of the eigenmodes. The flutter solver evaluates the equations of motion for the frequency and damping coefficients within a specified flight envelope. The results such as the flutter boundary envelopes, the interpolated structural mode on the aerodynamic model or the mode at which flutter occurs can be converted for visualization into external post-process software including TECPLOT, MSC. Patran and Excel. This flutter analysis process chain is described schematically in Figure 4.2.

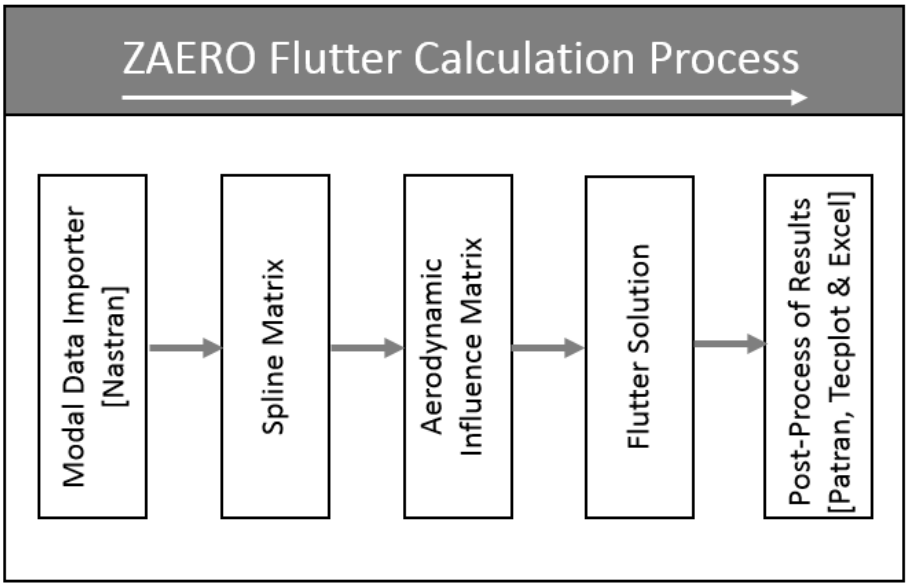

Figure 4.2 The Process of Flutter Calculation in ZAERO

4.2 Generation of the Supersonic Aerodynamic Influence Coefficient Matrix

ZONA7 is the module that generates the Aerodynamic Influence Coefficient (AIC) Matrix in the supersonic Mach number range. As previously stated, simple harmonic motion is assumed such that the unsteady aerodynamic methods can be solved in the reduced frequency domain. Panel method is used to obtain the aerodynamic equation, which requires the aircraft model to be divided into small panels defined as aerodynamic boxes. Each of these boxes have a control point where the boundary condition is defined. The equations belonging to each box is individually derived and assembled together to approximate the entire aircraft equation. The coefficients of these added equations represent the aerodynamic effect of aerodynamic boxes to

control points and the assembled matrix is called the Aerodynamic Influence Coefficient Matrix.

ZONA7 [34] bases its aerodynamic calculations on the linearized small disturbance equation given as follows,

$$(1-M^2)\Phi_{xx}+\Phi_{yy}+\Phi_{zz}-2\frac{M}{c}\Phi_{xt}-\frac{1}{c^2}\Phi_{tt}=0 \tag{4.1}$$

where Φ is the total velocity potential that can be divided into the steady and unsteady potential as $\Phi=\phi_0+\phi_1$ and c is the speed of sound. With this assumption and the fact that Equation (4.1) is a linear equation, Equation (4.1) can be decoupled to steady and unsteady linearized small disturbance equations. Then, assuming simple harmonic motion, the unsteady potential equation can be re-expressed by assuming the total velocity potential as;

$$\phi=\bar{\phi}e^{i\lambda Mx'} \tag{4.2}$$

where

$$\lambda=\frac{kM}{\sqrt{|1-M^2|}} \tag{4.3}$$

$$k=\frac{wL}{V} \tag{4.4}$$

$$x'=L\sqrt{|1-M^2|}\,x \tag{4.5}$$

where V is the main stream velocity, M is the main stream Mach number, L is the reference length, w is the oscillation frequency and k is the reduced frequency.

Introducing Equation (4.2) into the unsteady linearized small disturbance equation and applying Green's theorem results in an integral solution in terms of the unsteady source and doublet singularity distributions over a surface of the related configuration. This

derivation is explained in more detail in Reference [34]. For solving the integral equation, ZONA7 makes use of the panel method.

There are two types of panel modelling available in ZAERO. The wing-like components are used to model any thin surface whose spanwise cross-section can be an airfoil such as wings, canards, tails, pylons etc. The body-like components are the parts that do not fall into the previous category such as fuselage, engine intake, external stores, etc. For the purpose of this study, wing-like components are utilized to model the wing. The wing-like components are assumed to be flat plate since the in the assumption of thin lifting surfaces, the thickness influence is rather small for the unsteady linear aerodynamics. To generate the lift, doublet singularity is utilized where source singularity is used to model the thickness effects; therefore, source singularity is not distributed on the wing-like components leading to the supersonic potential influence of the wing-like components to be;

$$\phi_W = \frac{1}{2\pi} \iint \Delta\phi(x,y,z) e^{i\lambda M\xi} \frac{\partial}{\partial n} K dS \tag{4.6}$$

where K is the Supersonic Kernel function, n is the out-normal vector, and S represents the surface of the configuration of interest. The acceleration potential transformation is performed on Equation (4.6) leading to it being expressed directly in terms of ΔC_p as follows [34];

$$\phi_W(x_0,y_0,z_0) = \frac{\beta}{4\pi} \iint \Delta C_p(x,y,z) e^{ik\beta\xi} \overline{K}(\xi,\eta,\zeta) dS \tag{4.7}$$

where

$$\beta = \sqrt{|1 - M^2|} \tag{4.8}$$

$$\xi = \left(\frac{x - x_0}{\beta L}\right) \tag{4.9}$$

$$\eta = \left(\frac{y - y_0}{L}\right) \tag{4.10}$$

$$\zeta = \left(\frac{z - z_0}{L}\right) \tag{4.11}$$

$$\overline{K} = -\int_{\sqrt{\eta^2+\zeta^2}}^{\xi} \frac{e^i k}{\beta} \tau \frac{\partial K}{\partial n} d\tau \tag{4.12}$$

where (x_0, y_0, z_0) are the field point to be influenced and (x, y, z) are the sending points from the sources and doublets.

The integrals of this new equation can be divided into many simple equations for each aerodynamic box and the Aerodynamic Influence Matrix (AIC) can be constructed. The detailed derivations can be found in Reference [34].

Finally, the influence of the displacements $\{h\}$ of the aerodynamic panels on the aerodynamic forces $\{F_h\}$ can be expressed as;

$$\{F_h\} = q_\infty [AIC]\{h\} \tag{4.13}$$

where q_∞ is the dynamic pressure. Furthermore, the vectors $\{h\}$ and $\{F_h\}$ can also be defined as the mode shapes and the force vectors on the wing box, respectively.

Figure 4.3 shows a typical modelling of a wing-like component. The solid circles are the control points where the boundary conditions act on. The control points that lie at the mid-span of each wing box are located at 85% of the wing box chord for subsonic Mach numbers and at 95% of the wing box chord for supersonic Mach numbers. The lines represent the vortex generated by the elements. Each strip sheds two vortex lines from its side edges that start at the trailing edge and shed downstream. However, at edges shared by two adjacent strips, the strength of the two vortex lines partially cancel each other. Due to the singular behavior of the vortex line, several restrictions must be applied while modeling the wing-like components. Since, in the scope of this study, only a half-wing model is used these restrictions are not applicable, thus they are not

explained. While modelling full aircrafts they should be taken into account and are explained in detail in Reference [34].

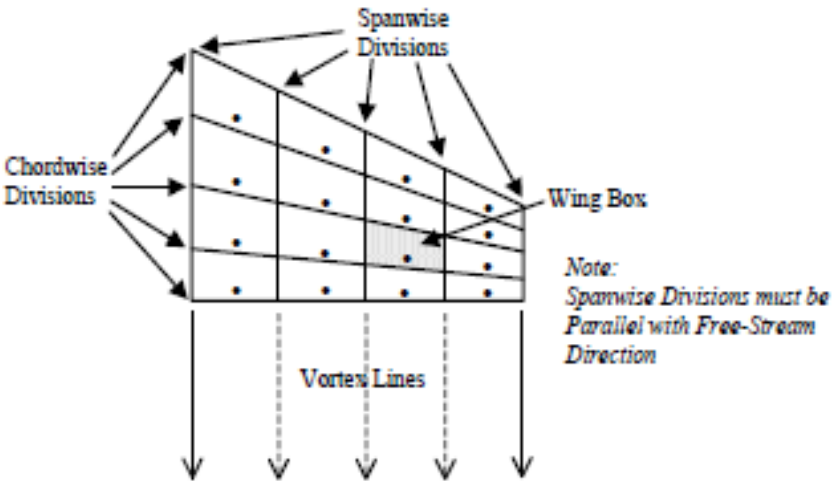

Figure 4.3 Wing-Like Modelling in ZAERO [34]

4.3 Interconnection of the Structure with Aerodynamics

The ZAERO aerodynamic model covers the outer surface of an aircraft whereas, the structural Finite Element Model takes into account not only the outer geometry but also the internal load carrying components. In this sense, these two models are different types of representations therefore; the displacement and force transferal between them are not straightforward. A spline matrix is introduced to relate the aerodynamic to the structural degrees of freedom.

The finite element model for an aircraft has many degrees-of-freedom leading to a large mass and stiffness matrices. Hence, a modal approach is introduced that reduces the size of the eigenvalue flutter problem to the modal coordinates in order to reduce the time and cost needed to compute the flutter problem in all degrees-of-freedom.

Defining the $\{h\}$ vector as the displacements of the aerodynamic box and the $\{x\}$ vector as the structural deformations, the spline matrix $[G]$ can be defined as follows;

$$\{h\} = [G]\{x\} \tag{4.14}$$

In addition, the structural $\{F_a\}$ and the aerodynamic $\{F_h\}$ forces can be related to each other as follows [34];

$$\{F_a\} = [G]^T\{F_h\} \tag{4.15}$$

Equation (4.15) shows that the transpose of the spline matrix is sufficient to connect the aerodynamic forces to the structure. The transformation process given by Equation (4.14) can be described as interpolating the displacements at the structural finite element grid points to the aerodynamic grid points, and the transformation process given by Equation (4.15) is the interpolation of the forces at the aerodynamic grids to the structural grids.

ZAERO offers various spline methods however, in this study, the Infinite Plate Spline (IPS) method is used since this is a 2D interpolation method, which is suitable for wing-like components [34].

4.4 Flutter Solution Analysis, the G-Method

The ZAERO flutter module contains two flutter solution techniques which are the K-method and the g-method. The g-method introduced by Chen [35], is a flutter solution method that generalizes the K-method and the P-K method for true damping prediction and can be considered as an extension of the widely used P-K method. It is based on the assumption that by adapting the damping perturbation method, a first order term derived from the Laplace domain aerodynamics can be included in the unsteady aerodynamic equation as follows;

$$Q(p) \approx Q(ik) + g\frac{\partial Q(p)}{\partial g}\bigg|_{g=0} \approx Q(ik) + gQ'(ik) \tag{4.16}$$

where $[Q(ik)]$ is the generalized aerodynamic force matrix and $p = g + ik$ is the non-dimensional Laplace parameter.

The g-method equation, whose derivation is explained in more detail in Reference [34], is given by;

$$\left[\left(\frac{V}{L}\right)^2 [M]p^2 + [K] - q_\infty[Q'(ik)] - q_\infty[Q(ik)]\right]\{q\} = \{0\} \tag{4.17}$$

where V is the mainstream velocity, L is the reference length, $[M]$ is the generalized mass matrix, $[K]$ is the generalized stiffness matrix and q_∞ is the dynamic pressure.

ZAERO calculates the flutter frequency w_f and damping 2γ at the reduced frequency where $Im(g) = 0$ from the equations;

$$w_f = k\frac{V}{L} \tag{4.18}$$

$$2\gamma = 2\frac{Re(g)}{k} \tag{4.19}$$

A sample damping velocity curve is given in Figure 4.4. When damping is negative, the structure is feeding energy into the vibration resulting in stable aeroelastic modes. When the damping curve passes from negative to positive the mode becomes unstable resulting in that point to be the flutter velocity. Furthermore, the slope of the damping vs velocity curve where it passes through the flutter point is a qualitative measure of how violently the oscillations would happen during flight.

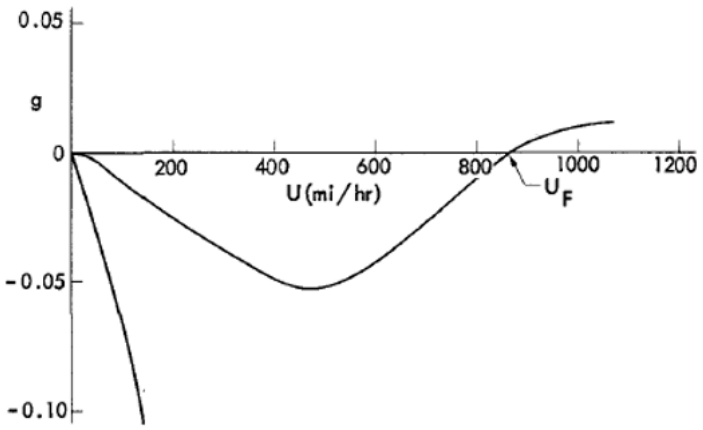

Figure 4.4 Sample Damping- Velocity Plot [1]

Furthermore, ZAERO has the capability to perform flutter analysis based on different configurations of flight conditions as shown in Table 4.1. In this study, FIXHATM and FIXMATM are used to conduct the flutter analyses by ZAERO.

Table 4.1 Flutter Solution Methods Available in ZAERO [34]

ZAERO Card	Definition	Flutter Analysis Performed
FIXHATM	Fixed altitude but varying Mach number	Matched Point Analysis
FIXMATM	Fixed Mach number with varying altitudes	Matched Point Analysis
FIXMACH	Fixed Mach number with varying velocity and density pairs	Non-Matched Point Analysis
FIXMDEN	Fixed Mach number and density with varying velocities	Non-Matched Point Analysis

4.5 Using ZAERO to Find the Flutter Speed of the Weakened AGARD 445.6 Wing

The AGARD 445.6 wing is a standard aeroelastic wing, which is created for validating the flutter results of any numerical method with the corresponding experimental data obtained from the Langley dynamics tunnel. The AGARD 445.6 wing is modeled as a panel, which has an aspect ratio of 1.6525, taper ratio of 0.6576, a quarter-chord swept angle of 45° and a NACA 65A004 airfoil section [36]. Even though various wing configurations were tested, the most commonly used test case in computational aerodynamic problems is the weakened wing model. This model has a reduced stiffness achieved by drilling holes through the wing and filling the spaces with foam plastic in order to maintain aerodynamic continuity.

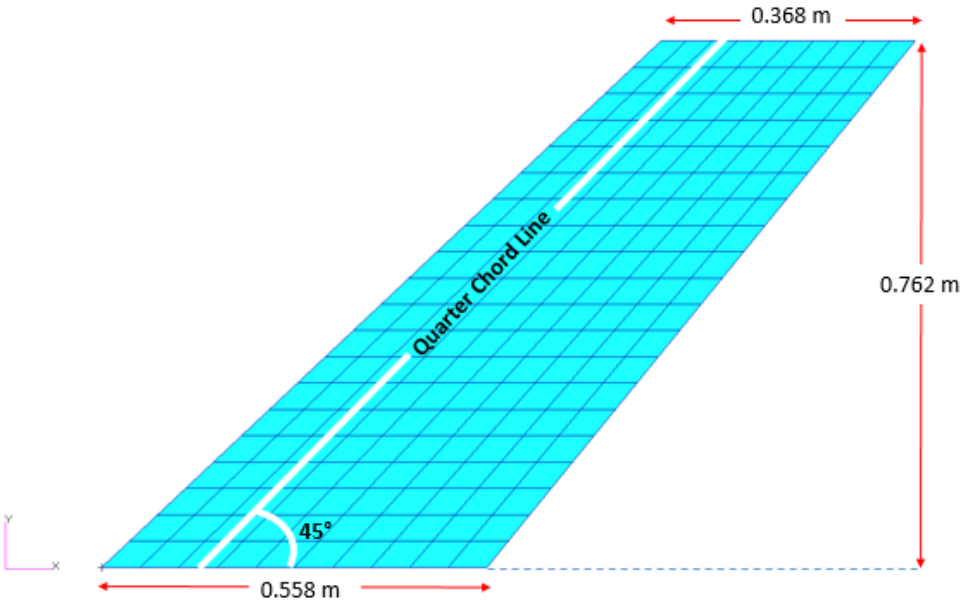

Figure 4.5 Structural FEM of the Weakened AGARD 445.6 Wing

The wing created for this study is given in Figure 4.5. The wing is modeled with CQUAD4 shell elements with single orthotropic material with the attributes given in Table 4.2. The airfoil cross-section is defined by assigning the appropriate thickness to the shell elements along the chordline.

Table 4.2 Properties of the Material of the AGARD 445.6 Wing [37]

Parameter	**Definition**	**Value**
E_1	Longitudinal Modulus of Elasticity	3.15 GPa
E_2	Lateral Modulus of Elasticity	0.42 GPa
ν	Poisson's Ratio	0.31
G	Shear Modulus	0.44 GPa
ρ	Wing Density	381.9 kg/m^3

MSC. Nastran is used to compute the natural frequencies of the wing model. Figure 4.6 shows the first four mode shapes of the model created and Table 4.3 shows the comparison of the calculated natural frequencies with the experimental data given in Reference [36].

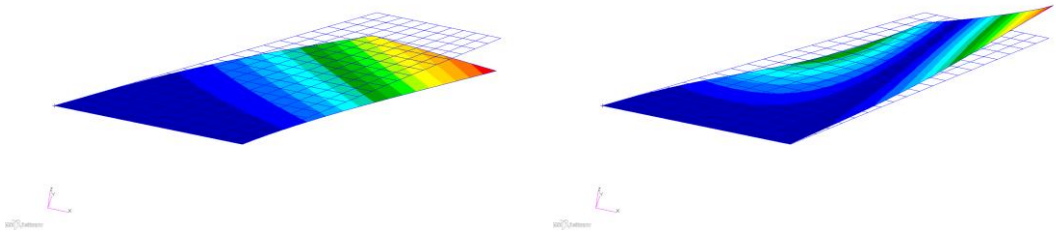

Mode 1 (1st Bending Mode) Mode 2 (1st Torsion Mode)

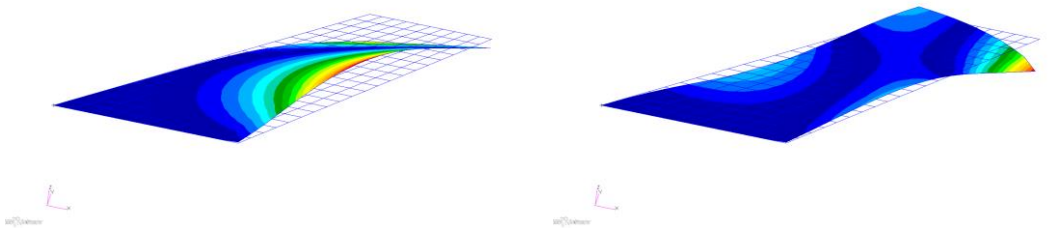

Mode 3 (2nd Bending Mode) Mode 4 (2nd Torsion Mode)

Figure 4.6 Weakened AGARD 445.6 Mode Shapes

Table 4.3 Comparison of Natural Frequencies of the Weakened AGARD 445.6 Wing

Wing Models	**Mode 1 [Hz]**	**Mode 2 [Hz]**	**Mode 3 [Hz]**	**Mode 4 [Hz]**
Numerical	9.46	39.67	49.45	95.10
Experimental	9.60	38.10	50.70	98.50

The wing-like aerodynamic model created with ZAERO and plotted with TECPLOT is given in Figure 4.7. The outer dimensions are consistent with the structural model. There are 10 elements chordwise and 25 elements in the spanwise direction leading to a model with 250 aerodynamic elements in total.

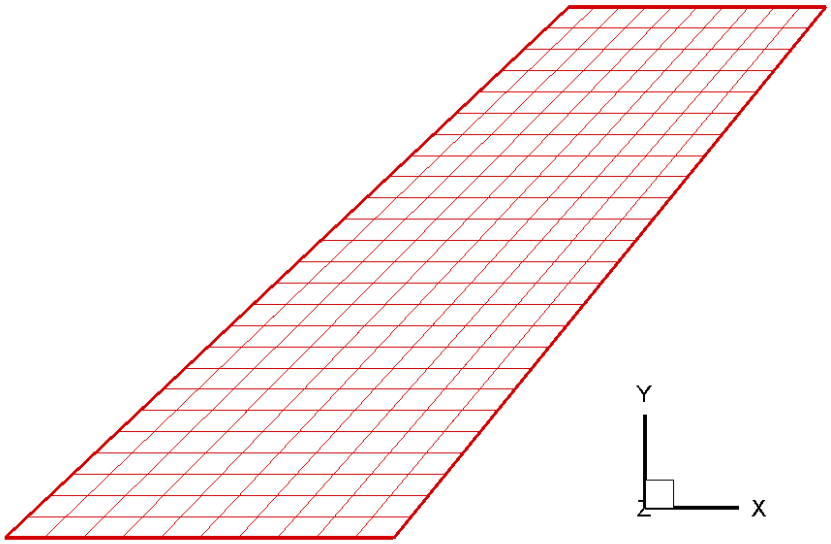

Figure 4.7 Aerodynamic Model of the Weakened AGARD 445.6 Wing

For the splines, all the structural grids in the model are included to have a conservative approach in terms of the connection of the aerodynamic and structural models. Considering that the model is a relatively small one, inclusion of the entire structural grid group does not lead to an analysis which is time-consuming. However, this approach will lead to unnecessary computational time for larger models, therefore; a less number of grids should be chosen, and the interpolated structural mode shapes should be plotted on the aerodynamic model to check the efficiency of the spline. For this model, Figure 4.8 gives the motion of the aerodynamic grids for the first and second free vibration modes. Comparison of Figure 4.6 with Figure 4.8 shows that a successful interpolation is attained by the present spline input. Hence, spline verification has been performed successfully.

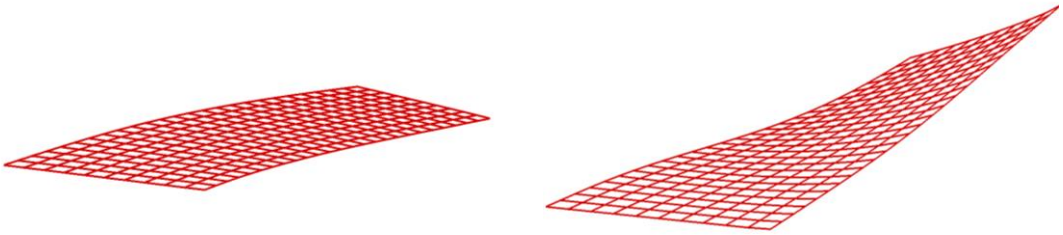

Mode 1 (1st Bending Mode) Mode 2 (1st Torsion Mode)

Figure 4.8 Spline Verification Performed for the First and the Second Structural Free Vibration Modes

In all flutter calculations, the first four natural frequencies are employed. The structural damping is set to zero. The analysis is conducted in air conditions where the term ρ represents the air density. The inputs of the ZAERO flutter analysis given are consistent with the experimental data [36] as seen in Table 4.4. M is the mainstream Mach number, ρ is the air density, μ is the wing density parameter, w_a is the first torsional natural frequency and b is the half-chord length.

Table 4.4 Inputs for the Flutter Analysis

M	ρ [kg/m^3]	μ	w_a [rad/s]	b [m]
0.499	0.428	33.47	249.25	0.279
0.678	0.208	68.75	249.25	0.279
0.901	0.099	143.92	249.25	0.279
0.954	0.063	225.82	249.25	0.279
1.072	0.055	259.59	249.25	0.279
1.141	0.078	182.74	249.25	0.279

The wind tunnel test results are presented in terms of a non-dimensional flutter speed index (FSI) defined in Equation (4.20). Therefore, the flutter speed (V_f) obtained from ZAERO is also given in terms of this parameter as follows;

$$FSI \rightarrow \frac{V_f}{bw_a\sqrt{\mu}} \tag{4.20}$$

The results are given in Figure 4.9 and Table 4.5. These comparisons show good agreement in flutter characteristics for free-stream Mach numbers below one. The transonic dip predicted by the experimental methods is also reflected in the results. However, in the supersonic range, the computed results over predict the flutter boundary. This phenomenon of the premature rise of the FSI determined in the supersonic range is also observed in other computational aerodynamics methods in literature such as Navier-Stokes [38] and Euler Aerodynamics [39]. This effect could be credited to the fact that structural damping is not included in the ZAERO analysis whereas these effects are inherently included in the experimental results.

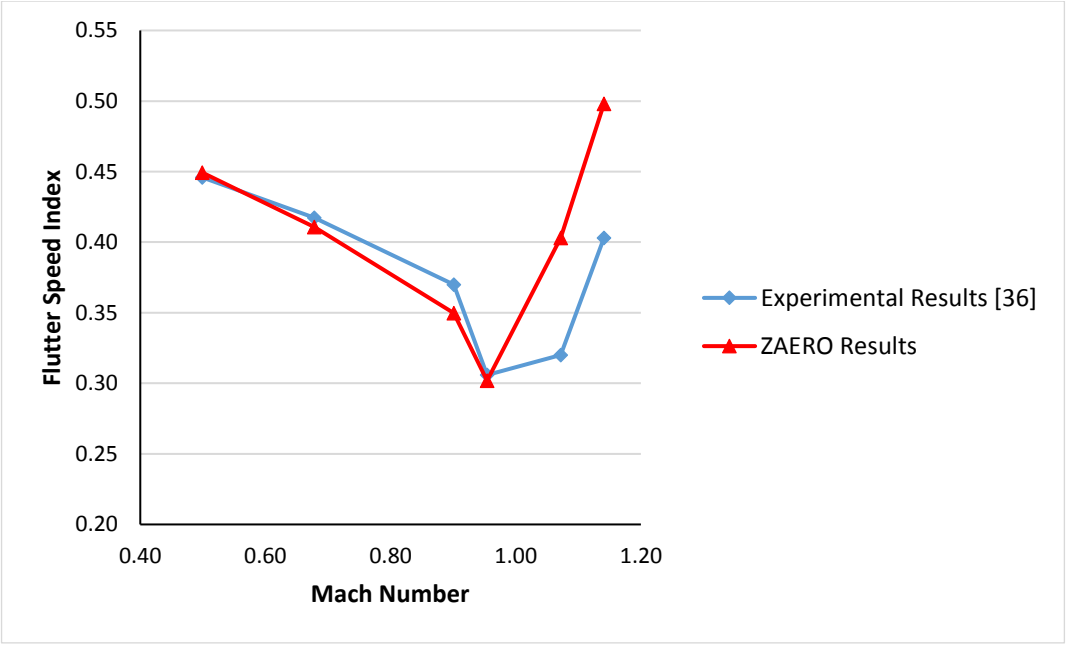

Figure 4.9 Comparison of the Experimental and ZAERO Results

Table 4.5 Tabular Comparison of the Experimental and ZAERO Results

M	**EXPERIMENTAL FSI**	**ZAERO FSI**
0.499	0.4459	0.4493
0.678	0.4174	0.4107
0.901	0.3700	0.3497
0.954	0.3059	0.3019
1.072	0.3201	0.4031
1.141	0.4031	0.4981

CHAPTER 5

FLUTTER ANALYSIS OF A FIGHTER WING

5.1 Modelling of a Fighter Wing

The structural finite element model of a generic fighter wing is modelled using MSC. Nastran [32].The internal layout of the wing FEM is modified for various configurations while keeping the external geometry constant as well as the modelling approach. The concept of the wing is determined to be conventional with a moderate aspect ratio, tapered in the leading edge and no taper in the trailing edge. Moreover, twist or dihedral effects are not included. The airfoil section is kept constant throughout the span of the wing. The interest of the study is the supersonic flutter that results as a coupling of the bending and torsion modes and the effect of other degrees of freedom are not investigated. As a result, control surfaces are not modelled since this process would be redundant as their modal frequencies is not a part of the study. Furthermore, in the conceptual design phase, the control surfaces are not usually not included in the aeroelastic analysis, as their design is not mature enough.

Figure 5.1 illustrates the airfoil chosen which is the NACA63-412. The geometrical dimensions of the wing is shown in Figure 5.2.

Figure 5.1 Airfoil Geometry of the Wing

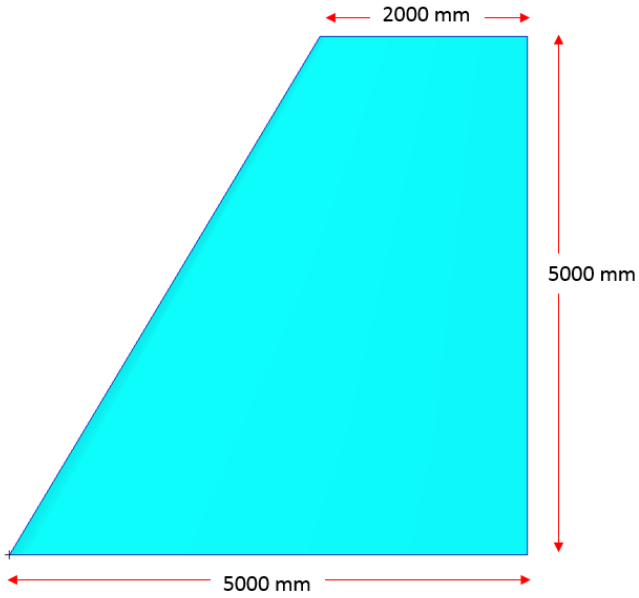

Figure 5.2 Wing Dimensions

The baseline model consists of five ribs and three spars. A coarse meshing strategy is applied for every configuration at this study which is further explained in Section 5.2. All components are modeled with shell elements and their corresponding thickness and material attributes are defined by different properties according to their geometric attributes. Figure 5.3 shows the internal layout for the baseline wing model.

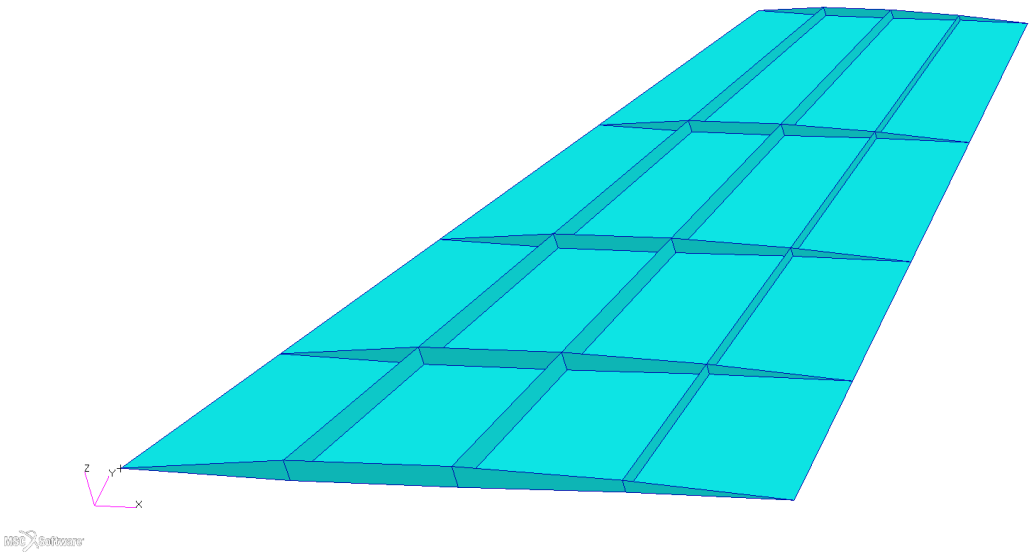

Figure 5.3 Internal Layout of the Baseline Wing Model

Table 5.1 lists the material properties used for the structural elements of the wing and Table 5.2 lists the properties of the components of the wing FEM. The total weight of the wing FEM is 217.93 kg.

Table 5.1 Isotropic Material Properties of the Structural Elements of the Wing [40]

Material	**Density, ρ [kg/m^3]**	**Modulus of Elasticity, E [MPa]**	**Poisson's Ratio, ν**
2024-T851	2795.7	74 463	0.33
7475-T7351	2795.7	72 050	0.33
7075-T73	2795.7	70 327	0.33

Table 5.2 Material Properties of the Components of the Wing

Component	Material	Thickness [mm]	Element Type	Weight [kg]
Upper Wing Skin	2024-T851	2	CQUAD4	97.87
Lower Wing Skin	7475-T7351	2	CQUAD4	98.19
Spars	7475-T7351	3.5	CQUAD4	17.37
Ribs	7075-T73	1	CQUAD4	4.49

For the wing to fuselage attachment, the most appropriate boundary condition is the cantilever boundary condition. The wing is attached to the fuselage at grids associated with the spars. All the corresponding nodes are given zero translation in all directions and zero rotation about x-axis as shown in Figure 5.4.

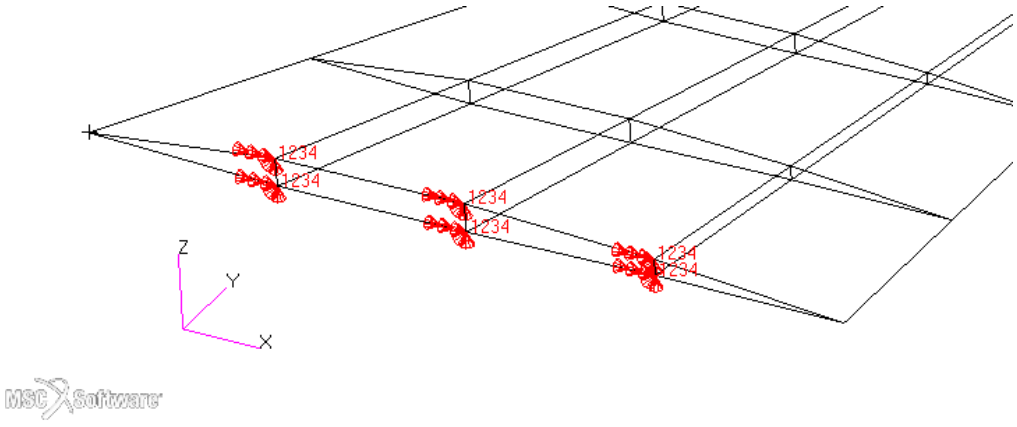

Figure 5.4 Boundary Conditions on the Attachment Points of the Wing

The modal analysis is conducted using MSC. Nastran for all the configurations studied. In terms of flutter analysis the bending and torsion degrees-of-freedom are taken into account and the mode shapes for these modes of the baseline model are given in Figure 5.5 and Figure 5.6.

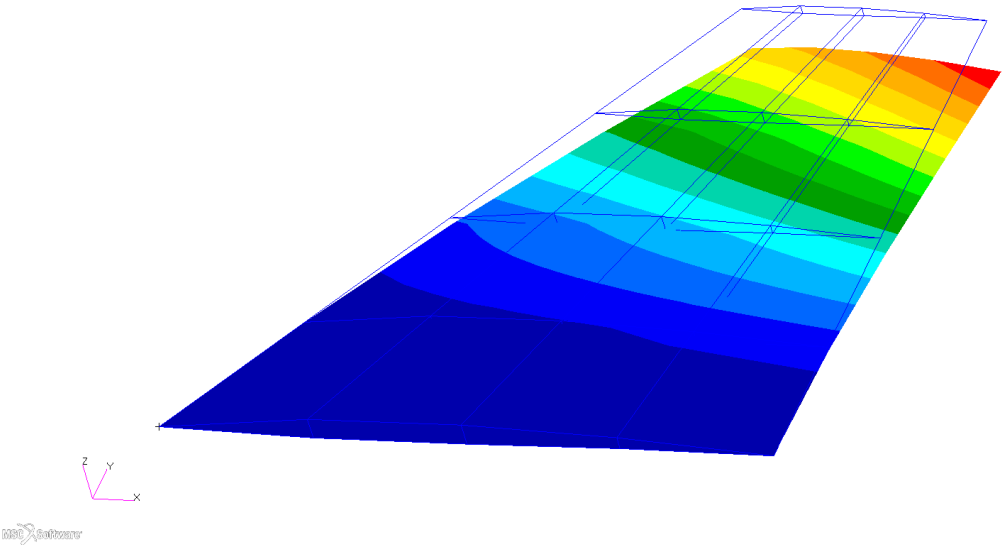

Figure 5.5 Bending Mode of the Baseline Wing Model [7.55 Hz]

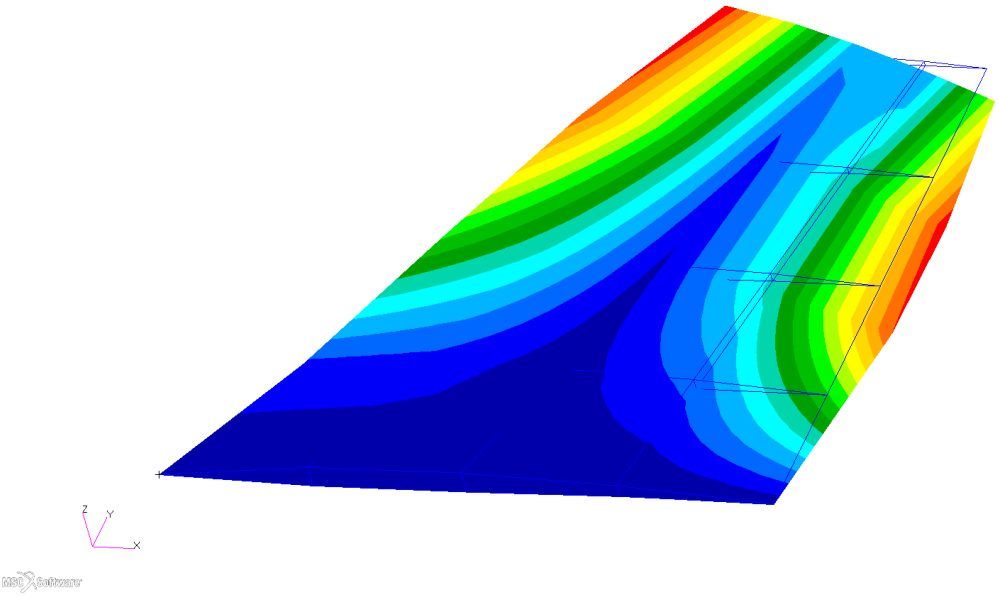

Figure 5.6 Torsion Mode of the Baseline Wing Model [22.53 Hz]

As previously explained, the aerodynamic lifting surfaces are modelled using wing-like components. The same aerodynamic model can be utilized for all the wing configurations studied since the external geometry is not modified throughout the process. The chordwise spacing of aerodynamic panels is concentrated near the leading and trailing edges similar to a CFD grid distribution. The reason being that these sections are subjected to high pressure gradient and the finer model is more accurate in capturing the high pressure gradient. There are 8 elements spanwise and 12 aerodynamic panel elements chordwise resulting in 96 aerodynamic elements. The TECPLOT representation of the aerodynamic model is given in Figure 5.7.

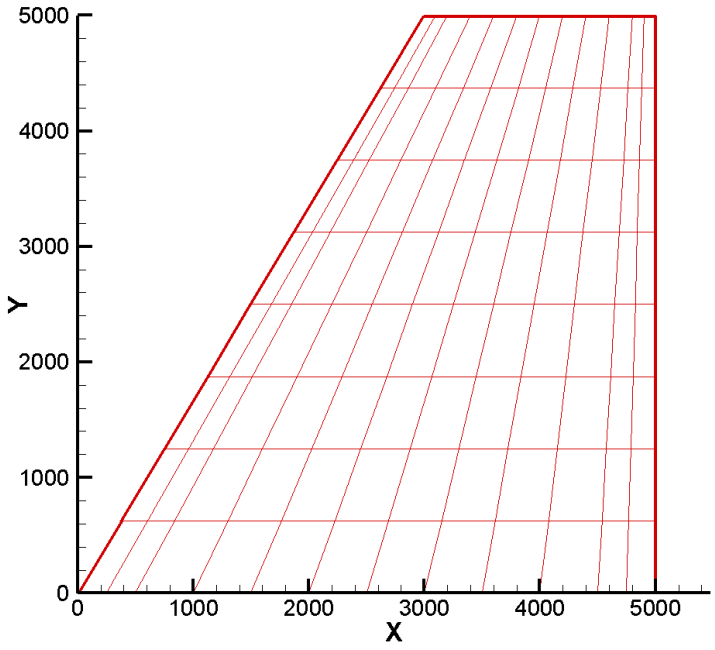

Figure 5.7 The ZAERO Aerodynamic Model of the Wing

Following the generation of the aerodynamic model, splines are created to interpolate from the structural to aerodynamic degrees-of-freedom. Two or more grid points can be projected onto the same location on the plane of an element. To avoid a singular interpolation matrix, only one grid point should be selected at that location [34]. As a result, the structural grids for the splines are chosen as the entire grid selection on the upper skin for each model. The spline verification for the bending and torsion modes can be viewed in Figure 5.8 and Figure 5.9, which indicate a successful spline generation.

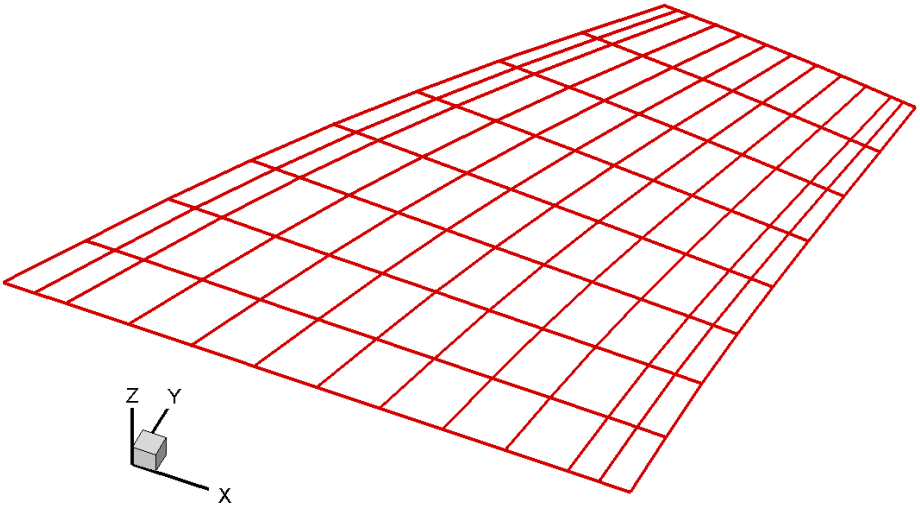

Figure 5.8 Bending Mode Plotted on the Aerodynamic Model

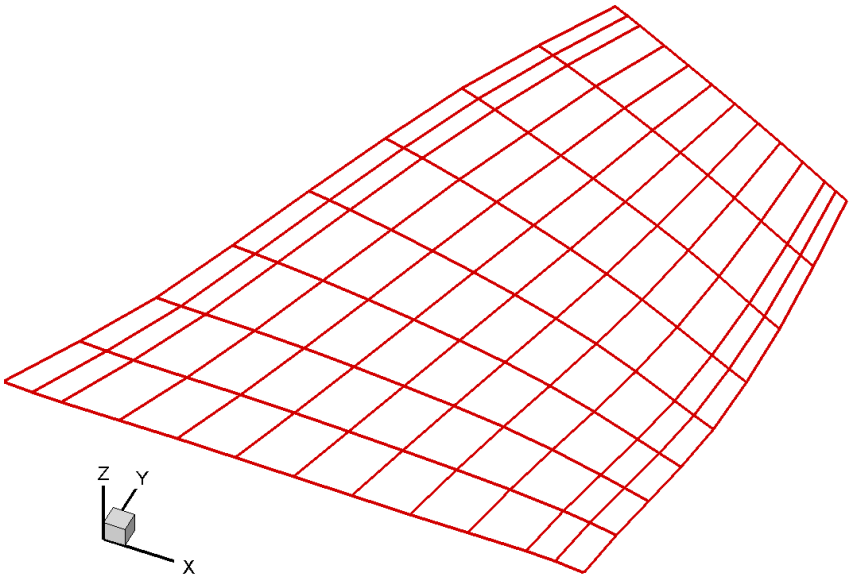

Figure 5.9 Torsion Mode Plotted on the Aerodynamic Model

5.2 Mesh Refinement

In this section, the mesh size effect is investigated for both the structural and aerodynamic models. The baseline wing model is chosen for this study. The models are compared in terms of their computational times and their effects on the modal and flutter results.

5.2.1 Structural Model

As explained in Section 5.1, the meshing strategy for the fighter wing model is a coarse model where elements are divided only at the rib and spar intersections. The support this assumption, a finer model is created as given in Figure 5.10. As a result, the baseline model has 54 CQUAD4 and 10 CTRIA3 elements whereas the finer model has 216 CQUAD4 and 40 CTRIA3 elements. The properties are kept the same therefore, the weight stays the same.

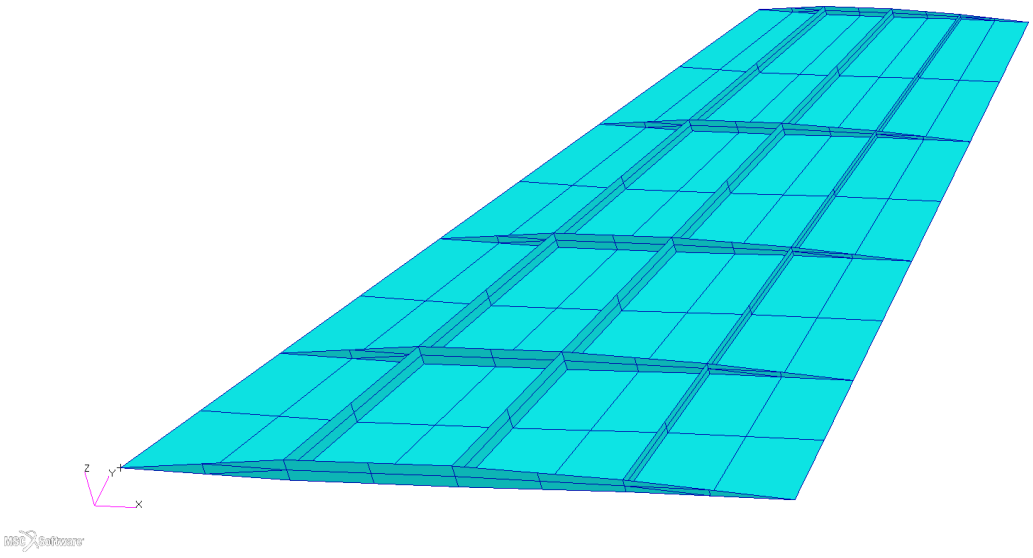

Figure 5.10 A Finer Finite Element Meshing of the Baseline Model

Figure 5.11 shows the first few modes and the torsion mode coupled with local modes detected at a higher frequency. The bending mode is not detected due to local modes. The results show that there are many local modes especially in the skin panels between the spars and ribs. The reason is that since no beam or bar elements are implemented to the FEM to model stiffeners, the quadrilateral elements between the spar and rib intersections are not supported enough to resist this motion. The existence of the local

modes prevents the analysis of pure bending and torsion and thus complicating the flutter analysis. However, a comparison is aimed for this study, therefore; having all the configurations modelled with the same approach is accepted as a valid strategy. Therefore, using a finer model by breaking the quads into four elements given in Figure 5.10 is not chosen due to the unwanted degrees-of-freedom induced by the local modes.

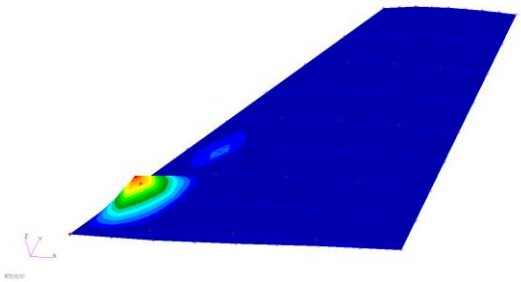

Local Mode [10.75 Hz]

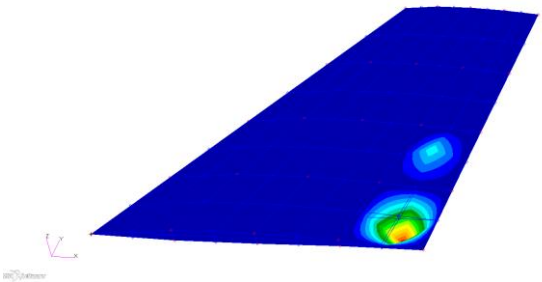

Local Mode [11.08 Hz]

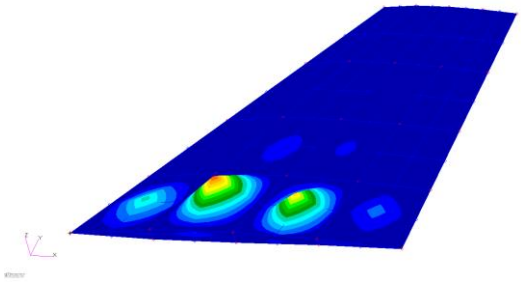

Local Mode [13.45 Hz]

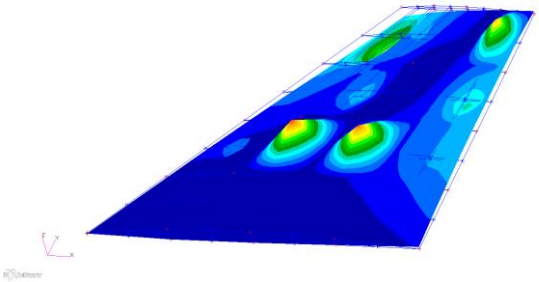

Coupling of Torsion and Local Modes [22.2 Hz]

Figure 5.11 Mode Shapes of the Finer Model

A second approach for a more fine structural mesh size is adopted as given in Figure 5.12. With this model, the local mode issue is eliminated since there is no nodes that are not supported by spar or rib elements.

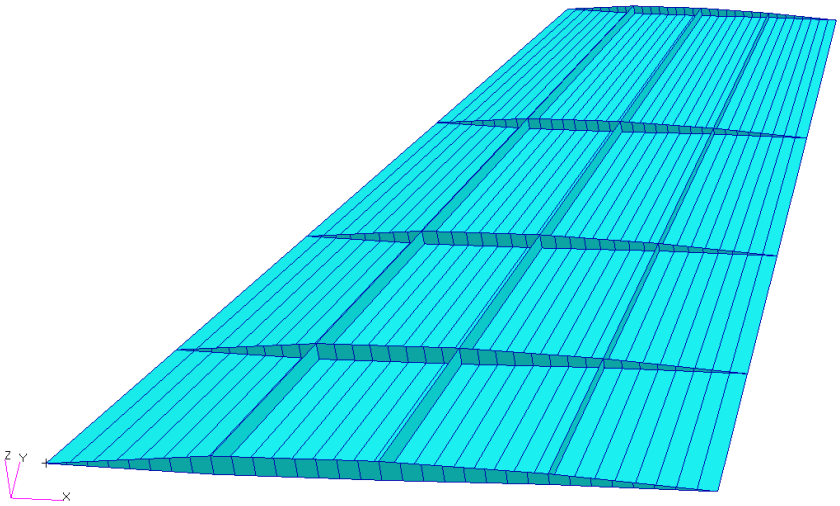

Figure 5.12 Second Approach to a Fine Structural Mesh Size

The results given in Table 5.3 show that increasing the element number by almost 1000% does not have a significant effect on the final flutter speed.

Table 5.3 Comparison of the Baseline and Fine Structural Models

Model	**Element Number**	**Flutter Speed**
Coarse	40	3.0 M
Fine	428	3.3 M

To further investigate the fine model, the wing with the six spar configuration is modeled with a fine approach as shown in Figure 5.13.

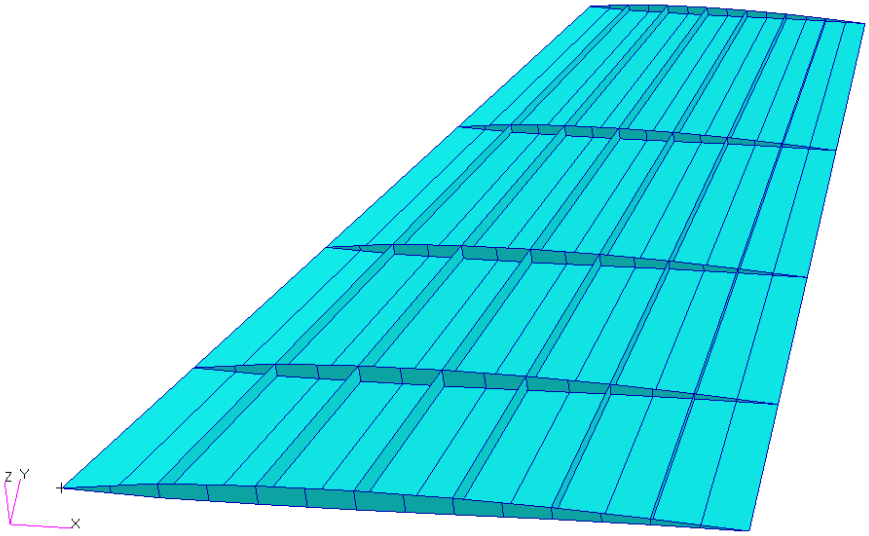

Figure 5.13 Fine Mesh of the Six Spar Configuration

The results given in Table 5.4 show that increasing the element number does not affect the flutter speed of the model showing that the current approach to the mesh size is sufficient in accurately calculating the flutter speeds of the configurations.

Table 5.4 Comparison of the Coarse and Fine Structural Models for the Six Spar Conf.

Model	**Element Number**	**Flutter Speed**
Coarse	115	6.6 M
Fine	206	6.5 M

5.2.2 Aerodynamic Model

The aerodynamic model introduced in Section 5.1 is modified to a finer and coarser model while keeping the spline and structural models the same. The models can be seen in Figure 5.14.

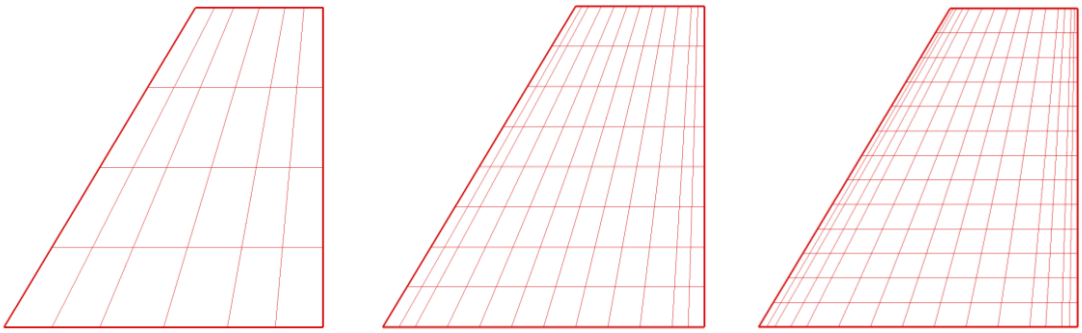

Coarse Aero Model Baseline Aero Model Fine Aero Model

Figure 5.14 Aerodynamic Model Mesh Refinement

The effect of mesh refinement on the total computation time and on the flutter speed is given in Table 5.5. The coarsest mesh calculates the flutter speed fastest however; the flutter speed is estimated to be significantly higher than the other two models. Therefore, a model with this type of mesh is eliminated. When the fine and baseline model are compared, it can be observed that the flutter speeds are very close to each other however, the fine model conducts the flutter analysis in a longer time. Even though for this analysis the time difference may not seem significant, considering that many variations of the structural baseline model will be analyzed, computation times will accumulate unnecessarily while the flutter speed is not varied significantly as seen in Table 5.3. As a result, the baseline model is used throughout the study for the supersonic flutter analysis of various fighter wing configurations.

Table 5.5 Effects of the Aero Mesh Refinements on Parameters

	Coarse Model	**Baseline Model**	**Fine Model**
Total Element #	24	96	195
Flutter Speed	3.20 M	2.96 M	2.91 M
Computation Time [min]	86	111	178

To further support this claim, flutter analyses with finer aerodynamic meshes are conducted to see that the flutter speeds lay within the 2.90-2.96 Mach range and a lower flutter point is not missed. Figure 5.15 shows that when the element mesh size is increased up to 475 elements, there is no significant decrease in the flutter speed. Therefore, the mesh size of 96 elements is concluded to be enough for the scope of this study.

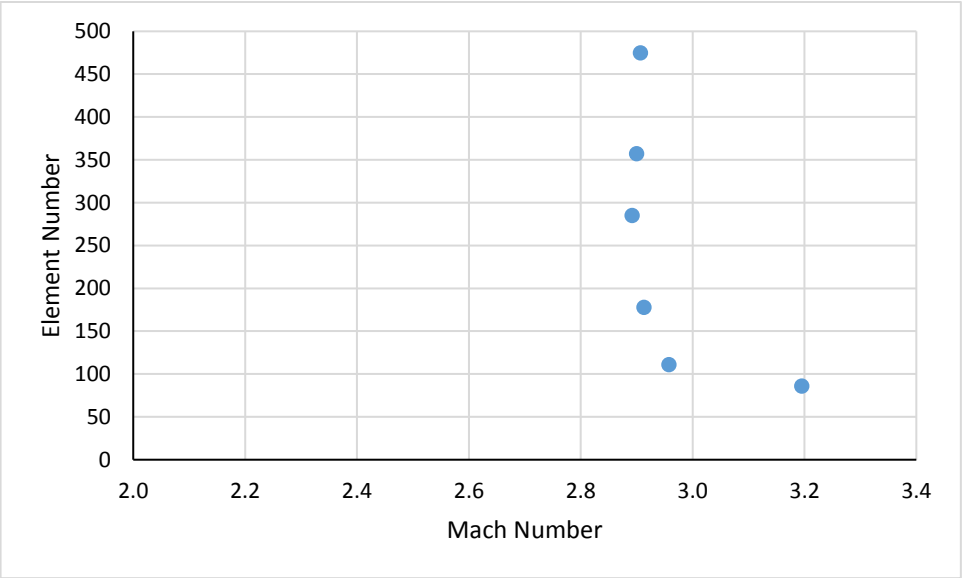

Figure 5.15 Effect of Element Number on the Flutter Speed

5.3 Effect of the Various Aspects of the Fighter Wing on the Flutter Boundary

The features that are studied within the scope of this study are the spar number, spar orientation, skin material in terms of composite and aluminum and finally the effect of an external mass representing a missile or a pod on the supersonic flutter speed. The outer geometry and the location of the ribs and their number is not varied throughout the study. The boundary conditions are given zero translation in all directions and zero rotation about x-axis at the spar attachment grids. The materials and the properties of the elements are as listed in Table 5.1 and Table 5.2 and are not changed between the configurations. The aerodynamic model is constant while the spline grids are chosen from the upper skin nodes for every configuration.

The flutter analyses are conducted at sea level conditions and no structural damping is defined. As previously stated, the degrees-of-freedom that are included are the bending and torsion.

5.3.1 Effect of Spar Number on the Supersonic Flutter Characteristics

Initially, the spar number of the baseline configuration is varied. Figure 5.16 shows the three models with increasing spar numbers. This spar orientation is named as the continuous spar configuration.

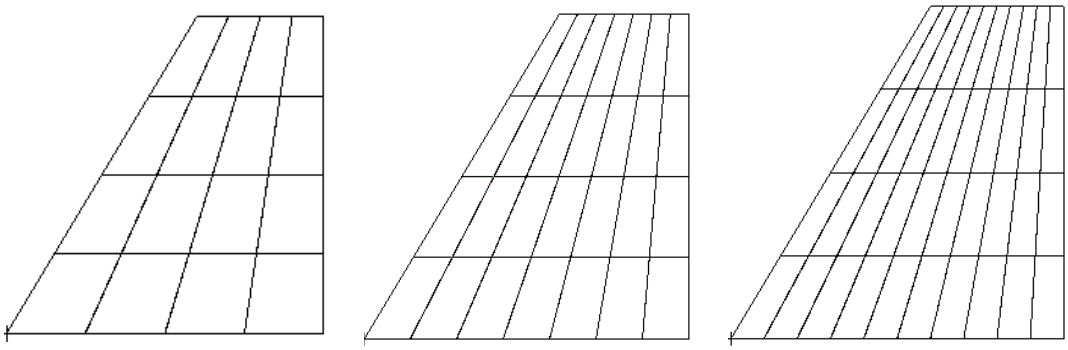

Continuous 3 Spar Continuous 6 Spar Continuous 9 Spar

Figure 5.16 Continuous Spar Number Variations

The natural frequencies and the weights of the configurations are given in Table 5.6. The natural frequencies and the mode shapes are given in Appendix A.

Table 5.6 Natural Frequency and Weight Comparison on the Continuous Spar Configurations

Spar Orientation	**Spar #**	**Bending Frequency [Hz]**	**Torsion Frequency [Hz]**	**Total Weight [kg]**
Continuous	3	7.55	22.53	217.93
Continuous	6	7.81	24.46	233.31
Continuous	9	7.82	24.72	248.52

The comparison of the spar configurations in terms of the natural frequencies shows that the rise observed when the spar number is increased from three to six is not observed between six and nine. This shows that for the continuous spar configuration, the bending and torsional stiffnesses reach a certain level at six spars and a further increase in the spar number does not have an effect on this attribute.

The flutter boundary plots are given in Figure 5.17 - Figure 5.20.

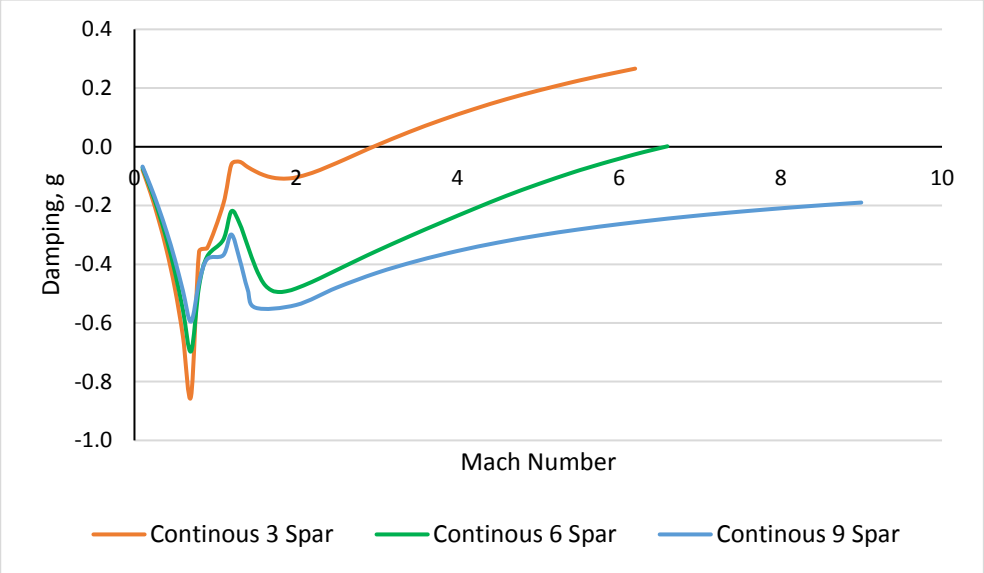

Figure 5.17 Damping vs Velocity Graph for the Bending Mode of the Continuous Spar Number Variation

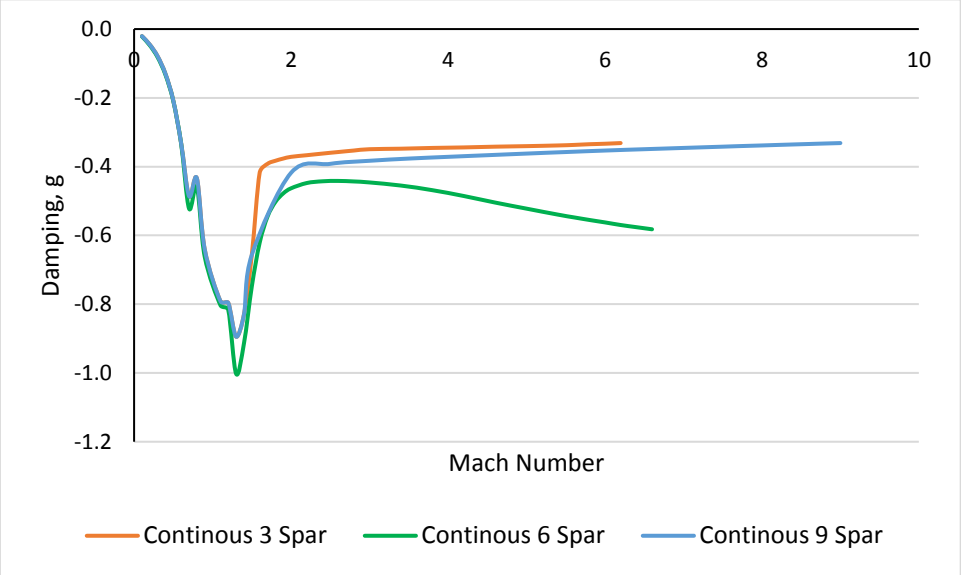

Figure 5.18 Damping vs Velocity Graph for the Torsion Mode of the Continuous Spar Number Variation

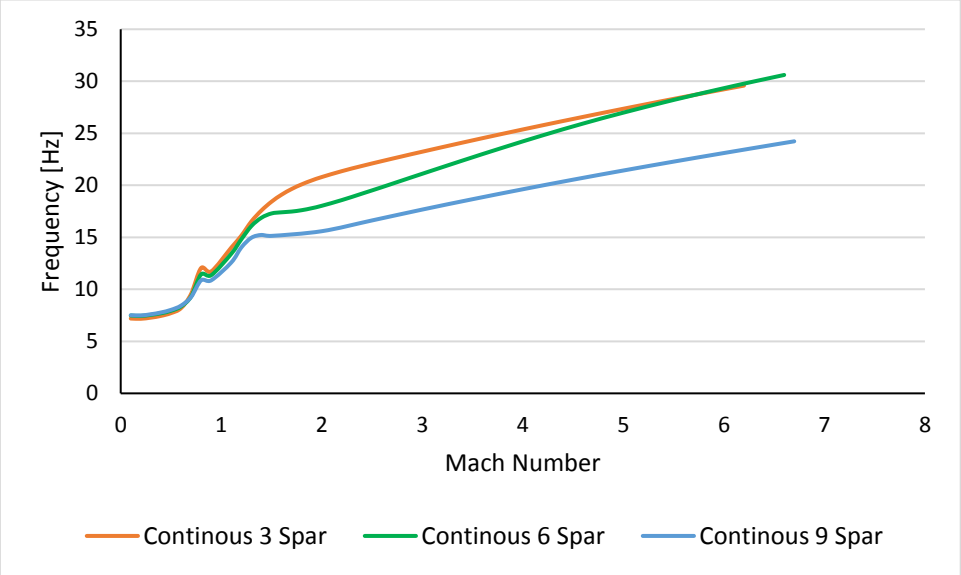

Figure 5.19 Frequency vs Velocity Graph for the Bending Mode of the Continuous Spar Number Variation

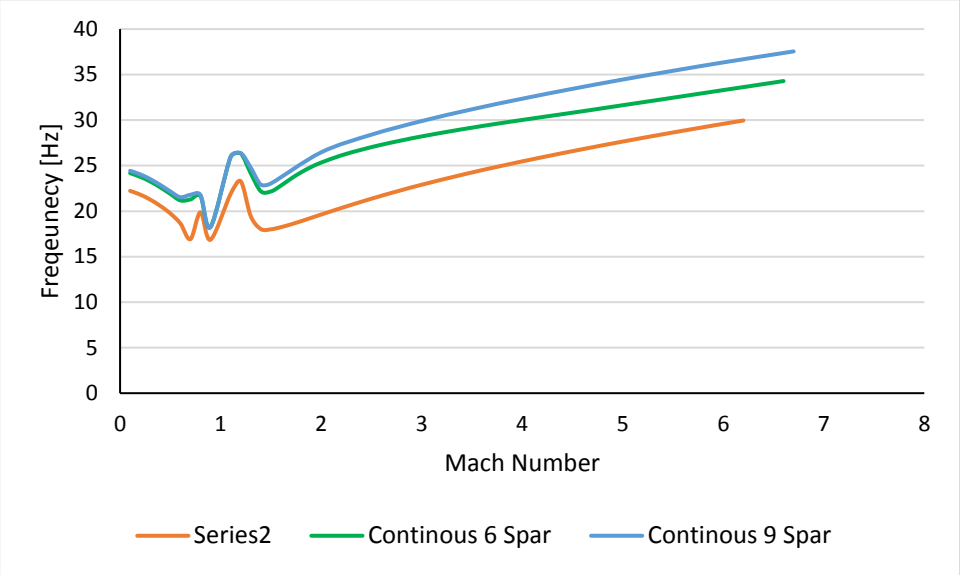

Figure 5.20 Frequency vs Velocity Graph for the Torsion Mode of the Continuous Spar Number Variation

It is important to note that ZAERO has the capability to solve the subsonic and supersonic flutter problems at a single run by automatically switching the solvers with respect to the Mach number that is defined in the run file. The flutter frequencies as well as the interpolated flutter speeds of the three models are given in Table 5.7. No flutter point is detected for the nine-spar configuration up to Mach number of 9. For the three and six spar configurations, flutter occurs at the bending mode.

Table 5.7 Spar Number Effect on the Continuous Spar Configuration Flutter Boundary

Spar Orientation	**Spar #**	**Flutter Frequency [Hz]**	**Flutter Speed [M]**
Continuous	3	23.14	2.96
Continuous	6	30.55	6.57
Continuous	9	-	+ 9.00

From Table 5.6, it is seen that for the six and nine spar configurations the difference between the bending and torsional natural frequencies is higher compared to the three spar configuration. In the classical flutter event, it is known that flutter occurs when the bending and the torsional frequencies approach each other, which is illustrated in a generic flutter boundary plot given in Figure 5.21. It can be seen that flutter occurs at the speed where the bending and torsion modes get close to each other. Therefore, if the natural frequencies, which are the frequencies at zero velocity, become apart from each other, the flutter point can be expected to occur at a higher speed. Although a strict generalization can not be made, one of the reasons for the higher flutter speed of the six or nine spar configurations compared to the three spar configuration could be due to the higher difference between the bending and torsional frequencies compared to the three spar configuration. Moreover, the natural frequencies of the six and the nine spar configurations are very close to each other implying that the bending and the torsional stiffness of the nine spar configuration are higher than the corresponding terms of the six spar configuration, because nine spar configuration has a higher mass which would normally account for higher bending and torsional stiffness. Hence, higher wing stiffness of the nine spar configuration results in higher flutter speed compared to the six spar configuration.

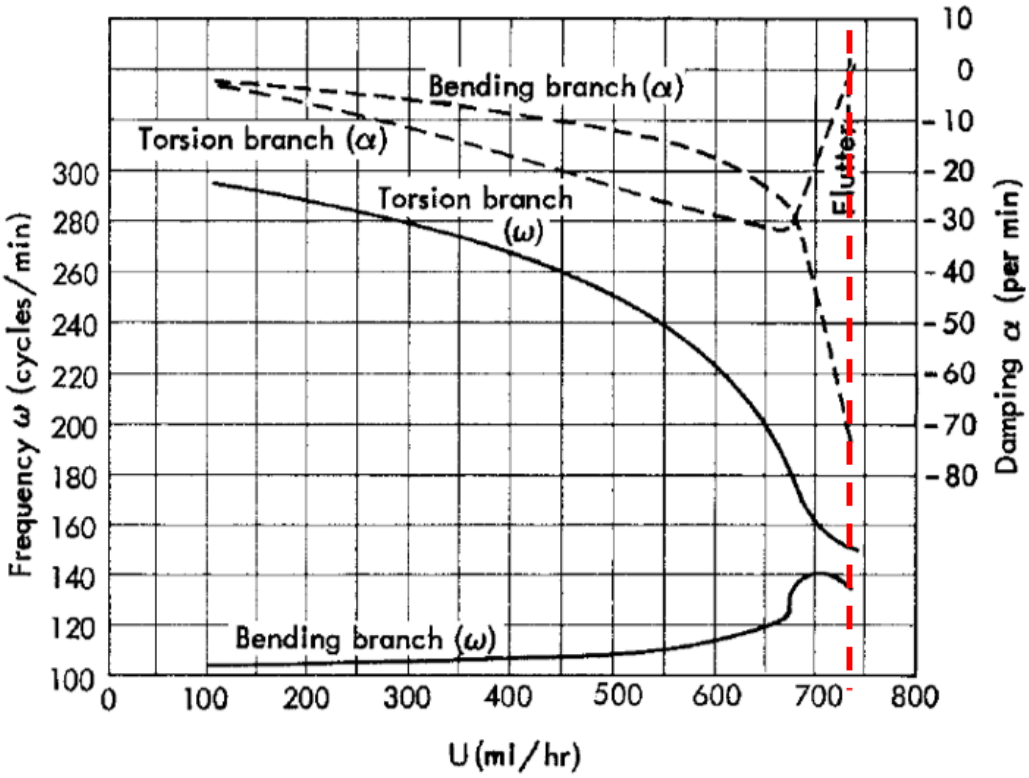

Figure 5.21 Generic Flutter Boundary Plots [1]

The study for the effect of spar number is further expanded. The spar thicknesses are decreased, while the other attributes are kept constant, so that all the configurations have the same total weight. Table 5.8 gives the weight and natural frequencies of the spar configurations with the same weight.

Table 5.8 Natural Frequencies of the Various Spar Number with Constant Total Weight Configurations

Spar Orientation	**Spar #**	**Spar Thickness [mm]**	**Total Weight [kg]**	**Bending Frequency [Hz]**	**Torsion Frequency [Hz]**
Continuous	3	3.5	217.93	7.55	22.53
Continuous	6	1.8	217.44	7.92	24.72
Continuous	9	1.2	217.56	8.05	25.38

The flutter boundary plots are not included as the boundaries are not affected significantly and the trends observed in Figure 5.17 - Figure 5.20 still hold true. The flutter frequencies as well as the interpolated flutter speeds of the three models are given in Table 5.9. No flutter point is detected for the nine-spar configuration up to Mach number of 9. For the three and six spar configurations, flutter occurs at the bending mode.

Table 5.9 Spar Number with Constant Total Weight Effect on the Continuous Spar Configuration Flutter Boundary

Spar Orientation	**Spar #**	**Flutter Frequency [Hz]**	**Flutter Speed [M]**
Continuous	3	23.14	2.96
Continuous	6	29.68	5.47
Continuous	9	-	+ 9.00

The results show that, although the weights are the same, continuous 9 spar configuration still has the highest flutter speed. This points to the fact that the high flutter speed at 9 spar configuration is not attributed to its high weight but rather to the increase of stiffness caused by the increase in the spar numbers. The remark that as the bending and torsion natural frequencies become apart from each other the flutter speed increases hold true for these results as well.

5.3.2 Effect of Spar Orientation on the Supersonic Flutter Characteristics

The second aspect of the structural layout that is investigated is the effect of the spar orientation on the flutter boundary. Research is carried out to determine the types of spar orientations that are used for fighter wing layouts. In the end, the following five types of orientations are used for the study;

1. Continuous Spar Configuration
2. Leading Edge Parallel Spar Configuration
3. Y-Axis Parallel Spar Configuration

4. Two Section Spar Configuration

The models are given in Figure 5.22. In order to be able to compare the configurations, for all models at the root sections there given six spars. The thicknesses of the skin, spar and rib elements are not changed between the configurations.

The natural frequencies and the weights of the configurations are given in Table 5.10. The natural frequencies and the mode shapes are given in Appendix A.

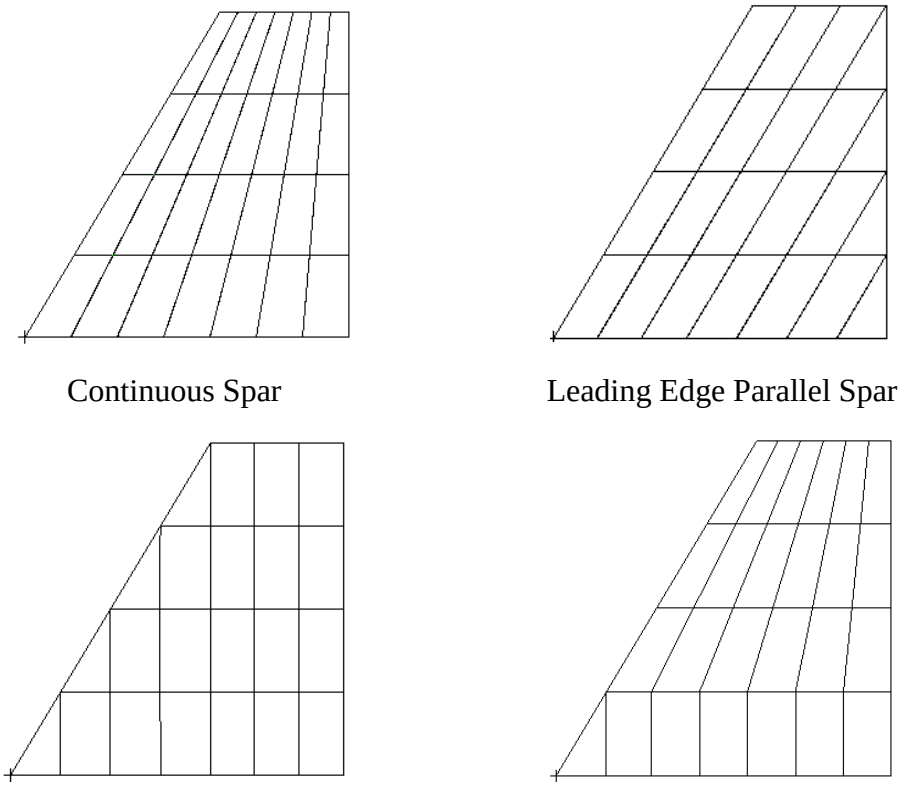

Figure 5.22 Spar Orientation Configurations

Table 5.10 Natural Frequency and Weight Comparison on the Spar Orientation Configurations

Spar Orientation	**Spar #**	**Bending Frequency [Hz]**	**Torsion Frequency [Hz]**	**Total Weight [kg]**
Continuous	6	7.82	24.46	233.31
LE Parallel	6	8.26	24.27	232.85
Y-Axis Parallel	6	8.04	24.35	223.07
Two Sections	6	7.68	24.29	228.18

In terms of the bending natural frequencies, although in overall the values do not differ considerably, the LE parallel configuration shows the highest stiffness followed by the y-axis parallel. The reason why these configurations perform better compared to the others is that their spars are positioned parallel to each other. The combination of the spars increases the resistance in the bending axis. In terms of the torsional natural frequencies, the difference is very little and hence negligible. Comparing the models in terms of their weight show that the continuous and the LE parallel models have the same mass while the y-axis parallel and the two sections configurations are approximately 10 kg lighter.

The flutter boundary plots are given in Figure 5.23 - Figure 5.26.

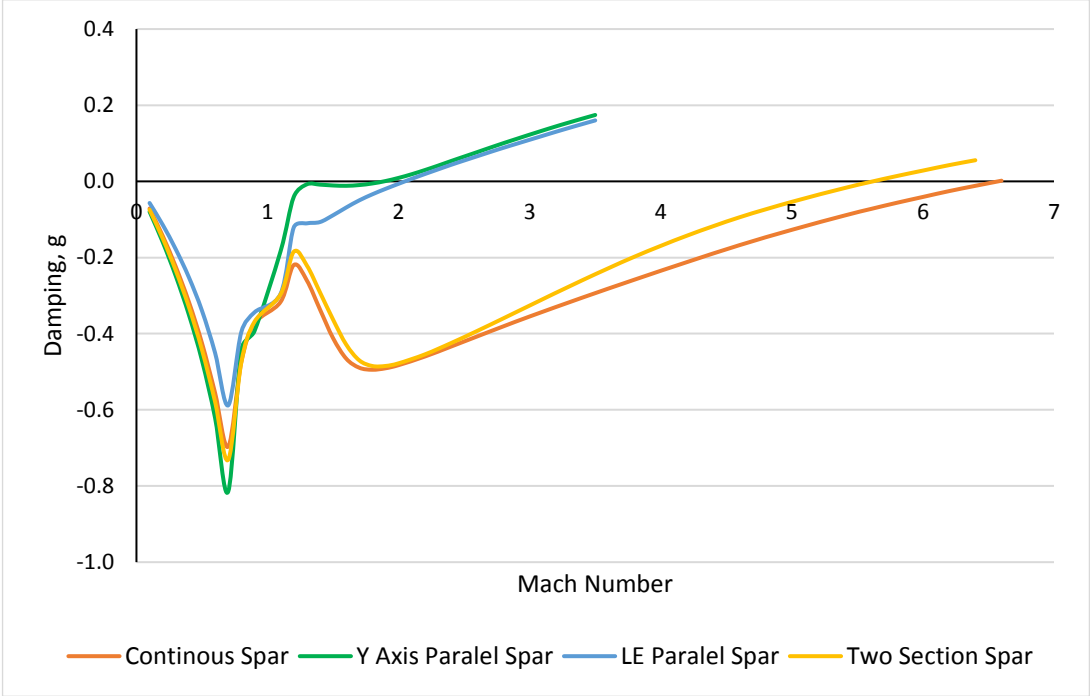

Figure 5.23 Damping vs Velocity Graph for the Bending Mode of the Spar Orientations

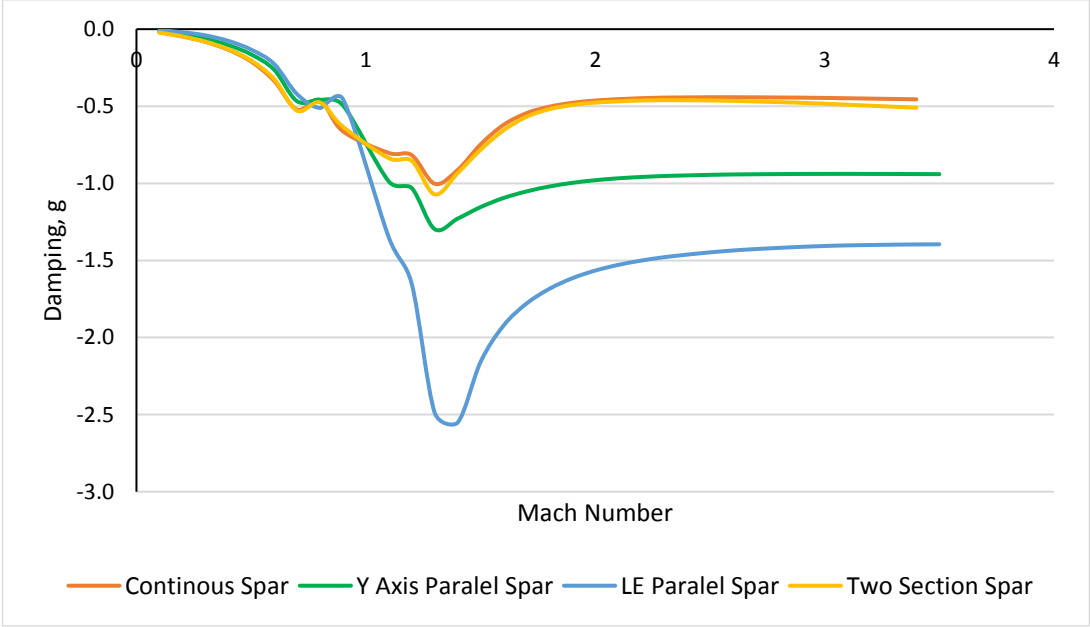

Figure 5.24 Damping vs Velocity Graph for the Torsion Mode of the Spar Orientations

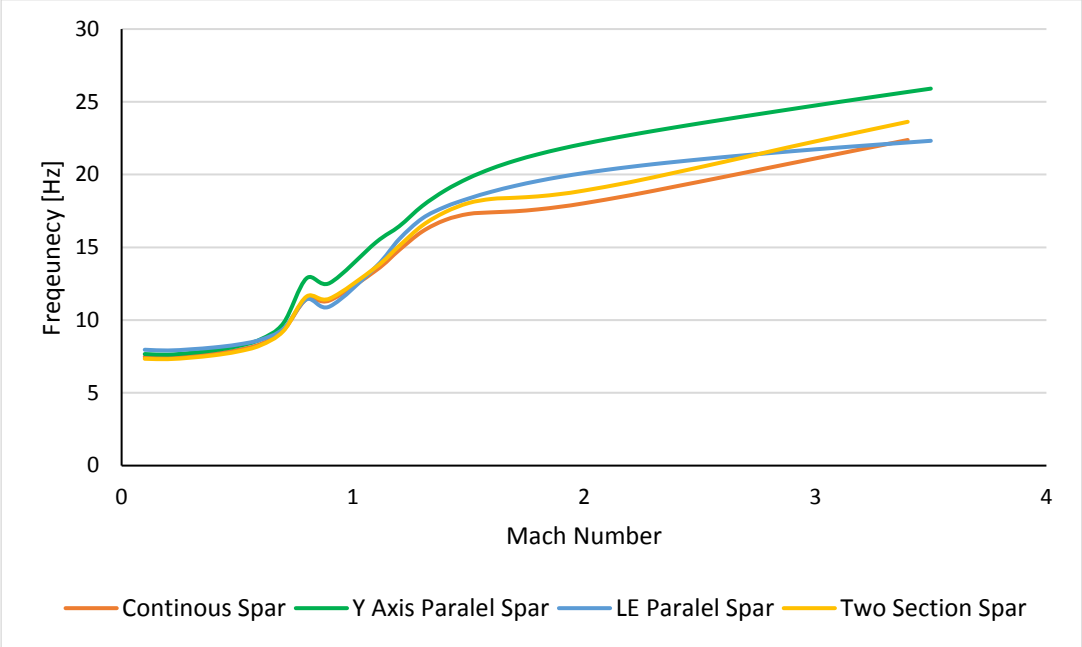

Figure 5.25 Frequency vs Velocity Graph for the Bending Mode of the Spar Orientations

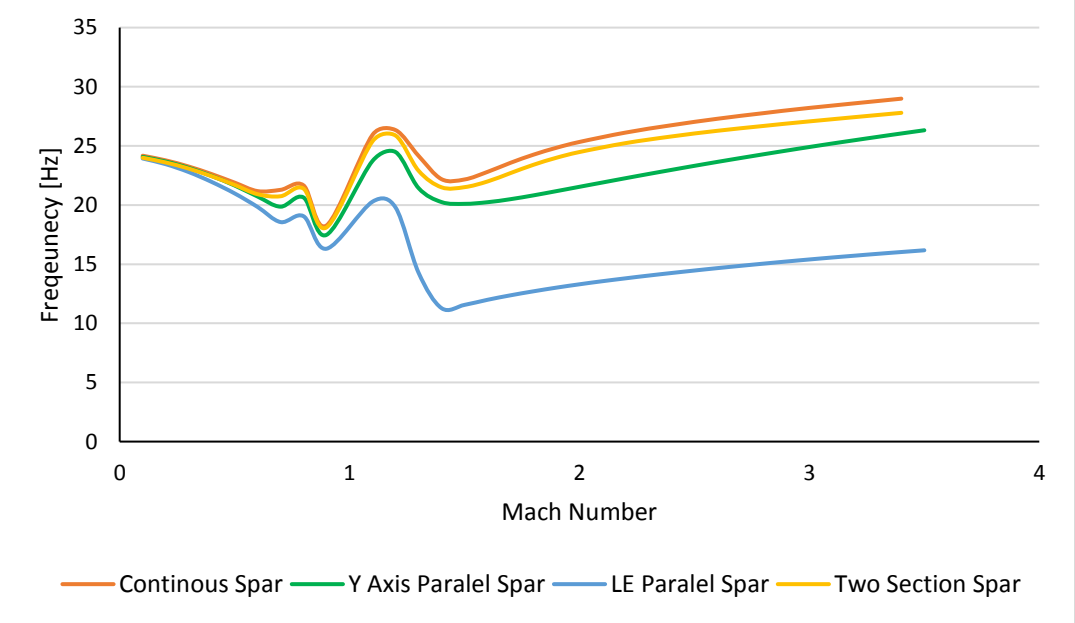

Figure 5.26 Frequency vs Velocity Graph for the Torsion Mode of the Six Spars

The flutter frequencies as well as the interpolated flutter speeds of the models are given in Table 5.11. For all the six spar configurations, flutter occurs at the bending mode.

Table 5.11 Spar Orientation Effect on the Six Spar Configuration Flutter Boundary

Spar Orientation	**Spar #**	**Flutter Frequency [Hz]**	**Flutter Speed [M]**
Continuous	6	30.55	6.57
LE Parallel	6	20.21	2.05
Y-Axis Parallel	6	21.72	1.89
Two Sections	6	29.26	5.62

According to Table 5.11, the highest flutter speed is observed for the continuous spar orientation followed by the two sections configuration. The most significant distinction of these two models is the number of spars at the tip sections with continuous having six and two-section having five. Since the continuous and the two section configurations have more number of spars at the tip sections compared to the other two configurations, bending and torsional stiffnesses of the outboard sections of the these configurations are the highest. It is known that the torsional stiffness is a dominant factor affecting the flutter speed. Moreover, continuous and two section wing configurations have higher differences between the bending and the torsional frequencies compared to the leading edge parallel and y-axis parallel configurations. Therefore, the flutter speeds of the continuous and two section configurations are higher than the leading edge parallel and y-axis parallel configurations.

It is also noticed that the main difference between the leading edge and y-axis parallel configurations is the spar length. Leading edge parallel configuration has longer spars compared to the y-axis parallel configuration; hence, the leading edge parallel wing is heavier than the y-axis parallel wing. Since the torsional frequencies of both wings are very close to each other, torsional stiffness of the leading edge parallel configuration must be higher than the torsional stiffness of the y-axis parallel wing configuration.

Higher torsional stiffness of the leading edge parallel configuration accounts for higher flutter speed as seen in Table 5.11.

5.3.3 Effect of Composite Skins on the Supersonic Flutter Characteristics

The third aspect whose influence is investigated on the supersonic flutter speed is the composite modelling of the fighter wing skin. The skin material of the baseline model, which has 3 spars as seen in Figure 5.3, is changed from aluminum to carbon fiber reinforced plastic (CFRP) composite while keeping the rest of the modelling approach the same. Reference [41] shows a study regarding the unidirectional ply orientation with respect to the leading edge of a wing, stating that when the plies are stacked from 0° to 45°, due to the reduction in the effective angle of attack, the aerodynamic loads will be the smallest around the 15° and 25° ply orientation. In this chapter, this approach is utilized to investigate if the same effect will be observed for the flutter speed as well. Furthermore, by modifying the first and final plies of the QI orientation, a modified quasi-isotropic orientation is created and the final flutter speeds are compared.

In the wing skin, eight plies are used with a ply thickness of 0.25 mm leading to a total skin thickness of 2 mm. This value is deliberately chosen to be comparable to the aluminum skin thickness which is 2 mm as well. For the wing skin layup, quasi-isotropic ply orientation [0° 45° -45° 90° 90° -45° 45° 0°] is adapted. Both woven and unidirectional (UD) orthotropic materials are used for the analysis whose mechanical properties are given in Table 5.12. Figure 5.27 shows the reference fiber angle with respect to skin geometry.

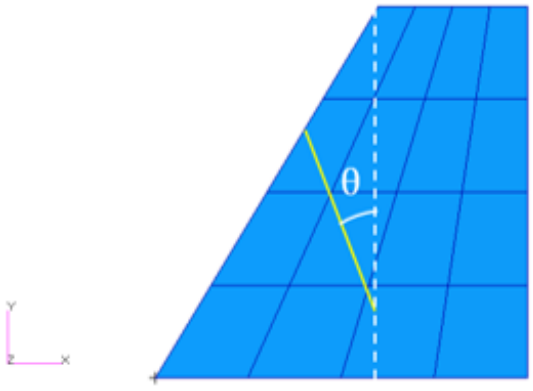

Figure 5.27 Definition of the Fiber Orientation Angle

Table 5.12 Mechanical Properties of the Standard CFRP Composite [42]

Properties	**Fabric**	**UD**
Modulus in the fiber direction, E_1	70 000 MPa	135 000 MPa
Modulus transverse to fiber direction, E_2	70 000 MPa	10 000 MPa
In-Plane Shear Modulus, G_{12}	5 000 MPa	5 000 MPa
Poisson's Ratio, ν	0.1	0.3
Density, ρ	1600 kg/m^3	1.600 kg/m^3

Initially, the UD ply orientation is modified such that all of the eight plies varies from 0° to 45° to detect where the flutter speed becomes the highest. Figure 5.28 shows the damping vs velocity plot for the mode where flutter occurs.

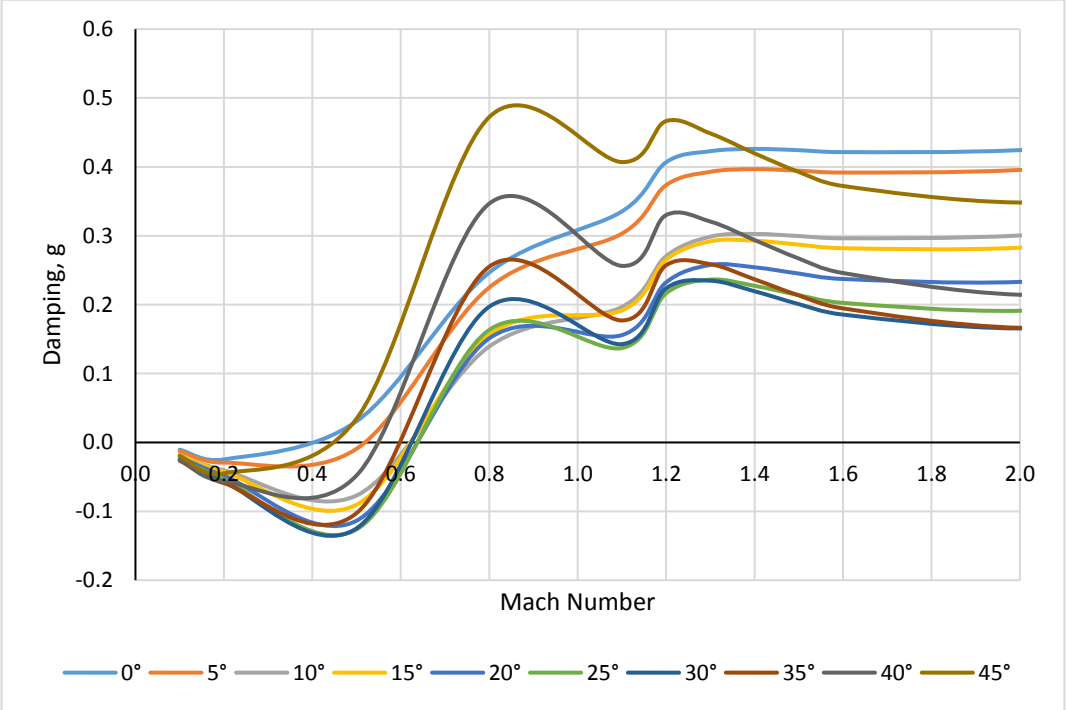

Figure 5.28 Damping vs Velocity for the Bending Mode of the UD Ply Orientations [0°- 45°]

Table 5.13 shows the natural frequencies as well as the flutter frequency and the interpolated flutter speeds. Flutter is observed at the bending mode for all configurations. It is important to note that this part is preparatory work for further analysis therefore the fact that the flutter does not occur at supersonic speeds is not significant. The natural frequencies and the mode shapes are given in Appendix A.

Table 5.13 Interpolates Flutter Speeds for UD Ply Orientations [0°- 45°]

Ply Orientation of UD Layer	**Bending Frequency [Hz]**	**Torsion Frequency [Hz]**	**Flutter Speed [M]**	**Flutter Frequency [Hz]**
0°	8.23	21.00	0.333	18.56
5°	7.31	21.58	0.512	17.32
10°	6.54	21.86	0.607	17.19
15°	5.93	21.83	0.610	16.97
20°	5.44	21.53	0.629	16.47
25°	**5.06**	**20.99**	**0.631**	**15.89**
30°	4.77	20.27	0.616	15.27
35°	4.54	19.41	0.586	14.58
40°	4.37	18.48	0.536	13.78
45°	4.24	17.58	0.369	14.45

Table 5.13 shows that at 25°, the flutter speed becomes highest and further increase in the fiber orientation does not increase the flutter speed any further. It is important to note that for this fiber orientation, the wing has neither the highest bending nor the torsion natural frequency. However, it is noticed that for this orientation the difference the bending and torsional natural frequencies is one of the highest. It should be noted

that the difference between the bending and the torsional natural frequencies is not the sole factor that governs the flutter speed. However, if the difference between the bending and the torsional natural frequencies is high, then the flutter speed is also high and maximizing the difference between the bending and the torsional frequencies is a design practice recommended to increase the flutter speed.

The next step is to replace the first and last plies of the quasi-isotropic layup (0^o plies) by 25° plies and observe the effects on the flutter boundary. Table 5.14 shows the ply orientations and the weight effects. It should be noted that for the woven fabric material each ply is assumed to be composed of mutually perpendicular fibers but the total thickness of the ply of the woven fabric is same as the ply thickness of UD plies.

Table 5.14 Comparison of the Aluminum and Composite Skin Wing Models

Wing Skin Material	**Thickness [mm]**	**Ply Orientation [degree]**	**Total Weight [kg]**
Aluminum	2	-	217.93
Woven Fabric	0.25 x 8 =2	[0° 45° -45° 90° 90° -45° 45° 0°]	134.08
UD	0.25 x 8 =2	[0° 45° -45° 90° 90° -45° 45° 0°]	134.08
Modified UD	0.25 x 8 =2	[25° 45° -45° 90° 90° -45° 45° 25°]	134.08

The damping and frequency versus velocity plots for the aluminum, quasi-isotropic woven and unidirectional and the modified unidirectional models are given in Figure 5.29 - Figure 5.32.

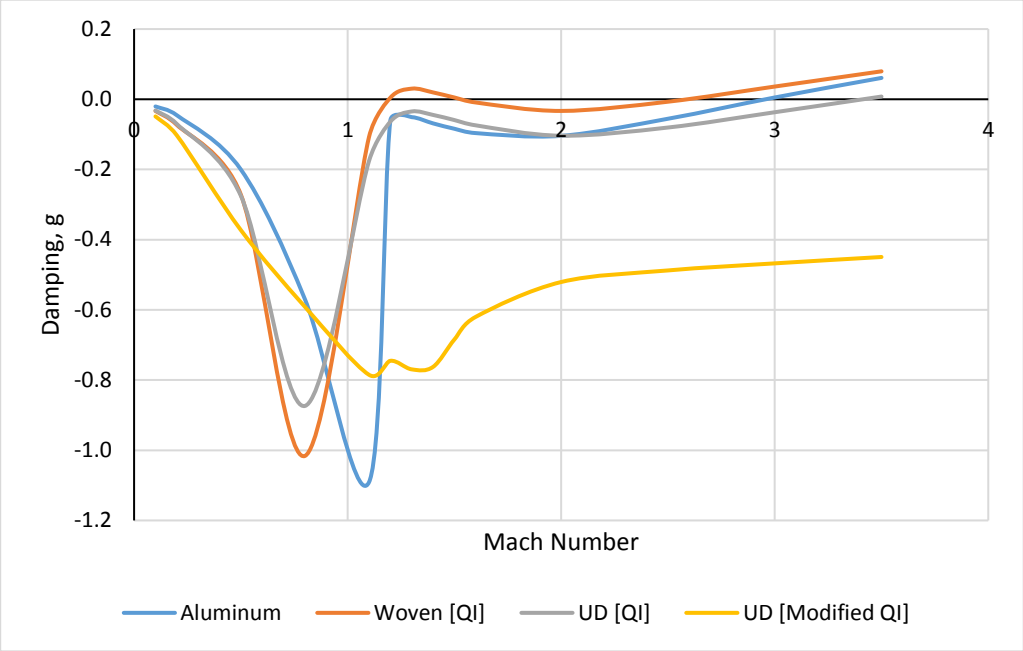

Figure 5.29 Damping vs Velocity Graph for the Bending Mode of the Ply Orientations

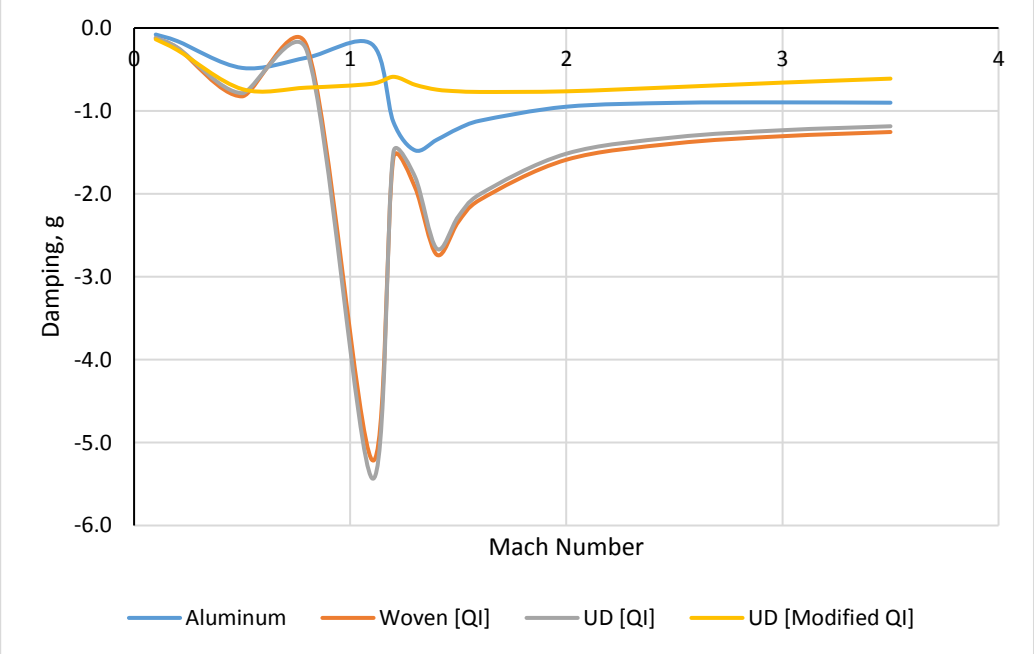

Figure 5.30 Damping vs Velocity Graph for the Torsion Mode of the Ply Orientations

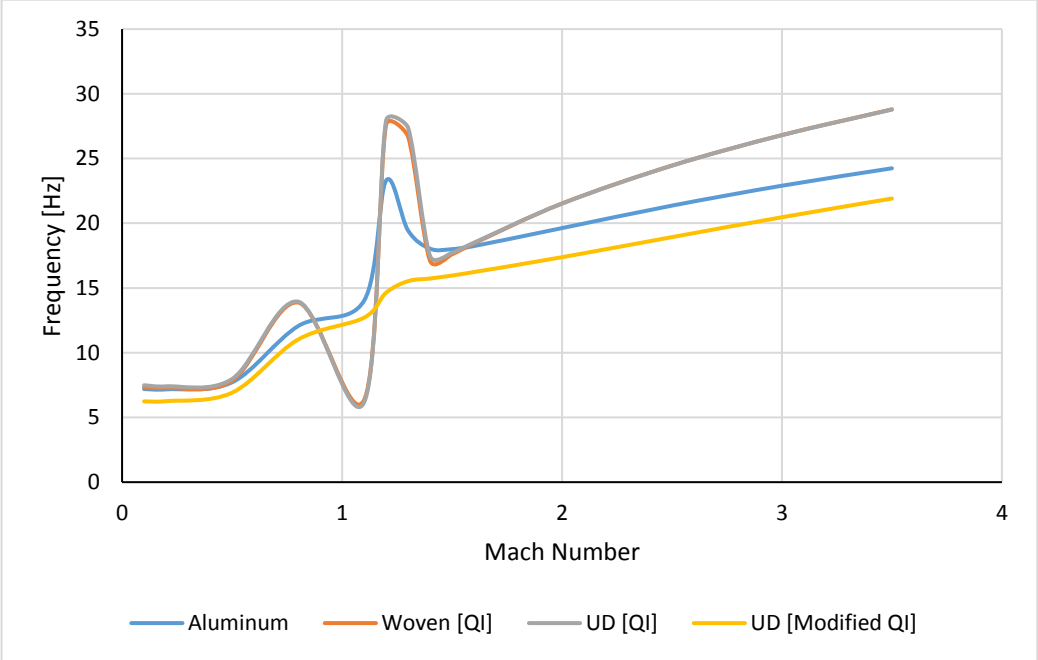

Figure 5.31 Frequency vs Velocity Graph for the Bending Mode of the Ply Orientations

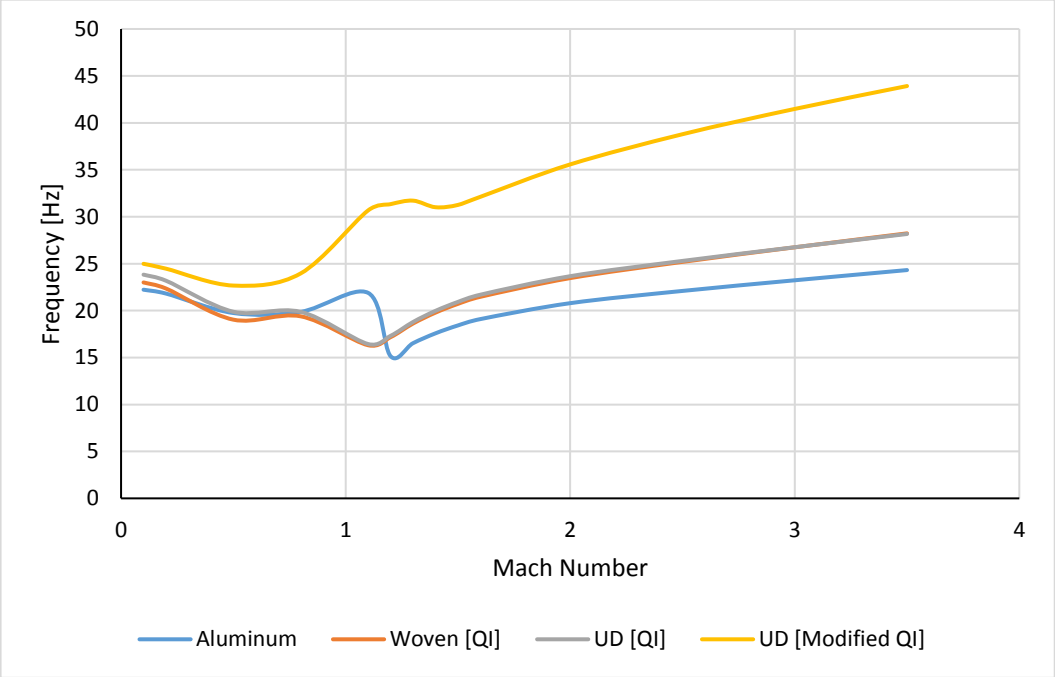

Figure 5.32 Frequency vs Velocity Graph for the Torsion Mode of the Ply Orientations

The natural frequencies and the interpolated flutter speeds for the wing configuration with different wing skin materials considered are given in Table 5.15. For the modified UD ply orientation, no flutter is observed up to a Mach number of 9. For the other configurations, flutter occurs at the bending mode.

Table 5.15 Comparison of the Aluminum and Composite Wing Models

Material	**Bending Frequency [Hz]**	**Torsion Frequency [Hz]**	**Flutter Speed [M]**	**Flutter Frequency [Hz]**
Aluminum	7.55	22.53	2.96	23.14
Woven [QI]	7.94	23.48	2.58	25.44
UD [QI]	8.08	24.31	3.41	27.92
Modified UD	6.77	25.48	+ 9.00	-

The results show that changing the skin property from aluminum to carbon epoxy composite significantly decreases the total weight of the wing while keeping the skin thickness the same. It should also be noted that except for the bending natural frequency of the modified UD quasi isotropic wing configuration, bending and torsional natural frequencies of the wings with composite skins are higher than the wing with aluminum skin. Wing with woven fabric skin has the lowest flutter speed. This could be due to the low Young's modulus of the woven fabric in one of the in-plane directions. It is noticed that all the composite wing configurations have the same weight, therefore the differences in the flutter speeds between the wings with composite configurations are mainly due to the different stiffness properties of the composite wings and not due to the inertial effects. Comparing the quasi-isotropic orientations, it is seen that the wing with unidirectional plies has a higher flutter speed compared to all aluminum wing and the wing with woven skins. This results from the fact that the unidirectional plies have high stiffness in the fiber direction and the outermost plies, which are most effective especially on the bending stiffness of the wing, are aligned along the y axis of the wing as shown in Figure 5.27. In a sense, this ply orientation adds additional stiffness, similar to the spars, to support the wing against twisting and bending forces. Finally, the highest flutter speed is observed for the wing configuration with modified unidirectional ply orientation in which 0° plies are made 25°. Such a modification results in increased torsional stiffness and reduced

bending stiffness, which is evident from the natural frequency results given in Table 5.15. Again, for the wing with the quasi-isotropic layup having modified UD plies, the difference between the bending and the torsional natural frequencies is maximum. However, when composite plies are placed in an off-axis fashion with respect to the wing axis, bending and torsional deformations are also coupled and such a coupling, named as bending-torsion coupling, has a lowering effect on the flutter speed since it promotes bending and torsion coupling. On the other hand, when the 0^o plies are rotated towards the leading edge, due to the bending torsion coupling effective angle of attack of the wing sections reduce causing reduction in aerodynamic loads, which has an increasing effect on the flutter speed. As mentioned before, torsional stiffness of the wing increases due to the off-axis plies and when the 0^o plies are rotated towards the leading edge torsional stiffness of the wing increases, which has an increasing effect on the flutter speed. Hence, flutter speed is governed by the complex interaction of the aforementioned effects and it turns out that the highest flutter speed occurs when the 0^o plies of the quasi-isotropic skin layup are rotated towards the leading edge by an angle which is taken as 25^o based on the previous study on skin laminate with pure UD plies. Current study shows that fighter wings with composite skins may be advantageous in terms of having higher flutter speeds and lower mass compared to all aluminum wings. Moreover, the use of woven composites in the wing skins has no aeroelastic advantage when compared to the all aluminum wing except for lower mass. It should be noted that present study only considers the flutter aspect of wings with composite skins. In the fighter wing design, strength and stability considerations are also considered to decide on the optimum ply angle of the skin layup.

5.3.4 Effect of External Weight on the Supersonic Flutter Characteristics

The final aspect whose influence on the supersonic flutter characteristics of the fighter wing investigated is the effect of an external weight attached to the wing. This weight represents the missiles that the fighter wing is expected to carry. MSC. Nastran provides alternative ways to define mass which are by concentrated masses (CMASSi and CONMi), mass density on the material entries (MAT1, MAT2, etc.), and nonstructural mass defined on the property entries [32]. For the purpose of the study, a concentrated point mass element CONM2 is used to model a 40 kg point mass where the inertia properties are not defined.

The CONM2 element is attached to all grids of the middle rib of the baseline model by a multipoint constraint element. The purpose of these elements is to impose fixed constraints between components of motion at the grid points to which they are connected. Each constraint equation that emerges due to constraint elements, expresses one dependent degree of freedom as a linear function of the independent degrees of freedom [32]. For the purpose of the study, an RBE3 element is used to attach the external mass to the wing. RBE3 defines a constraint relation in which forces and moments applied to reference points are distributed to a set of independent degrees of freedom based on the RBE3 geometry and local weight factors without adding additional stiffness to the structure. MSC. Nastran recommends this element to be used for distributing applied loads and masses in a model [32]. The independent terms of the RBE3 element are given the translational degrees-of-freedom while the dependent term is given all six degrees-of-freedom. The attachment concept can be seen in Figure 5.33.

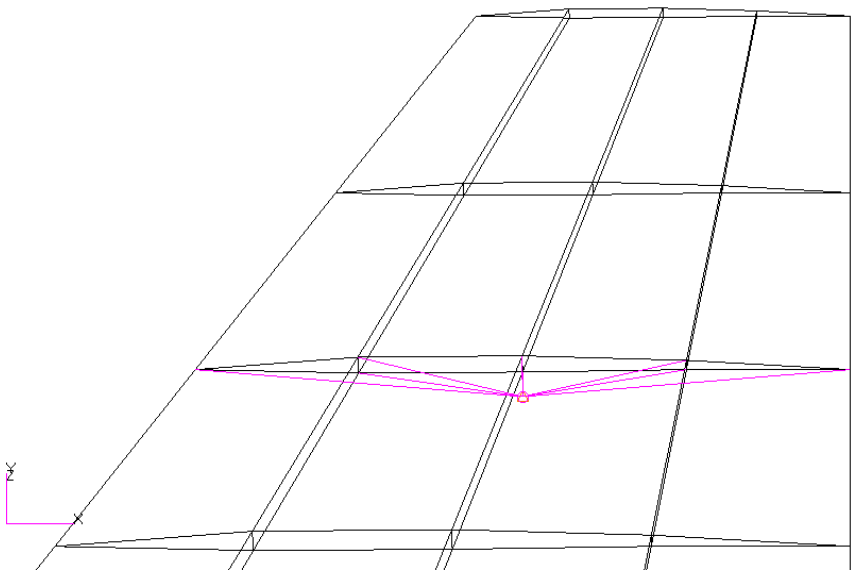

Figure 5.33 Connection of the Weight to the Wing

The effect of the external weight is analyzed by placing the CG of the mass at different locations along the middle rib. Figure 5.34 illustrates the configurations where the red circle represents the CG of the external mass and the purple circle represent the total CG of the wing including the external mass. The flutter results of these configurations are compared with each other and the clean configuration.

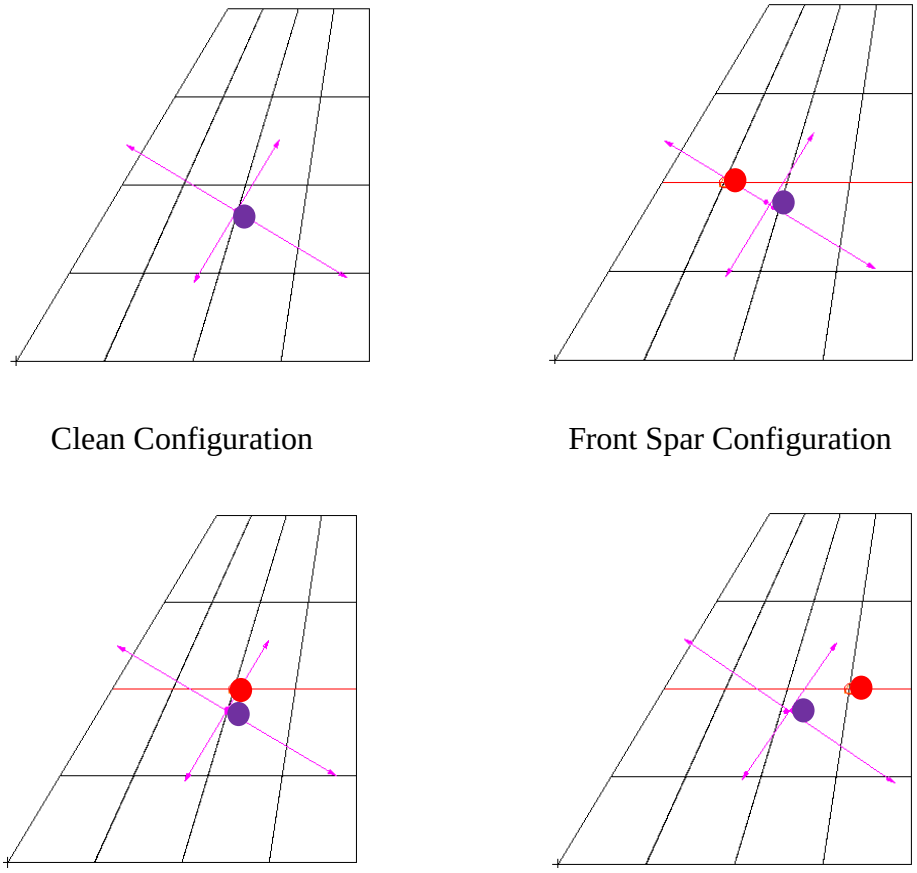

Figure 5.34 The External Weight Positions

In this section, since the mass of the external weight is kept constant for each configuration the flutter speed is mainly affected by the updated center of gravity. The y and z-axes for the different configurations are the same; therefore, the x-axis will be affected. Table 5.16 shows the effect of the external weight positions on the x-axis of center of gravity.

Table 5.16 The X-Axis Center-of-Gravity and the Weight of the Configurations

Configuration	Total Weight [kg]	X-Axis [mm]
Clean	217.93	3121.04
Front Spar	257.93	3005.02
Middle Spar	257.93	3140.83
Rear Spar	257.93	3276.61

The distance between the center-of-gravity and elastic axis of a wing is called the static unbalance. This parameter is positive if the center-of-gravity is aft of the elastic axis and negative when the center-of-gravity is forward of the elastic axis. The flutter speed increases when the static unbalance becomes closer to zero, in other words, the elastic axis and the center-of-gravity gets closer to each other.

The flutter boundary plots for the four configurations considered are given in Figure 5.35 - Figure 5.38.

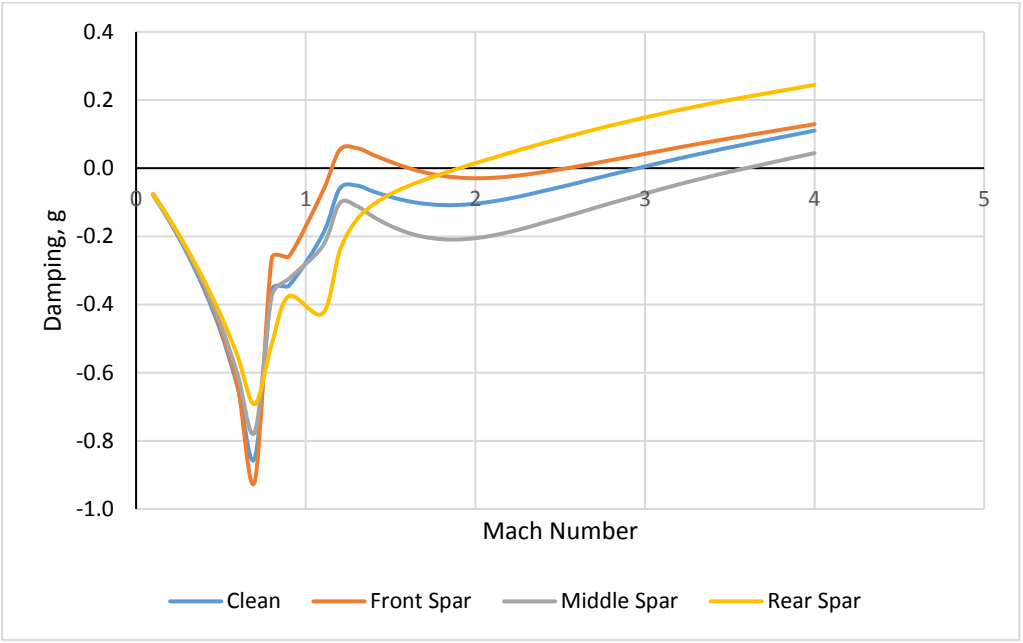

Figure 5.35 Damping vs Velocity Graph for the Bending Mode of the External Weight Configurations

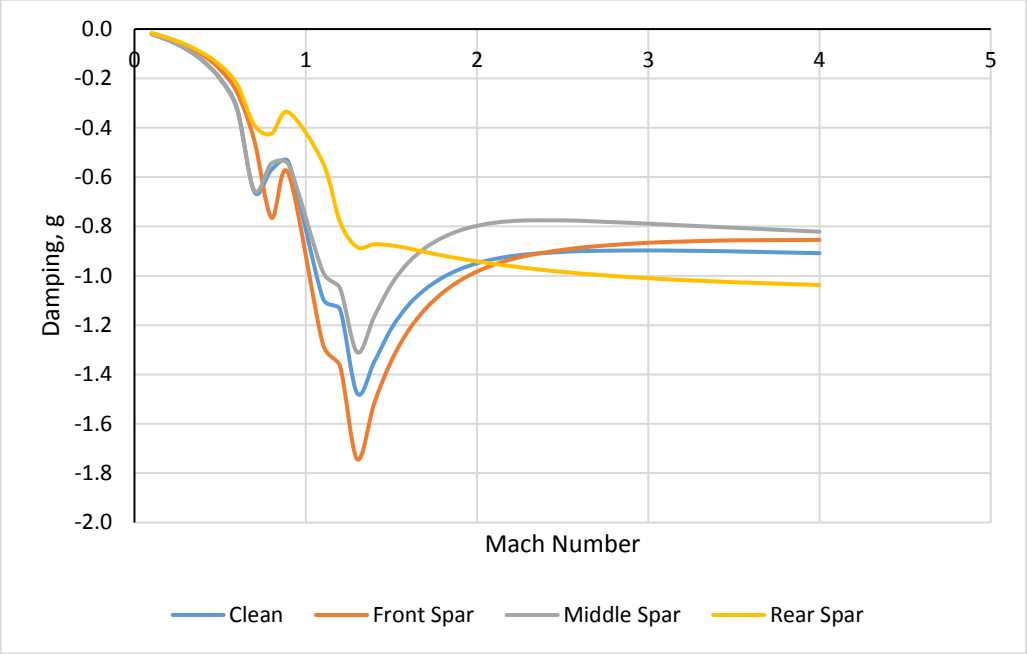

Figure 5.36 Damping vs Velocity Graph for the Torsion Mode of the External Weight Configurations

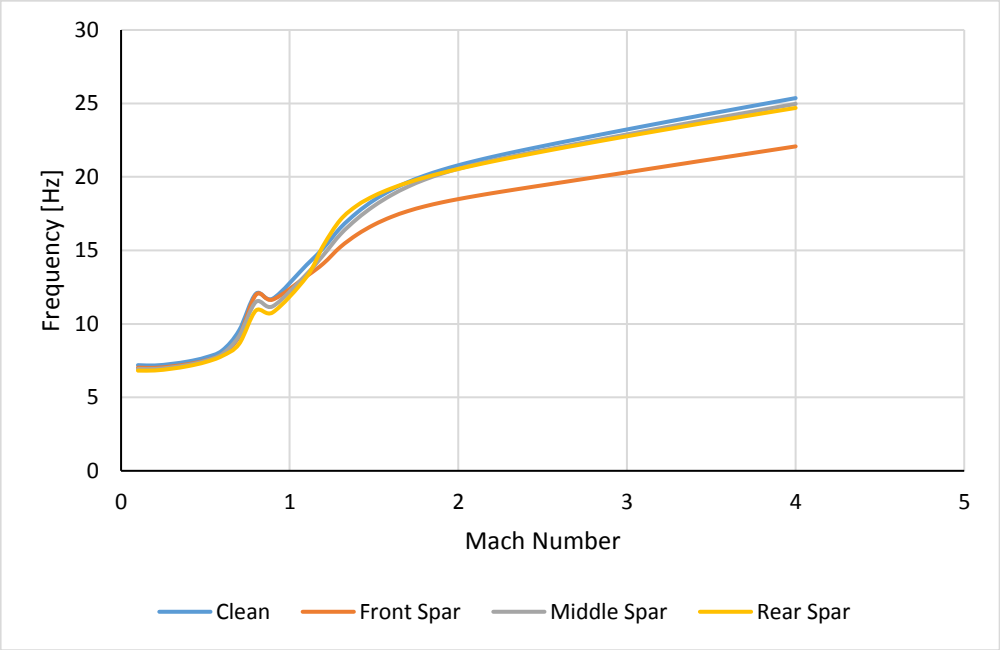

Figure 5.37 Frequency vs Velocity Graph for the Bending Mode of the External Weight Configurations

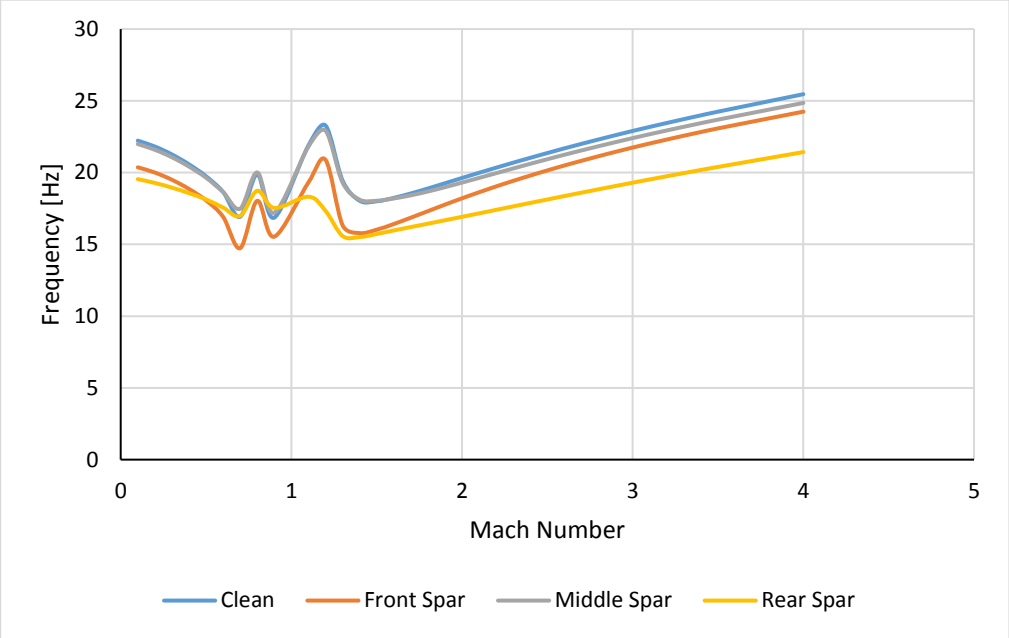

Figure 5.38 Frequency vs Velocity Graph for the Torsion Mode of the External Weight Configurations

The elastic axis of the baseline wing model is estimated to be located close to the middle spar as the torsion mode shape of baseline model shown in Figure 5.39 suggests.

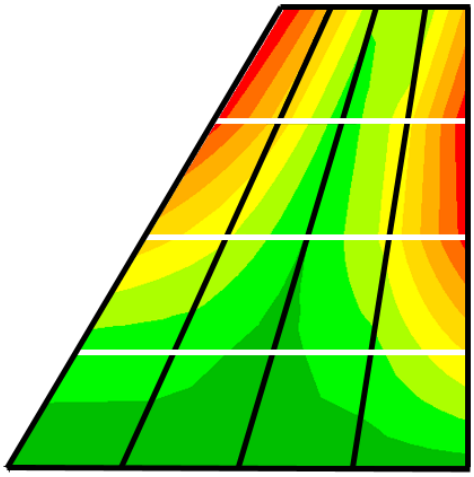

Figure 5.39 Upper View of the Torsion Mode Shape of the Baseline Model

The natural frequencies as well as the interpolated flutter speeds and flutter frequencies are given in Table 5.17. The natural frequencies and the mode shapes are given in Appendix A.

Table 5.17 Comparison of the External Weight Configurations

External Mass CG Location	**Bending Frequency [Hz]**	**Torsion Frequency [Hz]**	**Flutter Speed [M]**	**Flutter Frequency [Hz]**
Clean Conf.	7.55	22.53	2.96	23.14
Front Spar	7.36	20.62	2.54	20.29
Middle Spar	7.26	22.28	3.60	24.14
Rear Spar	7.12	19.76	1.91	20.28

The results show that the highest flutter speed is observed when the cg of the wing is closest to the elastic axis, which is very close to the middle spar. This is due to the reason that at this location, the static unbalance is closest to zero. Moreover, the difference between the bending and the torsional natural frequencies is highest for the case for which the external mass is attached to the middle spar. As a matter of fact, from the results given in Table 5.17, one can see that flutter speeds and the differences between the bending and the torsional natural frequencies are in order. That is, highest flutter speed corresponds to the case that has the highest difference between the bending and the torsional natural frequencies. Combined effect of low static unbalance and difference between the bending and the torsional natural frequencies is deemed to be the main reason for the high flutter speed of the wing which has an external mass connected to the middle spar. Finally, comparing the configurations with external weight shows that flutter Mach number decreases as the mass is moved from the leading edge towards the trailing edge. This is consistent with the research that the flutter speed generally decreases as the center of gravity is moved aft of the elastic axis [43].

CHAPTER 6

CONCLUSION AND FUTURE WORK

In Chapter 2, the typical section model is introduced as a simplification of a finite wing. This reduction is done by giving the geometric and inertial properties of an appropriate section of a finite wing to the two-dimensional typical section model. Furthermore, the typical section wing is given bending and torsional degrees-of-freedom as these two are the most important modes when classical flutter is considered. It is important to note that, throughout the study, the only two degrees-of-freedom considered for each flutter analysis are the bending and torsional DoFs due to this reason. Two supersonic theories, which are the Possio theory proposed by Garrick and Rubinow and the supersonic Piston theory, are used to derive the aerodynamic lift and moment equations used for the flutter calculations for a typical section wing model. Then the flutter problem is constructed using both of these methods and a code in MATLAB is developed that solve the supersonic flutter speed. The code written requires certain cross-sectional parameters that are listed in the related chapter as well as the ratio of the bending and torsional frequencies, therefore, a modal analysis is necessary to be solved beforehand as an input to the code. The code solves the flutter determinant using the classical flutter method which is also explained in detail. Finally, the validation of the codes with literature is presented as well as their comparison to each other. The code results with both theories show excellent agreement with results presented in literature. The flutter speeds calculated by the two theories get closer to each other at higher Mach numbers for all altitudes. In deciding on which theory to continue with in the subsequent chapters, literature is taken as reference and the supersonic piston theory is chosen.

In Chapter 3, the supersonic flutter speed of a finite wing is estimated with the two-dimensional supersonic Piston theory with thickness effects. A simple plate wing model is created with stiffeners on the leading and trailing edges. The variation of the span, beam cross-section and the material properties is analyzed and its effect on the supersonic flutter speed calculated by the typical section aerodynamics. As inputs for the code developed in Chapter 2, modal analysis is run for each configuration to obtain the corresponding bending and torsional natural frequencies. Furthermore, due to the simple nature of the wing model created, the straightforward derivations for the cross-sectional properties are also obtained. The first parameter studied which is the span variation showed results such that as the span increases, it results in a decrease in the bending and torsional stiffness of the wing. This decrease inherently leads to a decrease in the flutter speed which is successfully obtained from the results of the code. The second parameter which is the beam cross-sectional area showed an increase in wing stiffness in both degrees-of-freedom as the area increases. The code flutter results were again successful in reflecting this increase in stiffness and showed increase in wing flutter speed as the area increased. The final parameter which was analyzed was the change the modulus of elasticity of the material. The modulus of elasticity is about the tendency of a structure to deform when opposing forces are applied and is associated with the stiffness of a structure. Therefore, as the modulus of elasticity is increased, the bending and torsional stiffness characteristically also show an increasing trend. The code results were also successful in showing an increase in the flutter speed as the modulus of elasticity is increased. Finally, the results for the variations in each parameter was compared to the results obtained from a commercial aeroelastic solver which is ZAERO. The results compared showed that even though a in terms of quantitative comparison may not be achieved, the trends observed with both methods were in good agreement. It is then concluded that, the estimation of the flutter speed of a finite wing with the code developed in this study using the typical section supersonic piston theory aerodynamics is purposeful when a flutter speed for a certain wing configuration is known. The effect of the variation of the design parameters on the flutter speed can be obtained in a fast manner in the absence of a supersonic aeroelastic solver. This is especially beneficial in the beginning of a design phase when large numbers of design concepts are to be analyzed in a short amount of time.

In Chapter 4, a general review of the commercial aeroelastic solver ZAERO is provided as a basis information for further analysis in the upcoming chapter. The generation of the supersonic aerodynamic influence coefficient matrix, the interconnection of the structural degrees-of-freedom to the aerodynamic model using the spline approach and the flutter solution method used which is the g-method is explained with basic equations used by ZAERO. Finally, ZAERO is utilized to solve the flutter problem of the Weakened AGARD 445.6 Wing. The results are compared with the experimental solutions to prove the applicability of the ZAERO commercial tool. The comparison showed good agreement with the experimental results in the subsonic region, even reflecting the transonic dip predicted by the experimental methods. In the supersonic region, ZAERO over predicted the flutter speeds compared to experimental results however, in literature this trend is observed in the same way with other computational aerodynamic methods as well.

In Chapter 5, all the work that has been done up to this point is put to use to estimate the supersonic flutter characteristics of a fighter wing. Initially, a finite element model of a fighter wing is created in MSC. Nastran. The baseline wing model has five ribs and three spars and the spars are continuous along the wing span. The wing is modelled with all quadrilateral shell elements with different properties for the upper and lower skins, spars and ribs. As previously emphasized, since the degrees-of-freedom taken into account for the flutter analysis are the bending and torsional natural frequencies, modal analysis is performed using the finite element model of the wing including these modes only. Then, mesh refinement analyses of the structural and aerodynamic models are presented. In terms of the structural mesh, any finer FEM than the one with a single element in the interaction of the each spar and rib resulted in the appearance of local modes that interfered with the desired uncoupled bending and torsion natural frequencies. When a second approach for a fine model is utilized, the results showed no significant difference in the flutter results. Therefore, a coarse model is chosen for the structural mesh. In terms of the aerodynamic mesh, a suitable mesh size is chosen that performed the best in a trade-off between the most accurate flutter speed and the fastest computation time. With the structural and aerodynamic mesh approach chosen, the effect of the various aspects of a fighter wing on its supersonic flutter speed are solved. Flutter deals with the interaction of the aerodynamic, elastic and inertial

aspects of a wing, therefore the flutter characteristics of each configuration are interpreted by understanding the variation of the bending and torsional natural frequencies and the total weight of the wing analyzed since the aerodynamic model is not changed between the configurations due to the fixed outer geometry.

The first parameter whose effect on the flutter characteristics of a fighter wing studied is the spar number. The baseline spar number which is three is increased to six and nine. The modal analysis results showed that the bending frequencies did not show much increase when the spar number is increased from three to nine, however, there was a 2 Hz increase in the torsion frequency when the spar number was increased from three to six, and negligible increase from six to nine while the weight of the wing increased by 15 kg between each configuration. In terms of the flutter results, the flutter speed for the three spar configuration was about Mach 3, for the six spar configuration about Mach 6.5 and no flutter was observed with the nine spar configuration up to Mach 9. This increase in the flutter speed could be attributed to the increase in the weight between the configurations; however, further analysis is conducted to challenge this notion by keeping the weight of the total wing constant by adjusting the spar thicknesses accordingly. The flutter results showed similar trends compared to the initial analysis with the six spar flutter speed being around 5.5 and no flutter being observed up to 9 Mach for the nine spar configuration. This similar increase in the flutter speed when the total weight is kept constant shows that the increase in the flutter speed is not associated with the increase of the weight but is associated with the increase of the stiffness due to the higher number of continuous spars along the span.

The second parameter whose effect on the flutter characteristics of a fighter wing studied is the of spar orientation. Four types of spar orientations are considered which are the continuous spar configuration, leading edge parallel spar configuration, y-axis parallel spar configuration and two section spar configuration which is parallel to the y-axis between the root and second rib and continuous in the remaining sections. In order for a healthy comparison, the number of spars at the root are kept constant at six spars for every case. In terms of the natural frequencies, the bending frequency varies around the 0.30 Hz mark while the change in the torsion frequency is even more

negligible. In terms of the weight, the continuous and the LE parallel configurations have the highest weight followed by the two sections and y-axis parallel configurations being less by average of 7 kg. When the flutter speeds are compared, the highest flutter speed is observed for the continuous spar configuration at about Mach 6.5 and followed by the two-sections at about Mach 5.5. The LE parallel and the y-axis parallel gave lower flutter speeds with Mach 2 and Mach 1.9 respectively. The results show that the increase in the spar spacing at the tip of the wing has a dramatic effect on the flutter speeds of a fighter wing and for a delayed flutter point; the crowded spar spacing is preferable in terms of an aeroelastic point of view.

The third parameter whose effect on the flutter characteristics of a fighter wing studied is the skin material of the baseline model with three spars. The change resulting from the switch of wing skin from aluminum to carbon fiber reinforced plastic is observed as well as the effect of various composite ply orientations. Two types of fabrics utilized for the composite modelling are UD and woven fabric. Eight plies are chosen each one having a thickness of 0.25 mm to be consistent with the total thickness of the initial aluminum material which is 2 mm. The ply orientations are chosen to be quasi-isotropic ([0° 45° -45° 90° 90° -45° 45° 0°]). A further analysis is conducted by varying the ply orientations of all eight plies of the UD fabrics from 0° to 45° towards the leading edge to detect where the flutter speed becomes the highest. Consistent with literature, the highest flutter speed is observed at 25°. A final ply orientation is created with the UD fabric by replacing the first and last plies of the quasi-isotropic layup (0° plies) by 25° plies and this configuration is defined as the modified QI UD lay-up. Comparing these three composite skin models with the aluminum skin model showed an 80 kg difference. In terms of the natural frequencies, the modified QI UD lay-up had a significantly lower bending frequency and the highest torsional frequency and the aluminum configuration had the lowest natural frequencies. The UD QI and woven QI lay-ups have similar natural frequency values. In terms of the flutter speed, comparing the composite models, the woven QI lay-up had the lowest flutter speed around 2.5 Mach followed by UD QI lay-up at around 3.5 Mach and no flutter is observed for the modified QI UD lay-up up to 9 Mach. The results show that fighter wings with composite skins is more advantageous in terms of having higher flutter speeds and lower mass compared to all aluminum wings. Moreover, the use of woven

composites in the wing skins has no aeroelastic advantage when compared to the all-aluminum wing except for lower mass.

The final parameter whose effect on the flutter characteristics of a fighter wing studied is an external mass representing a missile or a pod being attached to the middle rib of baseline wing configuration. The effect of the external weight is analyzed by placing the CG of the mass at different locations along the middle rib. Since the mass of the external weight is kept constant for each configuration the flutter speed is mainly affected by the updated center of gravity. In terms of the natural frequencies, the difference in the bending frequencies are negligible while the clean configuration and the middle spar configuration have a higher torsional frequency by around 2 Hz compared to the front and aft spar configurations. In terms of the flutter speed, the configuration where the CG of the external mass is at the middle spar is the highest with 3.6 Mach flutter speed, followed by the clean configuration with around 3.0 Mach flutter speed. The front and aft external mass configurations have flutter speeds of 2.5 and 2.0 Mach respectively. The results show that regardless of the weight of the configurations, the updated center-of-gravity of the wing being closest to the elastic axis gives the highest flutter speed. The lower flutter speeds of the front and aft spar configurations can be attributed to the lower torsional frequencies however; an exact remark should not be made since for other cases studied throughout this study, the natural frequencies exclusively did not play a dominant role.

The results from all the cases considered show that a high flutter speed cannot be solely attributed to high weight or high natural frequencies since the flutter phenomena is very complex. However, the same conclusion can be reached for all cases considered in this study. When the natural frequencies are observed, the flutter speed is found to be the highest when the bending and torsion natural frequencies become apart from each other. This is consistent to the nature of flutter since flutter can be defined as the coupling of two or more modes at a certain flight condition. Therefore, considering the decreasing tendency of the torsion mode and the increasing tendency of the bending mode with speed, if the initial frequencies at zero speed, which are the natural frequencies, are closer to each other, these modes are likely to reach each other at a

lower speed compared to a structure with initial frequencies further apart from each other.

Future work that can further continue the work done for this study can be summarized as;

- Codes created in Chapter 2 can be used to estimate the flutter speed of a more complex wing with a more sophisticated flutter solution method .
- A generic load distribution can be applied to the various configurations and the resulting spar thickness and spacing could be carried out by an optimization process. The effect of the spar orientation can be done with the statically sized spar configurations.
- The control surface degrees-of-freedom can be also included in the study along with the bending and torsion modes.

REFERENCES

[1] R. L. Bisplinghoff, H. Ashley, and R. L. Halfman, *Aeroelasticity*. New York: Dover Publications, 1996.

[2] A. R. Collar, "The Expanding Domain of Aeroelasticity," *J. R. Aeronaut. Soc.*, vol. 50, no. 428, pp. 613–636, Aug. 1946.

[3] I. E. Garrick and W. H. Reed III, "Historical Development of Aircraft Flutter," *J. Aircr.*, vol. 18, no. 11, pp. 897–912, Nov. 1981.

[4] S. Von Borbely, "Aerodynamic Forces Harmonically Oscillating Wing Supersonic Speed," *Zeitschrift fur Angew. Math. und Mech.*, vol. 22, pp. 190–205, 1942.

[5] H. A. Temple, G. Jahn, "Flutter Supersonic Speeds," *Br. Aeronaut. Res. Counc. R. M. 2140*, 1945.

[6] I. E. Garrick and S. I. Rubinow, "Flutter and oscillating air-force calculations for an airfoil in a two-dimensional supersonic flow," *NACA Rep. 846*, Oct. 1946.

[7] C. Possio, "Aerodynamic Forces Oscillating Profile Supersonic Speeds," *Pontif. Accad. Sci. Acta*, vol. 1, no. 11, pp. 93–106, 1937.

[8] M. J. Lighthill, "Oscillating Airfoils at High Mach Number," *J. Aeronaut. Sci.*, vol. 20, no. 6, pp. 402–406, Jun. 1953.

[9] M. H. Rheinfzlrth and F. H. Swift, "A New Approach to the Explanation of the Flutter Mechanism," *NASA TN D-3125*, 1966.

[10] D. P. Raymer, *Aircraft design : a conceptual approach*. Washington, D.C: American Institute of Aeronautics and Astronautics, 2012.

[11] F. Sabri and A. A. Lakis, “Finite Element Method Applied to Supersonic Flutter of Circular Cylindrical Shells,” *AIAA J.*, vol. 48, no. 1, pp. 73–81, Jan. 2010.

[12] L. T. Niblett and B. S. Tech, *Flutter calculations on a supersonic aircraft wing*. Ministry of Supply, Aeronautical Research Council, 1955.

[13] W.-W. Zhang, Z.-Y. Ye, C.-A. Zhang, and F. Liu, “Supersonic Flutter Analysis Based on a Local Piston Theory,” *AIAA J.*, vol. 47, no. 10, pp. 2321–2328, Oct. 2009.

[14] D. S. Woolston and V. Huckel, “A calculation study of wing-aileron flutter in two degrees of freedom for two-dimensional supersonic flow,” *NACA Tech. Rep. 3160*, 1954.

[15] E. G. Broadbent, *Flutter Problems of High-Speed*. Ministry of Supply, Aeronautical Research Council, 1949.

[16] W. Mason, “A wing concept for supersonic maneuvering,” *NASA Contract. Reports*, 1984.

[17] P. W. Sacher, “Special Course on Fundamentals of Fighter Aircraft Design,” *AGARD CP-R-740*, 1987.

[18] A. G. Striz and V. B. Venkayya, “Influence of structural and aerodynamic modeling on flutter analysis,” *J. Aircr.*, vol. 31, no. 5, pp. 1205–1211, Sep. 1994.

[19] D. Liu, Z. Wan, and C. Yang, “The Influence of Spar Position on Aeroelastic Optimization of a Large Aircraft Wing with Different Materials,” in *53rd AIAA/ASME/ASCE/AHS/ASC Structures, Structural Dynamics and Materials Conference
20th AIAA/ASME/AHS Adaptive Structures Conference
14th AIAA*, 2012.

[20] N. Abdullah and E. Sulaeman, “AEROELASTIC FLUTTER ANALYSIS OF SUPERSONIC WING WITH MULTIPLE EXTERNAL STORES,” *IIUM Eng. Journal, Vol. 15, No. 2, 2014*, vol. 15, 2014.

[21] M. J. Turner and D. L. Grande, “Study of advanced composite structural design concepts for an arrow wing supersonic cruise configuration,” *NASA-CR-2825*, Apr. 1978.

[22] G. Kennedy and J. Martins, “A Comparison of Metallic and Composite Aircraft Wings Using Aerostructural Design Optimization,” in *12th AIAA Aviation Technology, Integration, and Operations (ATIO) Conference and 14th AIAA/ISSMO Multidisciplinary Analysis and Optimization Conference*, 2012.

[23] M. Ali, A. Hamed, “The Effect of Laminated Layers on the Flutter Speed of Composite Wing,” *J. Eng.*, vol. 18, no. 8, pp. 924–934, 2012.

[24] S. Guo, J. R. Banerjee, and C. Cheung, “The effect of laminate lay-up on the flutter speed of composite wings,” *Proc. Inst. Mech. Eng. Part G-journal Aerosp. Eng. - PROC INST MECH ENG G-J A E*, vol. 217, pp. 115–122, 2003.

[25] M. Sensmeier and J. Samareh, “A Study of Vehicle Structural Layouts in Post-WWII Aircraft,” in *45th AIAA/ASME/ASCE/AHS/ASC Structures, Structural Dynamics & Materials Conference*, 2004.

[26] Eurofighter.com, “Eurofighter Typhoon Technical Guide,” 2013. [Online]. Available: https://www.eurofighter.com/files/pdf/EF_TecGuide_2013.pdf. [Accessed: 17-Jun-2018].

[27] L. P. V. M. van Rijn, “Towards the fastenerless composite design,” Compos. Part A Appl. Sci. Manuf., vol. 27, pp. 915–920, 1996.

[28] M.-C. Meijer and L. Dala, “Generalized Formulation and Review of Piston Theory for Airfoils,” *AIAA J.*, vol. 54, no. 1, pp. 17–27, Jan. 2016.

[29] H. Ashley, “Piston Theory-A New Aerodynamic Tool for the Aeroelastician,” *J. Aeronaut. Sci.*, vol. 23, no. 12, pp. 1109–1118, Dec. 1956.

[30] P. Marzocca, L. Librescu, and W. A. Silva, “About the Effect of Control on Flutter and Post-Flutter of a Supersonic/Hypersonic Cross-Sectional Wing,” *NAG1-2281*, Jan. 2000

[31] MathWorks, *MATLAB 2016 Help*. Retrieved from MathWorks: MATLAB 2016 Help, 2016.

[32] M. NASTRAN, "Reference Manual, 2008," *MSC Softw. Corp.*, 2016.

[33] A. W. Leissa and M. S. Qatu, *Vibrations of continuous systems*. McGraw-Hill, 2011.

[34] ZONA Technology Inc, *ZAERO Theoretical Manual Version 9.2*, 3rd ed. 2016.

[35] P. C. Chen, "Damping Perturbation Method for Flutter Solution: The g-Method," *AIAA J.*, vol. 38, no. 9, pp. 1519–1524, Sep. 2000.

[36] J. T. J. Yates, E. C., Jr. Land, N. S. Foughner, "Measured and Calculated Subsonic and Transonic Flutter Characteristics of a 45 deg Sweptback Wing Planform in Air and in Freon-12 in the Langley Tran-sonic Dynamics Tunnel," *NASA TN D-1616*, 1963.

[37] R. M. Kolonay and H. T. Y. Yang, "Unsteady Aeroelastic Optimization in the Transonic Regime," *J. Aircr.*, vol. 35, no. 1, pp. 60–68, Jan. 1998.

[38] E. LEE-RAUSCH and J. BATINA, "Calculation of AGARD Wing 445.6 flutter using Navier-Stokes aerodynamics," in *11th Applied Aerodynamics Conference*, 1993.

[39] E. M. Lee-Rausch and J. T. Batina, "Wing flutter boundary prediction using unsteady Euler aerodynamic method," *J. Aircr.*, vol. 32, no. 2, pp. 416–422, Mar. 1995.

[40] "Metallic materials and elements for aerospace vehicle structures," *Mil. Stand. Handb. (United States Dept Defense), MIL-HDBK-5J*, 2003.

[41] O. Sener, T. Farsadi, M. O. Gozc, and A. Kayran, "Evaluation of the Effect of Spar Cap Fiber Angle of Bending-Torsion Coupled Blades on the Aero-Structural Performance of Wind Turbines," *J. Sol. Energy Eng. Trans. ASME*, vol. 140, no. 4, pp. 1–18, 2018.

[42] www.acpsales.com, “Mechanical Properties of Carbon Fiber Composite Materials, Fiber / Epoxy resin (120°C Cure).” [Online]. Available: http://www.acpsales.com/upload/Mechanical-Properties-of-Carbon-Fiber-Composite-Materials.pdf. [Accessed: 17-Jun-2018].

[43] J. K. Ramsey and K. R. V. Kaza, “Concentrated mass effects on the flutter of a composite advanced turboprop model,” *NASA-TM-88854*, Oct. 1986.

APPENDIX

MODE SHAPES OF THE FIGHTER WING CONFIGURATIONS

This section gives the mode shapes of the configurations analyzed for the fighter wing model.

1- Natural Frequencies for the Spar Orientation Variations

- Continuous Spar Orientation (6 Spars)

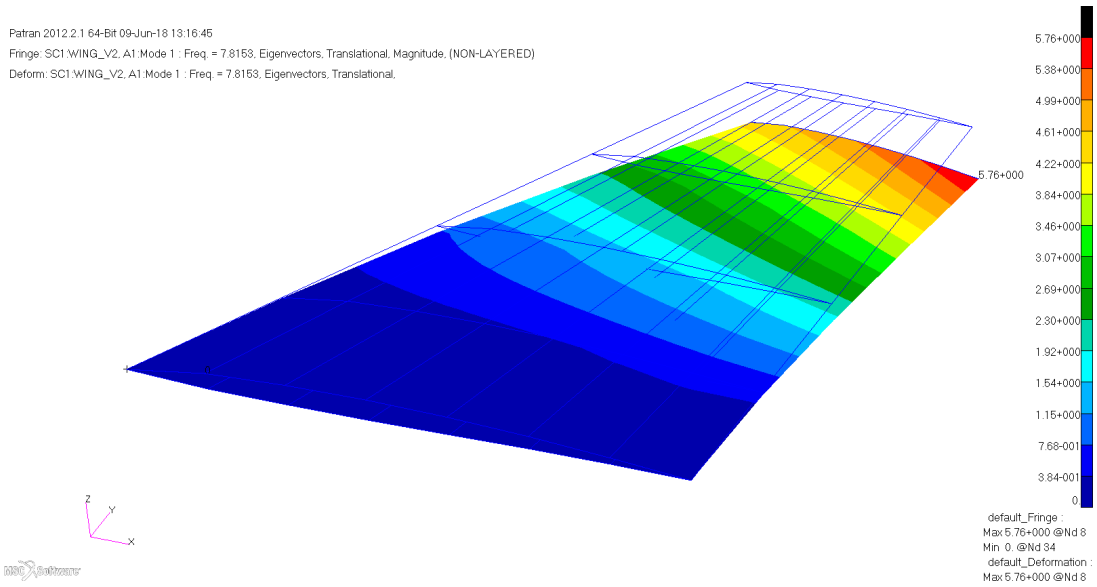

Figure A.1 Bending Natural Frequency – Continuous 6 Spar [7.82]

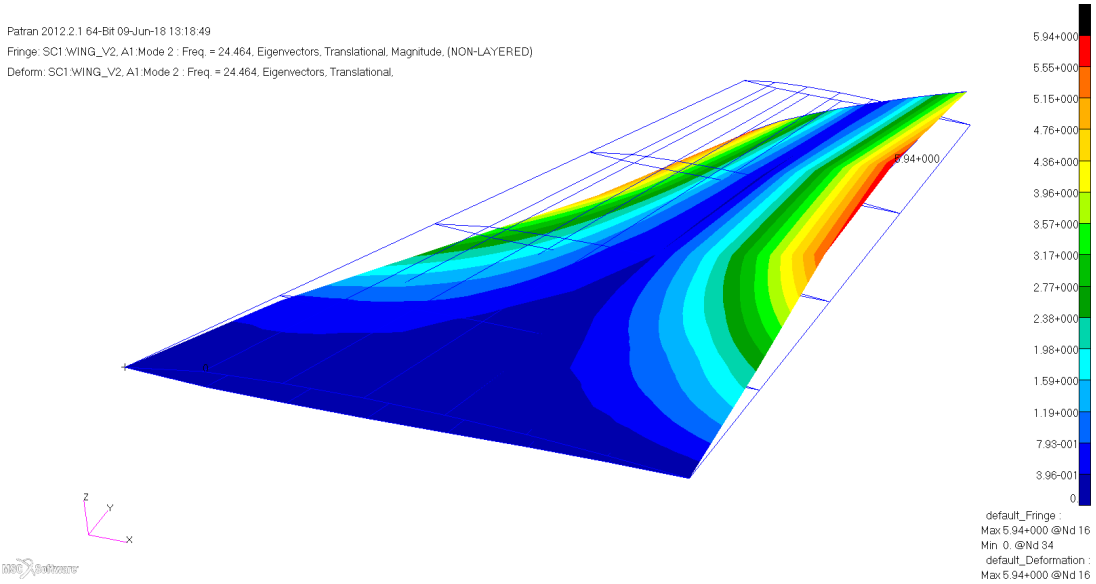

Figure A.2 Torsion Natural Frequency – Continuous 6 Spar [24.64]

- Continuous Spar Orientation (9 Spars)

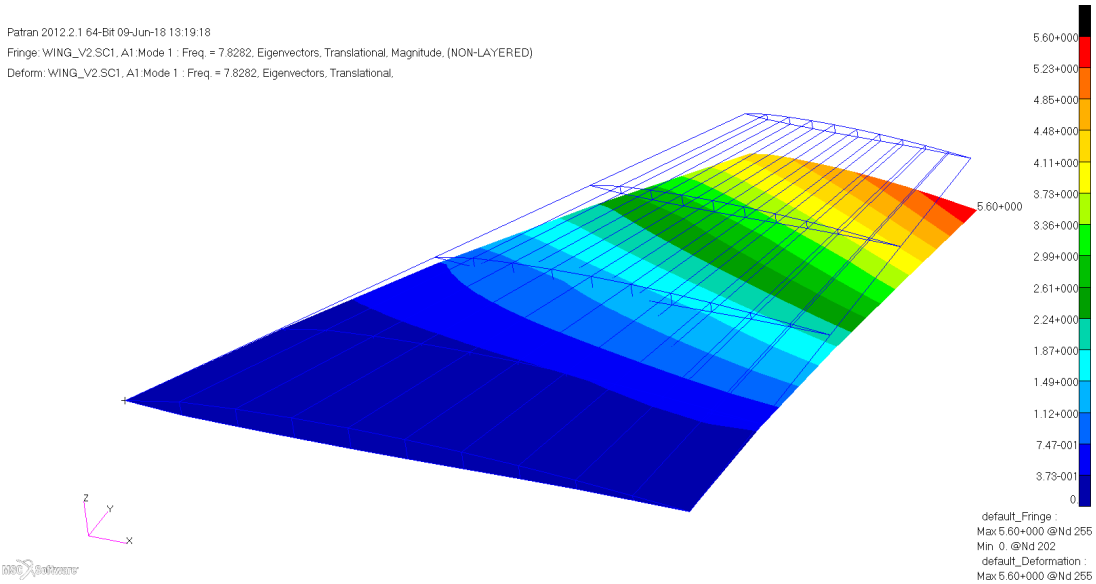

Figure A.3 Bending Natural Frequency – Continuous 9 Spar [7.83]

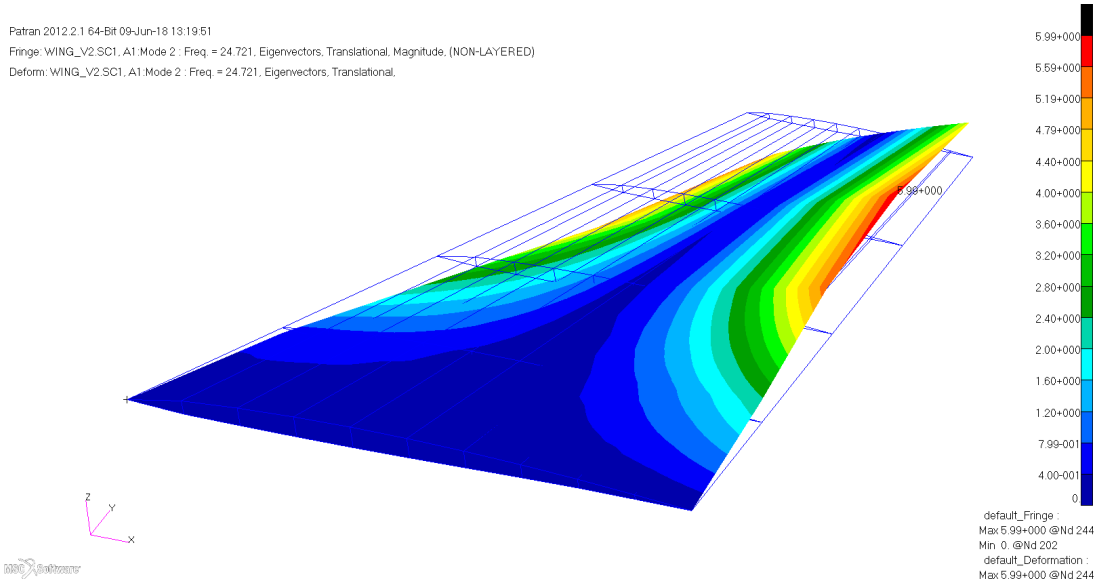

Figure A.4 Torsion Natural Frequency – Continuous 9 Spar [24.72]

- LE Parallel Spar Orientation (6 Spars)

7.62 cm

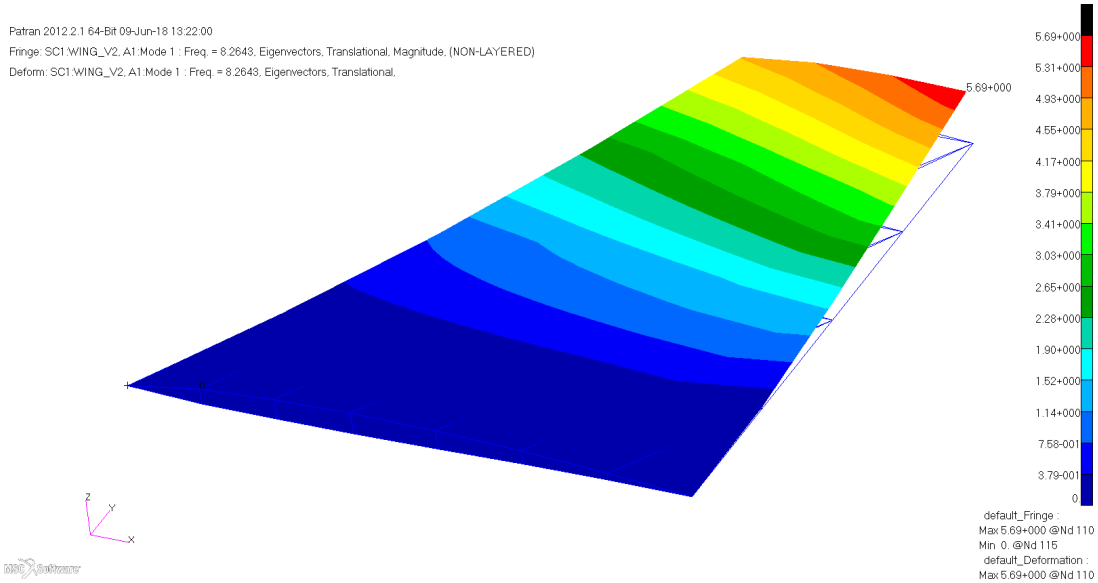

Figure A.5 Bending Natural Frequency – LE Parallel 6 Spar [8.26]

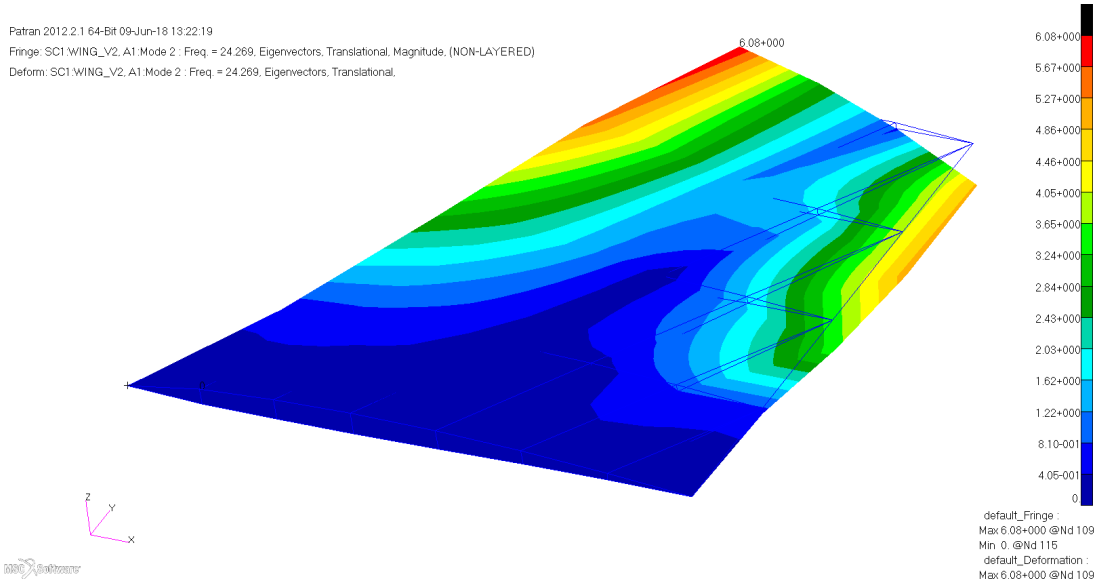

Figure A.6 Torsion Natural Frequency – LE Parallel 6 Spar [24.27]

- Y-Axis Parallel Spar Orientation (6 Spars)

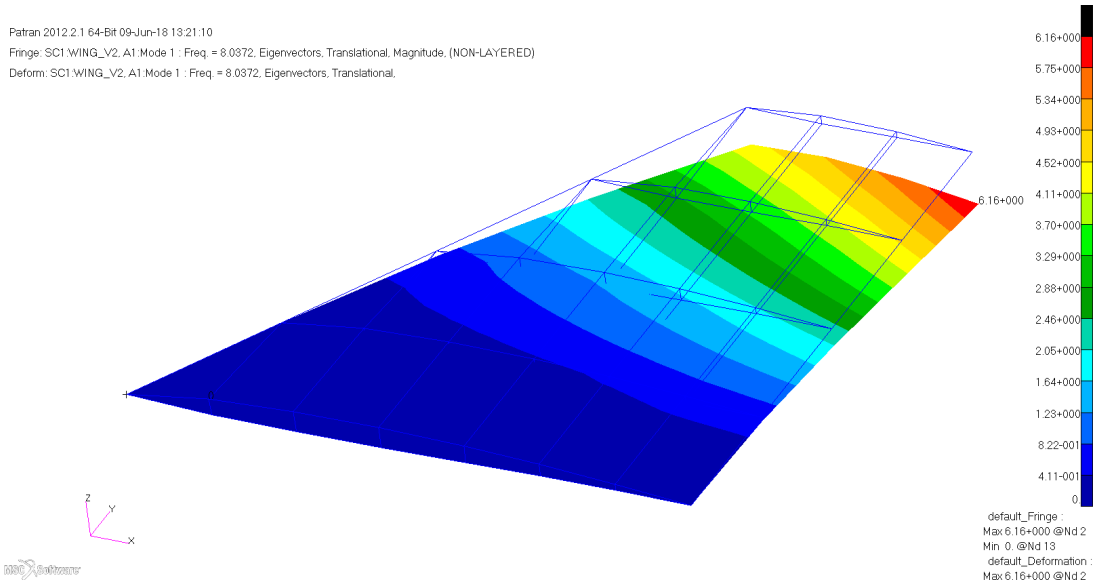

Figure A.7 Bending Natural Frequency – Y-Axis Parallel 6 Spar [8.04]

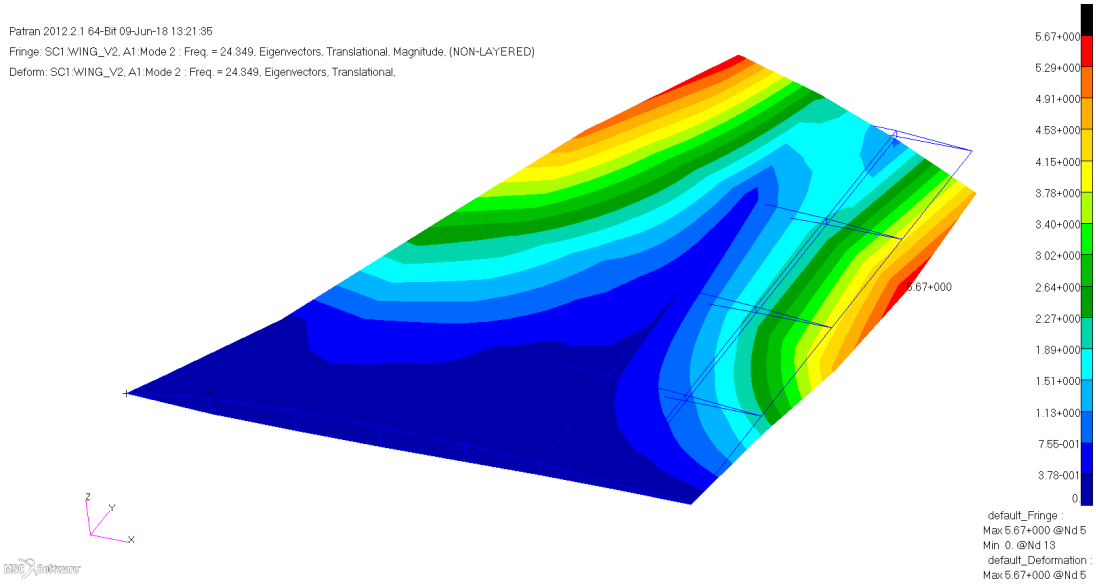

Figure A.8 Torsion Natural Frequency – Y-Axis Parallel 6 Spar [24.35]

- Two Section Spar Orientation (6 Spars)

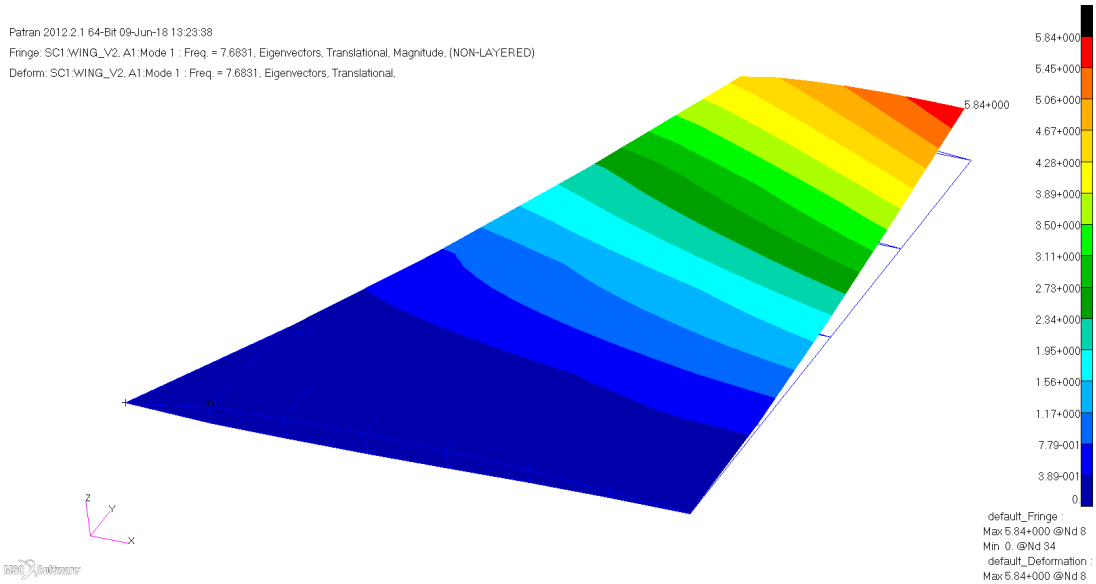

Figure A.9 Bending Natural Frequency – Two Section 6 Spar [7.68]

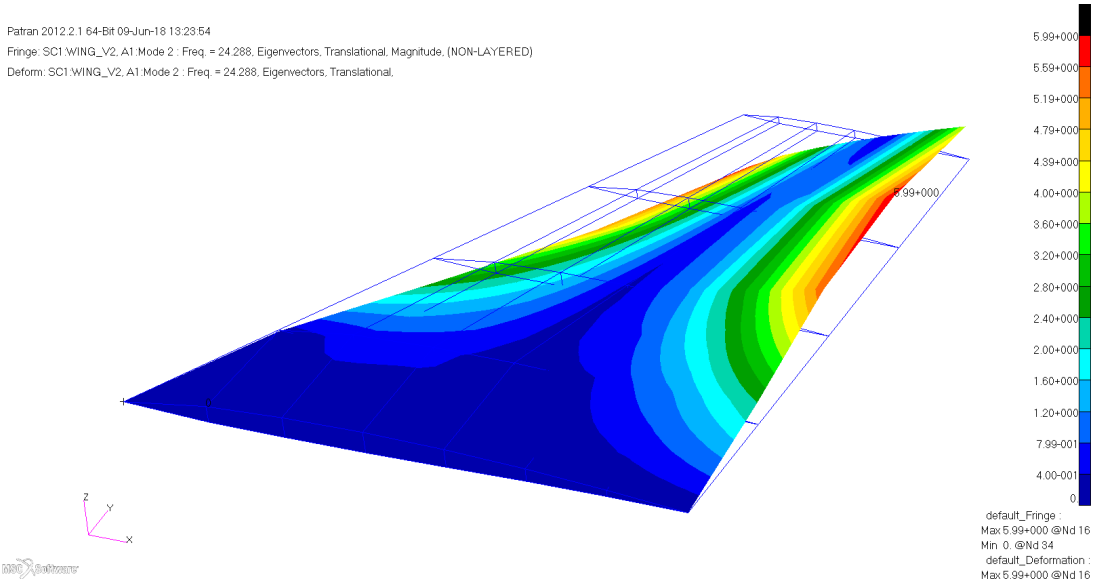

Figure A.10 Torsion Natural Frequency – Two Section 6 Spar [24.29]

2- Natural Frequencies for the Composite Skin Modelling of the Baseline Model

- Quasi-isotropic Woven Ply Orientation

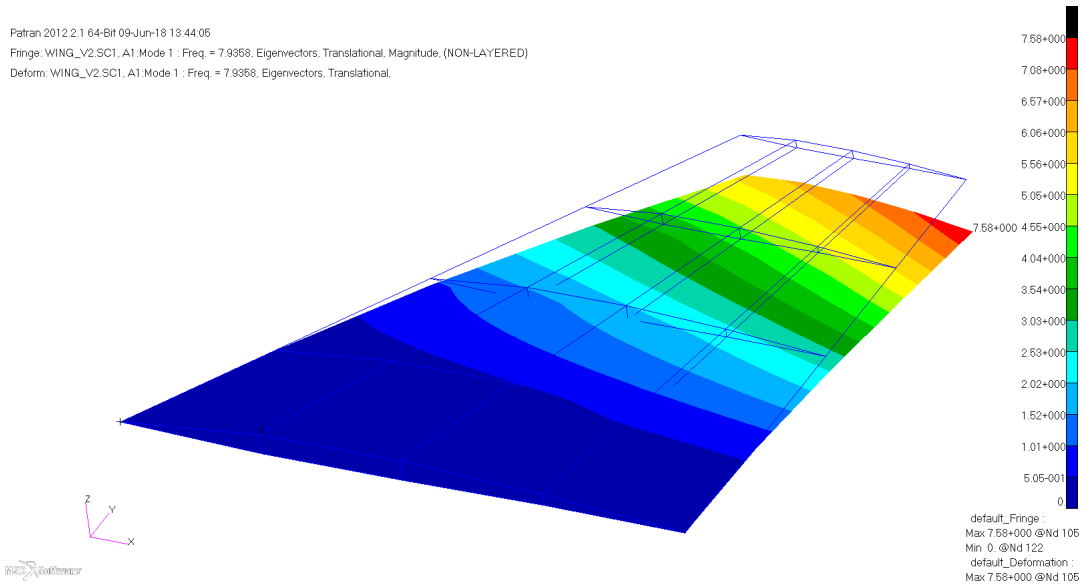

Figure A.11 Bending Natural Frequency – Quasi-isotropic Woven Skin Configuration [7.94]

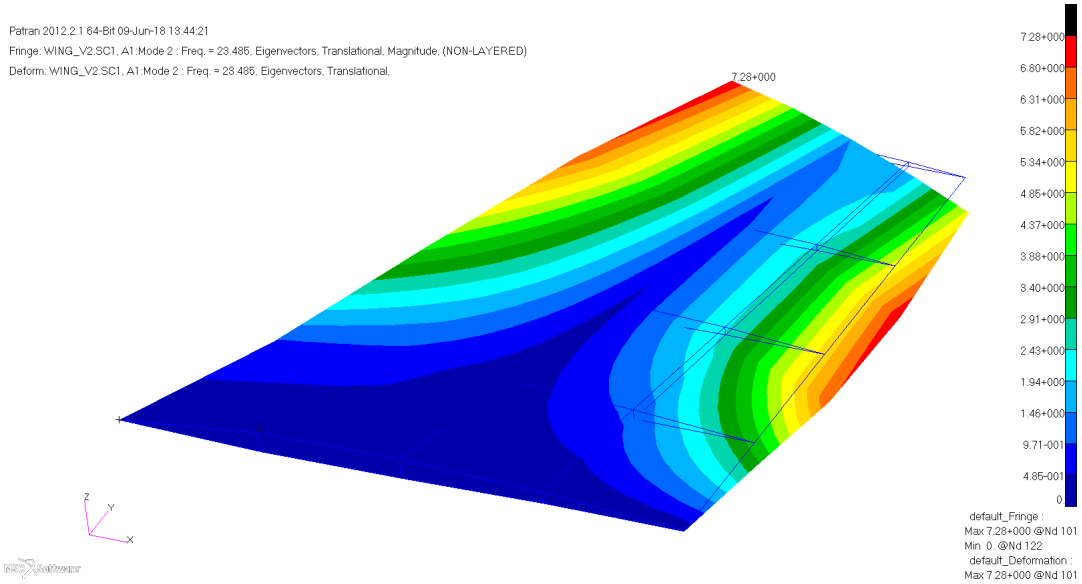

Figure A.12 Torsion Natural Frequency – Quasi-isotropic Woven Skin Configuration [23.49]

- Quasi-isotropic Uni-directional Ply Orientation

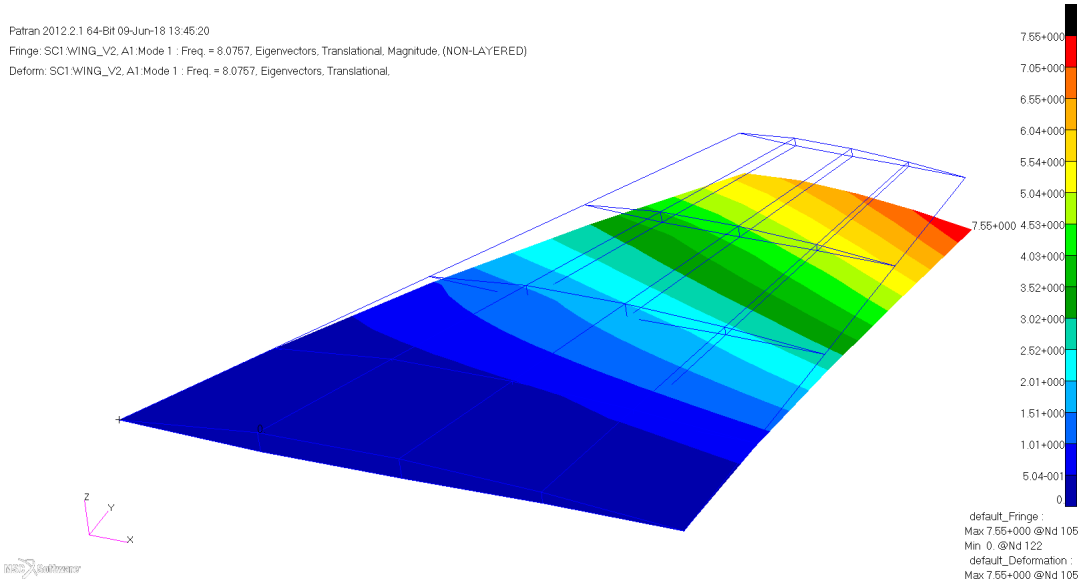

Figure A.13 Bending Natural Frequency – Quasi-isotropic UD Skin Configuration [8.08]

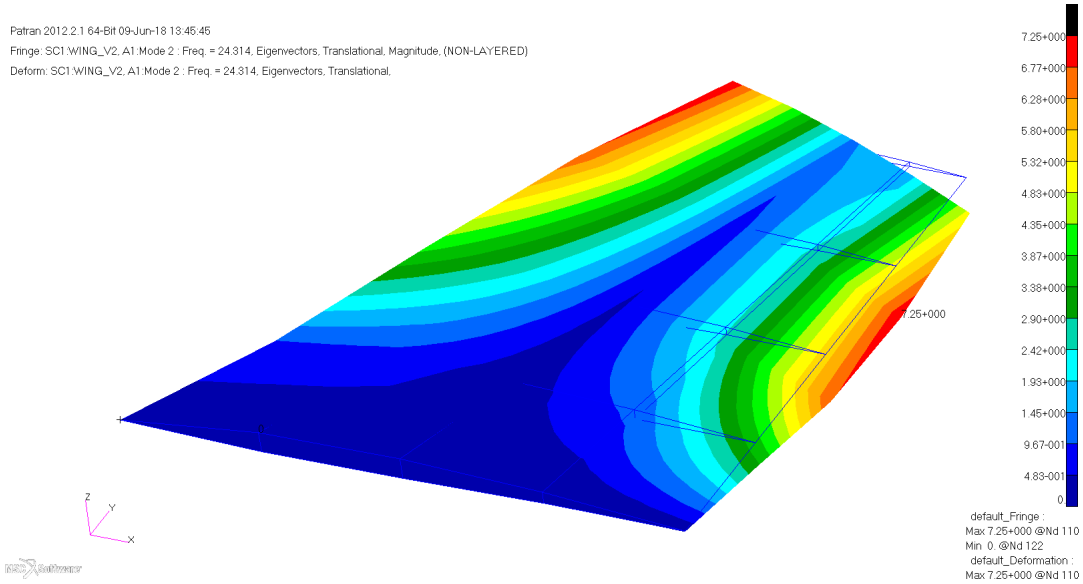

Figure A.14 Torsion Natural Frequency – Quasi-isotropic UD Skin Configuration [24.31]

- Modified Quasi-isotropic Uni-directional Ply Orientation

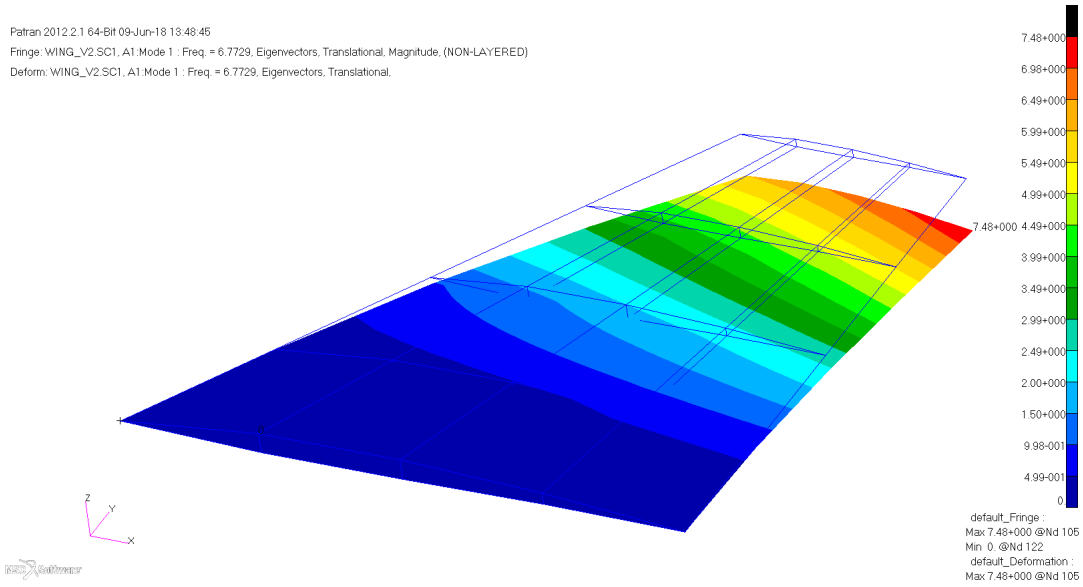

Figure A.15 Bending Natural Frequency – Modified Quasi-isotropic UD Skin Configuration [6.77]

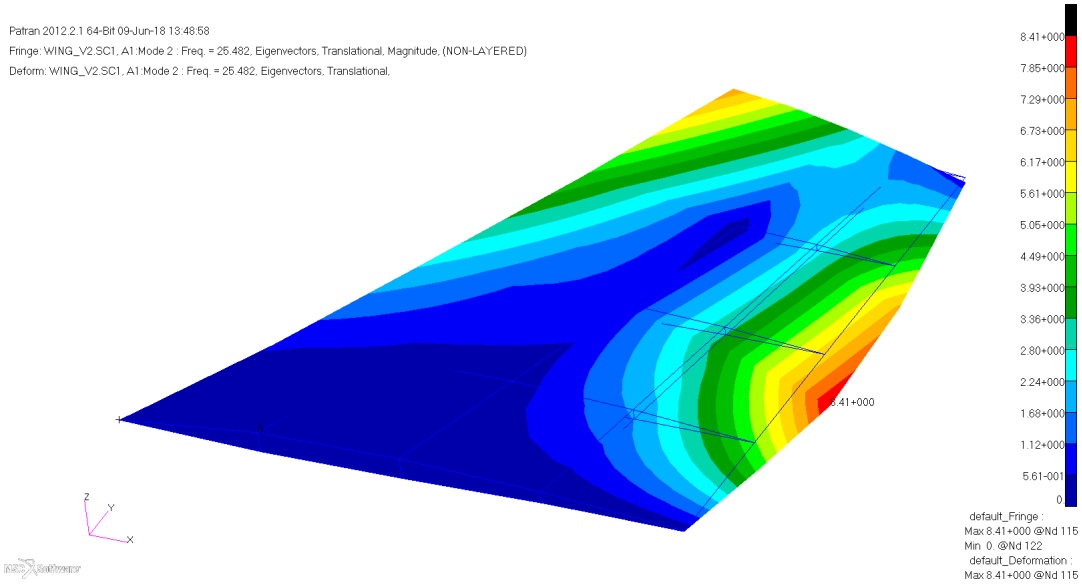

Figure A.16 Torsion Natural Frequency – Modified Quasi-isotropic UD Skin Configuration [25.48]

3- Natural Frequencies for the External Weight Orientation of the Baseline Model

- External Mass CG located at the Front Spar

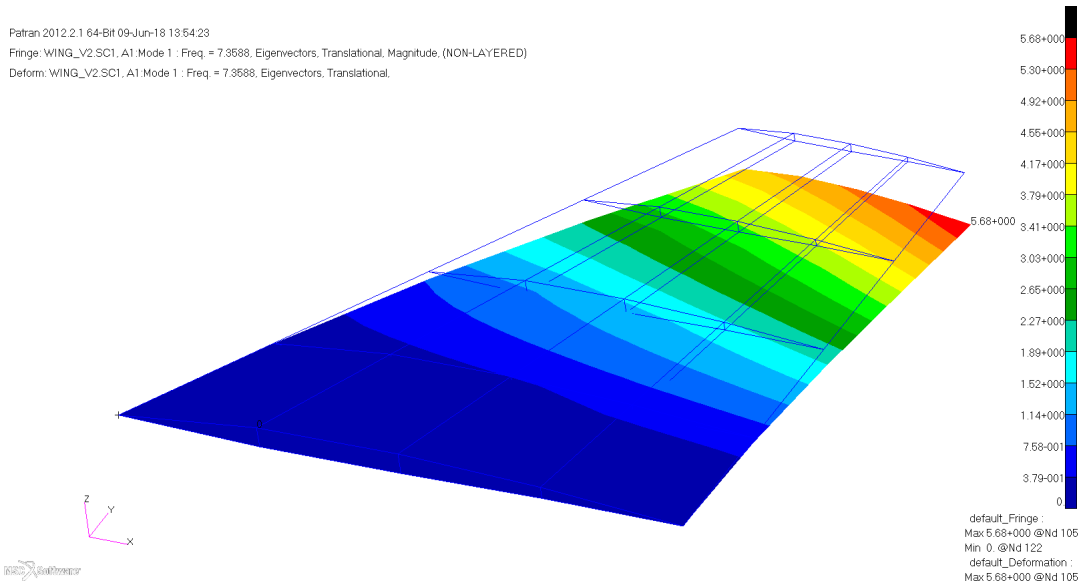

Figure A.17 Bending Natural Frequency – Front Spar Configuration [7.36]

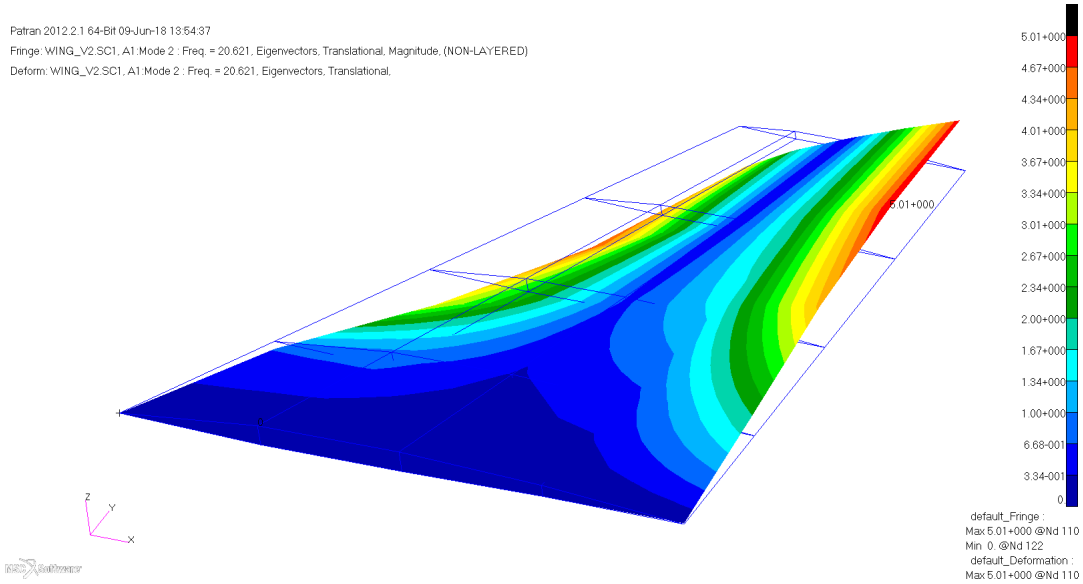

Figure A.18 Torsion Natural Frequency – Front Spar Configuration [20.62]

- External Mass CG located at the Middle Spar

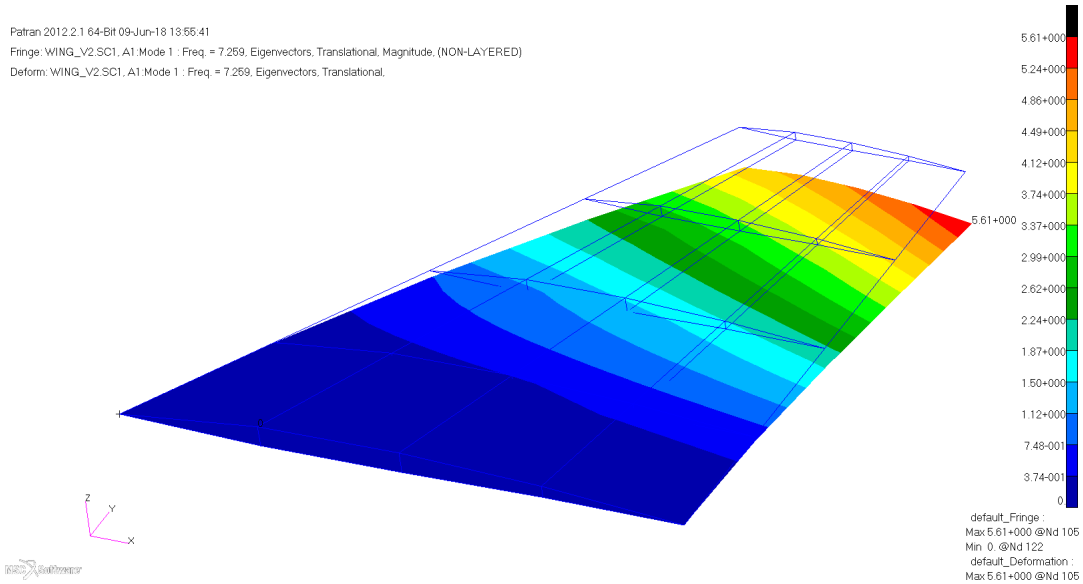

Figure A.19 Bending Natural Frequency – Middle Spar Configuration [7.26]

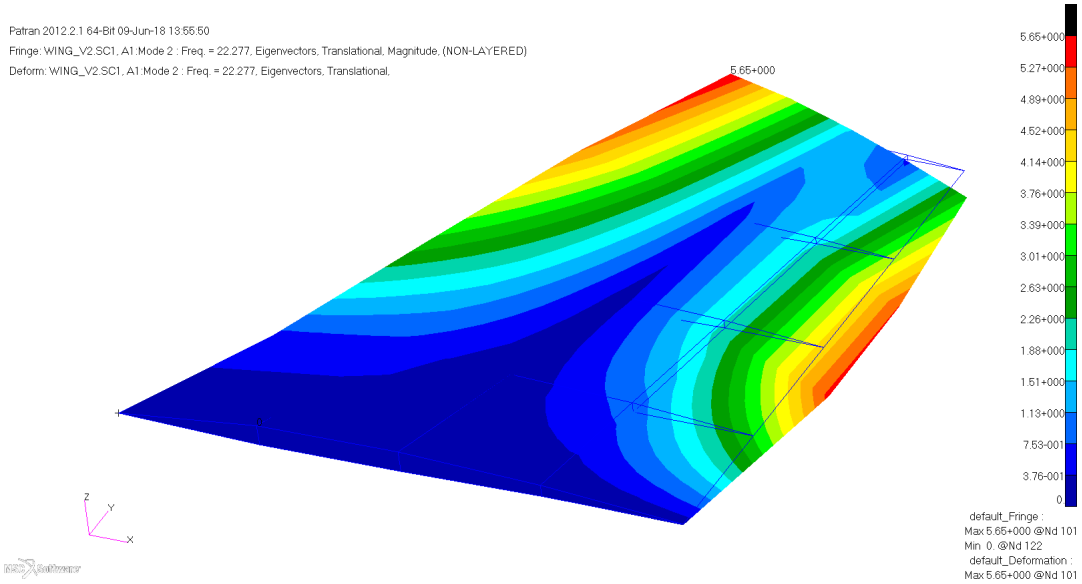

Figure A.20 Torsion Natural Frequency – Middle Spar Configuration [22.28]

- External Mass CG located at the Rear Spar

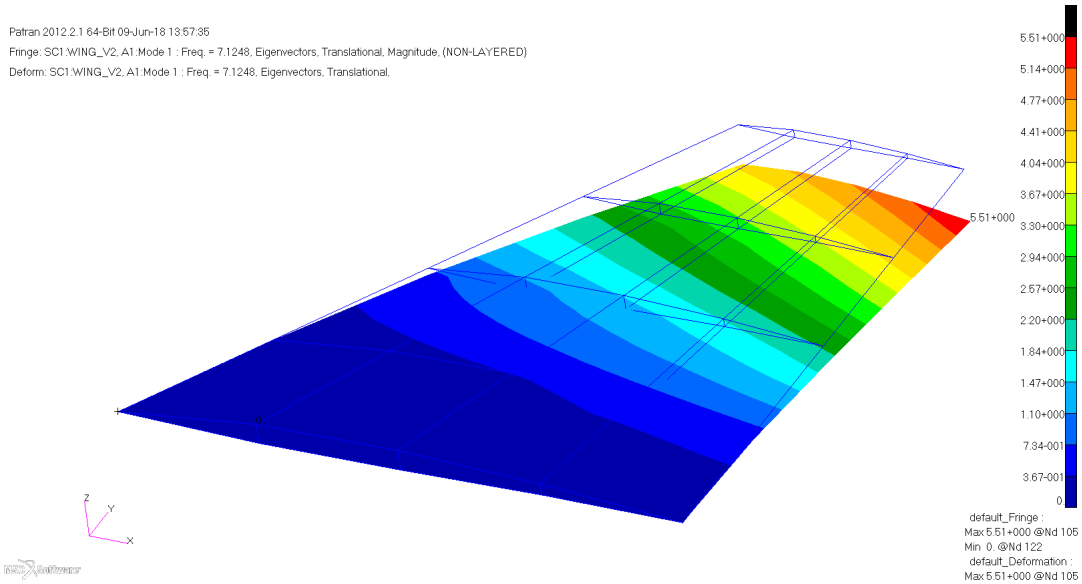

Figure A.21 Bending Natural Frequency – Rear Spar Configuration [7.12]

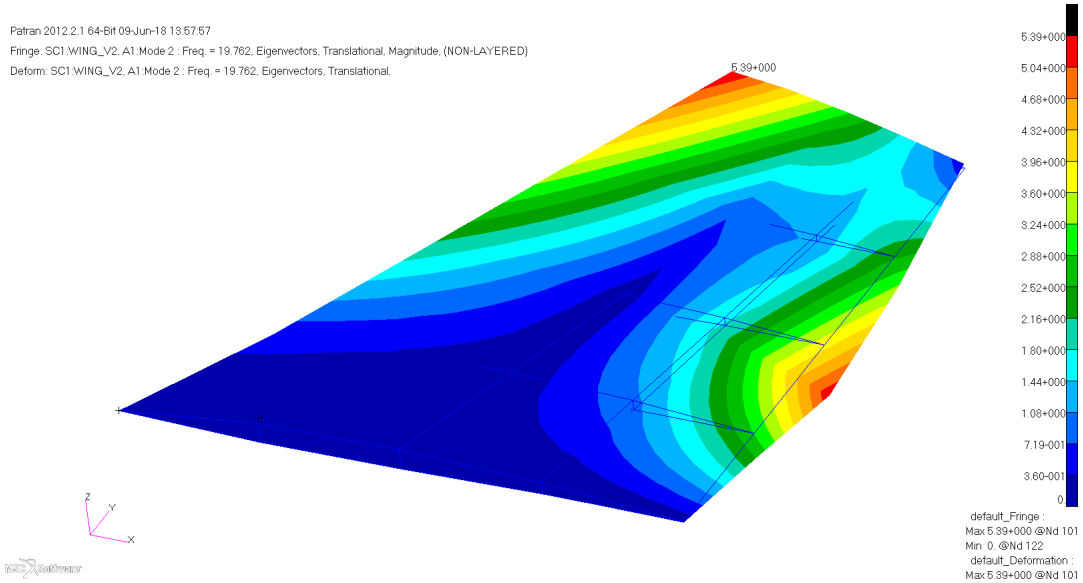

Figure A.22 Torsion Natural Frequency – Rear Spar Configuration [19.76]